

ASSESSMENT OF METHODS OF CORRECTION FOR SCATTER AND
ATTENUATION IN SPECT IMAGING

by

Yvonne McFarlane

A thesis presented to the University of Manitoba
in partial fulfillment of the requirements
for the degree of M.Sc. in Physics.

(c) Winnipeg, Manitoba.

July, 1988.

Permission has been granted to the National Library of Canada to microfilm this thesis and to lend or sell copies of the film.

The author (copyright owner) has reserved other publication rights, and neither the thesis nor extensive extracts from it may be printed or otherwise reproduced without his/her written permission.

L'autorisation a été accordée à la Bibliothèque nationale du Canada de microfilmer cette thèse et de prêter ou de vendre des exemplaires du film.

L'auteur (titulaire du droit d'auteur) se réserve les autres droits de publication; ni la thèse ni de longs extraits de celle-ci ne doivent être imprimés ou autrement reproduits sans son autorisation écrite.

ISBN 0-315-47863-2

ASSESSMENT OF METHODS OF CORRECTION FOR SCATTER
AND ATTENUATION IN SPECT IMAGING

BY

YVONNE McFARLANE

A thesis submitted to the Faculty of Graduate Studies of
the University of Manitoba in partial fulfillment of the requirements
of the degree of

MASTER OF SCIENCE

© 1988

Permission has been granted to the LIBRARY OF THE UNIVER-
SITY OF MANITOBA to lend or sell copies of this thesis, to
the NATIONAL LIBRARY OF CANADA to microfilm this
thesis and to lend or sell copies of the film, and UNIVERSITY
MICROFILMS to publish an abstract of this thesis.

The author reserves other publication rights, and neither the
thesis nor extensive extracts from it may be printed or other-
wise reproduced without the author's written permission.

TABLE OF CONTENTS

	PAGE NUMBER
Acknowledgements	(v)
Abstract	(vii)
List of Figures	(ix)
List of Tables	(xv)
Chapter I Introduction	1
(a) Diagnostic Imaging Modalities	2
(i) Imaging with X-rays	3
(ii) Imaging with Gamma rays	5
(iii) Ultrasound Imaging	8
(iv) Magnetic Resonance Imaging (MRI)	9
(b) Nuclear Medicine	11
(i) Radionuclides	11
(ii) The Gamma Camera	16
(iii) Camera Characteristics	40
(iv) Image Characteristics	45
(v) Planar Imaging and SPECT	52
(c) Principles of SPECT	54
(i) Reconstruction of Images from Projections	54

(ii) Artifacts	68
(d) Problems with Quantitative SPECT Imaging	71
(i) Scatter	80
(ii) Attenuation	87
(e) Corrections for Scatter and Attenuation	93
(i) Compensation for Scatter	93
(ii) Compensation for Attenuation	101
(f) Purpose of this Research	108
Chapter II Equipment	110
(a) The Phantom	111
(b) The Radioisotope	116
(c) The System Hardware	117
(d) Operation of the System	119
(i) ECT Data Acquisition	119
(ii) Word to Byte Framing	119
(iii) ECT Data Normalization and Sensitivity Correction	121
(iv) ECT Reconstruction	121
Chapter III Method	125
(a) Acquisition Information	126
(b) Sensitivity Maps	128

(c) ECT Reconstruction	129
(d) Value of the Attenuation Coefficient	134
(e) Subtraction	145
(f) Lesion Size and Contrast	146
(g) Assessment of Errors in Contrast and Lesion Size Measurement	151
Chapter IV Results and Discussion	152
(a) Attenuation Coefficients	153
(b) Lesion Contrast and Size Measurements	157
(c) Symmetric Windows	163
(d) Asymmetric Windows	172
(e) Subtraction Images	182
Chapter V Conclusion	222
Chapter VI References	225

ACKNOWLEDGEMENTS

I would like to thank my supervisor, Dr. Roger Palser, for his encouragement and guidance during my studies, and for being always approachable and patient.

I would also like to thank the members of the Medical Physics Department, and the Nuclear Electronics Section (in particular, Mr. Vic Goertzen), of the Manitoba Cancer Treatment and Research Foundation, for their knowledgeable advice in times of crisis.

My thanks are also due to Dr. David Greenberg, who gave permission for me to use the equipment of the Nuclear Medicine Department of the Health Sciences Centre, and to Mrs. Leslie Clement, and the Nuclear Medicine Technologists, for teaching me how to use it correctly.

Financial support during this period of study was, in part, provided by the Manitoba Cancer Treatment and Research Foundation.

Many other people contributed to the completion of this work; I would especially like to thank Dr. and Mrs. Ed Taylor, and Mr. and Mrs. Larry Jonassen, and the many friends who encouraged me throughout.

Last, but certainly not least, I would like to thank my family, who supported me in every way they could, although they never understood what I was doing, only that it was very important to me.

ABSTRACT

The ability to correct for the scatter and attenuation of gamma photons is important if quantitative single photon emission computed tomography (SPECT) is to become a reality. This work was designed to assess the efficacy and clinical utility of some suggested correction methods, using the Elscint ECT system.

A cylindrical phantom, one half of which contained perspex rods while the other did not, was imaged when filled with Tc-99m solution. Scatter correction was by use of narrow symmetric and asymmetric windows for data acquisition and by separate acquisition of scatter images in a lower energy window, prior to subtraction from the photopeak images. The system software applies Chang's attenuation correction to the reconstructed data with user-selectable attenuation coefficient values. A method has been developed, allowing these values to be conveniently determined. The values thus obtained were applied to the images and the effect on lesion contrast and resolution assessed.

Some improvements in image quality were observed with specific symmetric and asymmetric data acquisition windows. However, by reconstructing a scatter image, and subtracting an experimentally determined fraction of this image from the photopeak image, much more noticeable improvements in image contrast (and therefore detectability) and resolution were achieved, even for a lesion small enough in size, and deep enough within the phantom, to be difficult to detect and measure.

The decision as to which is the appropriate subtraction fraction, for a particular set of acquisition parameters (e.g. window size, window position, etc.), must also include a consideration of the aim of the study, in terms of the relative importance of having high contrast and good resolution. To help in this decision, a simple method of evaluating the possible subtraction fractions, with respect to their effect on contrast and resolution of a specific lesion, has been suggested.

LIST OF FIGURES

	PAGE NUMBER
Fig 1.1 Decay scheme of Tc-99m.	14
Fig 1.2 Main features of the gamma camera.	17
Fig 1.3 Function of a collimator.	21
Fig 1.4 Types of collimator.	28
Fig 1.5 Schematic drawing of a gamma camera with seven photomultiplier tubes.	33
Fig 1.6 PHA window positioned on the photopeak of a Tc-99m spectrum.	37
Fig 1.7 The components of a gamma camera system.	43
Fig 1.8 Profile of the image of a small radioactive source.	50
Fig 1.9 Reconstruction of an image by backprojection.	56
Fig 1.10 Shape of ramp filter in frequency and spatial domain.	61
Fig 1.11 Linear superposition of filtered backprojections.	65
Fig 1.12 Relative importance of photoelectric effect, Compton effect and pair production.	76

Fig 1.13	A possible sequence of interactions of a photon passing through matter.	78
Fig 1.14	Representation of a Compton collision.	81
Fig 1.15	Transaxial slice through a "flood" phantom, and corresponding count profile along a line through the centre.	90
Fig 2.1	(a)The phantom - longitudinal view.	112
	(b)The phantom - transaxial view, to illustrate internal structure.	114
Fig 2.2	Characteristics of Hanning normal and ramp filters.	123
Fig 3.1	Images of the phantom: 2 slices, each 14 pixels deep.	130
Fig 3.2	A set of reconstructed slices.	132
Fig 3.3	Flood slice with count profile.	135
Fig 3.4	Idealized count profiles to show the effect of attenuation.	138
Fig 3.5	Coefficient 'a' plotted against attenuation coefficient.	143
Fig 3.6	To show how the contrast values were obtained.	147

Fig 4.1	Contrast of three lesions, without attenuation correction, plotted against (symmetric) window size.	159
Fig 4.2	Contrast of three lesions, without attenuation correction, plotted against (asymmetric) window size.	159
Fig 4.3	Contrast of three lesions, after attenuation correction, plotted against (symmetric) window size.	161
Fig 4.4	Contrast of three lesions, after attenuation correction, plotted against (asymmetric) window size.	161
Fig 4.5	Contrast and resolution of lesion 19/80, with and without attenuation correction, plotted against (symmetric) window size.	166
Fig 4.6	Contrast and resolution of lesion 30/50, with and without attenuation correction, plotted against (symmetric) window size.	168
Fig 4.7	Contrast and resolution of lesion 16/50, with and without attenuation correction, plotted against (symmetric) window size.	170
Fig 4.8	Contrast and resolution of lesion 19/80, with and without attenuation correction,	176

- plotted against (asymmetric) window size.
- Fig 4.9 Contrast and resolution of lesion 30/50, 178
with and without attenuation correction,
plotted against (asymmetric) window size.
- Fig 4.10 Contrast and resolution of lesion 16/50, 180
with and without attenuation correction,
plotted against (asymmetric) window size.
- Fig 4.11 Contrast and resolution of lesion 19/80, 184
plotted against subtraction fraction, for
images acquired with 10-10% window on the
photopeak.
- Fig 4.12 Contrast and resolution of lesion 19/80, 186
plotted against subtraction fraction, for
images acquired with 8-4% window on the
photopeak.
- Fig 4.13 Contrast and resolution of lesion 19/80, 188
plotted against subtraction fraction, for
images acquired with 6-6% window on the
photopeak.
- Fig 4.14 Contrast and resolution of lesion 30/50, 192
plotted against subtraction fraction, for
images acquired with 10-10% window on the
photopeak.

- Fig 4.15 Contrast and resolution of lesion 30/50, 194
plotted against subtraction fraction, for
images acquired with 8-4% window on the
photopeak.
- Fig 4.16 Contrast and resolution of lesion 30/50, 196
plotted against subtraction fraction, for
images acquired with 6-6% window on the
photopeak.
- Fig 4.17 Contrast and resolution of lesion 16/50, 200
plotted against subtraction fraction, for
images acquired with 10-10% window on the
photopeak.
- Fig 4.18 Contrast and resolution of lesion 16/50, 202
plotted against subtraction fraction, for
images acquired with 8-4% window on the
photopeak.
- Fig 4.19 Contrast and resolution of lesion 16/50, 204
plotted against subtraction fraction, for
images acquired with 6-6% window on the
photopeak.
- Fig 4.20 Contrast plotted against resolution ratio 208
for lesion 19/80, 10-10% photopeak window.
- Fig 4.21 Contrast plotted against resolution ratio 208

- for lesion 19/80, 8-4% photopeak window.
- Fig 4.22 Contrast plotted against resolution ratio 210
for lesion 19/80, 6-6% photopeak window.
- Fig 4.23 Contrast plotted against resolution ratio 213
for lesion 30/50, 10-10% photopeak window.
- Fig 4.24 Contrast plotted against resolution ratio 213
for lesion 30/50, 8-4% photopeak window.
- Fig 4.25 Contrast plotted against resolution ratio 215
for lesion 30/50, 6-6% photopeak window.
- Fig 4.26 Contrast plotted against resolution ratio 218
for lesion 16/50, 10-10% photopeak window.
- Fig 4.27 Contrast plotted against resolution ratio 218
for lesion 16/50, 8-4% photopeak window.
- Fig 4.28 Contrast plotted against resolution ratio 220
for lesion 16/50, 6-6% photopeak window.

LIST OF TABLES

	PAGE NUMBER
Table 3.1: Lesions for which results are quoted	150
Table 4.1: Attenuation coefficients for symmetric windows	155
Table 4.2: Attenuation coefficients for asymmetric windows	155
Table 4.3: Attenuation coefficients for windows used for subtraction	156

CHAPTER I INTRODUCTION

(a) DIAGNOSTIC IMAGING MODALITIES

(Beck, 1982; Anger, 1964; Johns and Cunningham, 1983)

In the latter part of 1895, Roentgen discovered X-rays, and subsequently made a thorough investigation of their properties. He very rapidly attracted the attention of the medical profession with a shadow image showing the bone structure of his own hand (Roentgen, 1896). Since then, ionizing radiations have been used in medicine for a variety of applications which has changed and expanded as electronic and computer technology have developed. From that first planar shadow image have grown the fields of diagnostic radiology, radiotherapy and nuclear medicine, in which ionizing radiation may be used, for example, to create three-dimensional images of body organs or to treat deep-lying tumours. The involvement of physics with medicine has led to other developments such as the use of ultrasound and nuclear magnetic resonance as imaging techniques, and to continued exploration of ways to improve existing techniques.

The subject of this work is in the field of diagnostic imaging. Therefore let us review briefly the variety of modalities available, to provide the physician with information on physiological structure and function.

(i) IMAGING WITH X-RAYS.

A beam of X-rays may be transmitted through a patient and detected as it emerges. The tissues in the patient differentially attenuate the X-rays, resulting in an energy dependent shadow picture, which is actually a map of the X-ray attenuation coefficients in the path of the beam. If the differences in attenuation coefficients are not sufficient to give detectable image contrast of the tissues under investigation, radio-opaque dyes may be administered to the patient in order to increase the contrast. Thus, by suitable manipulation of factors that include the beam energy and administration of contrast media, planar images giving primarily structural information may be obtained.

The images obtained in the way just described are a very useful diagnostic tool. However, they are really two-dimensional projections of three-dimensional subject matter, in which information from several different structures overlaps, leading to poor discrimination of changes in attenuation coefficient and reduction in contrast. As a result, low-contrast details within the image may be difficult to distinguish. Attempts to solve this problem have led to the development of tomographic imaging techniques, with which the aim is to create images of slices through a three-dimensional object. The direction of these images, when reconstructed, is perpendicular to the direction of planar X-ray images, and therefore they contain only the statistical noise, inherent in the photon detection process, in that particular slice and little from the tissue above and below.

The simplest type of tomographic image employs simultaneous motion of source and detector, to give an image in which only one plane is in focus, while others are blurred. This is useful for imaging fine-detail, high-contrast objects such as the small bones of the ear.

X-ray computed tomography (CT) further extends this technique, to produce images which are two-dimensional transaxial slices through the patient. Typically, the patient is stationary and located within the arc of a rotating gantry which contains an X-ray tube and an arrangement of one or more detectors. The source-detector assembly is rotated around the patient, making a series of transmission measurements. This information is used to reconstruct the two-dimensional map of X-ray attenuation coefficients. The basic technique for image reconstruction was developed by Radon in 1917, and has since been in use in many areas of scientific research. However, it was not until digital computer technology had suitably advanced, that Hounsfield (in 1973) was able to introduce the first CT scanner for medical applications.

(ii) IMAGING WITH GAMMA RAYS.

Gamma ray imaging is undertaken in nuclear medicine departments, and provides information regarding physiological function. Radionuclides are used to tag compounds which are involved in physiological functions,

and which therefore localize in specific tissues or body products. The labelled compounds are called radiopharmaceuticals, and are employed in three main areas.

They may be used in treatments, such as radiotherapy treatment for enlarged thyroid gland, although treatments are generally only a small proportion of the work of a nuclear medicine department.

They may be used in diagnostic processes involving the determination of the amount of radioactivity in samples of blood, urine, faeces, etc. The sample, usually counted in a well counter, becomes an indicator of some metabolic process.

They may also be used in nuclear medicine imaging, in which contrast arises mainly from differences in the accumulation of administered radioactivity in body organs as a function of time. Nuclear medicine imaging was the area of emphasis of this research, therefore this discussion will focus on the imaging applications of radiopharmaceuticals.

The majority of nuclear medicine images are planar studies, of which there are two main categories - static and dynamic. In static studies the radiopharmaceutical localizes in an organ or tissue which is then imaged. In dynamic studies the radiopharmaceutical washes into and out of an organ, which is sequentially imaged, giving a series of pictures representing the progress of the labelled compound through an organ.

Computed tomographic imaging is available in nuclear medicine, but is an emission, rather than a transmission, technique and is known as single photon emission computed tomography or SPECT. Since it is the subject of this work, detailed discussion of SPECT imaging will be postponed until the appropriate sections.

Another tomographic technique, positron emission tomography (PET), is often included in the area of nuclear medicine. PET is similar to SPECT but requires radionuclides which emit positrons, for example oxygen-15, carbon-11 and nitrogen-13. These are intimately involved in metabolic processes and are therefore medically interesting. The annihilation radiation is

detected, using coincidence electronics, and used to reconstruct images, which are again primarily functional. The advantage is that the probability of detection of the photons is independent of the position of the emitter, in the patient, along the straight line between the detectors. In addition, the spatial resolution is better than in SPECT, as is the sensitivity (because absorptive collimators are not required - see I(b)(iii)). Its main disadvantage is that the necessary radioisotopes have short half-lives and require an on-site cyclotron for their production. For many centres this is prohibitively expensive.

(iii) ULTRASOUND IMAGING.

Short pulses of high-frequency sound are transmitted into the medium and the reflected and scattered energy is detected. The echoes are used to create a map which provides information on the mechanical properties of the tissues being imaged. Ultrasound has a major advantage in that it involves no exposure to ionizing radiation. Unfortunately, it cannot be used to image all body parts,

since bone and air cause too much reflection. However, it is extensively used in abdominal, obstetrical and cardiac imaging.

(iv) MAGNETIC RESONANCE IMAGING (MRI)

In the presence of a suitable magnetic field, atomic nuclei having an odd number of protons or neutrons absorb energy (i.e. they resonate). Absorption is almost instantaneous while the subsequent relaxation, or energy loss, is very slow, depending on the molecular structure and motion. This relaxation time is measured, and corresponding spatial information is obtained, by using field gradients. Image reconstruction is performed by computer and two and three-dimensional structural maps of the object of interest can be obtained.

Contrast in these images depends upon a complex group of factors including proton density, resonance relaxation times and chemical factors, which make it possible to obtain, from a given MRI image, a wide range of useful diagnostic information, related to anatomical structure

and physiological function. In this respect, magnetic resonance images are similar to nuclear medicine images, which also provide morphological as well as physiological information, and differ from conventional X-ray images, which provide mainly structural information.

At present, the major use of this modality is in proton imaging, although several other elements, such as carbon-13, fluorine-19, phosphorus-31 and sodium-23, seem to have potential as diagnostically useful nuclei. MRI can also be utilised for spectroscopic applications.

(b) NUCLEAR MEDICINE**(i) RADIONUCLIDES**

The ideal radionuclide for use in nuclear medicine should have the following properties:

A. Pure gamma emitter

Of the ionizing radiations (alpha, beta and gamma), gamma is the least ionizing. The presence of alpha or beta emissions makes no contribution to the diagnostic image. Usually internally absorbed, they merely increase the radiation dose to the patient without producing any benefit.

B. Optimum energy for penetration of patient and detection

The energy of the radiation must be such that it can penetrate the soft tissue and emerge from the body, otherwise it cannot be detected. In order to optimize detection and resolution, the energy of the emitted photons should lie inside a particular range. For gamma

cameras (discussed in I(b)(ii)), which are the most commonly used imaging devices in nuclear medicine, this range is between 100 and 200 keV.

C. Convenient half-life

The radionuclide half-life must be sufficiently long that it may be prepared, stored, injected, may localize in the organ and still emit enough radiation to form a good image. It must also be short enough to minimize the radiation risk to the patient. The physiological half-life, which is a measure of the length of time the radionuclide spends in the body, is also important. For example, a radionuclide with a long radioactive half-life may be used if its physiological half-life is short.

D. Convenient to produce

If the radionuclide has to be produced in a fission reactor or a cyclotron, it may be difficult to obtain, and this will impede its usefulness.

E. Suitable chemical properties

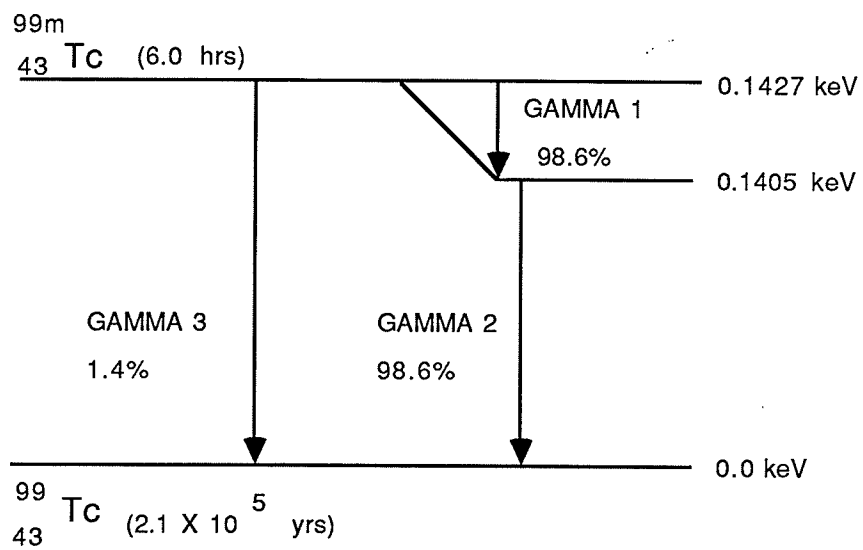
The chemical properties of the radionuclide must be such that it can be combined with physiologically useful

compounds, yielding a radiopharmaceutical which is stable.

Not all radionuclides will fulfil these criteria; a few of the more important radionuclides used in nuclear medicine are: gallium-67, technetium-99m, iodine-123, iodine-131, xenon-133 and thallium-201. Several other radionuclides are also used, and these are listed in texts on the subject (McAinsh, 1986, Johns and Cunningham, 1983, for example).

Of all the radioisotopes used in nuclear medicine, the most important is technetium-99m (Tc-99m). Its decay scheme, shown in Fig.1.1, shows that particulate emissions are absent, and that it emits a 140 keV photon which is easy to detect outside the body. It has a convenient half-life of six hours, and is easy to produce as required, from commercially available molybdenum generators. It may be combined into a wide variety of clinically useful compounds, permitting its use in imaging of the brain, liver and spleen, kidneys, lungs, bone and others. Technetium-99m is the isotope used in the work reported here.

Fig.1.1 Decay scheme of Tc-99m.

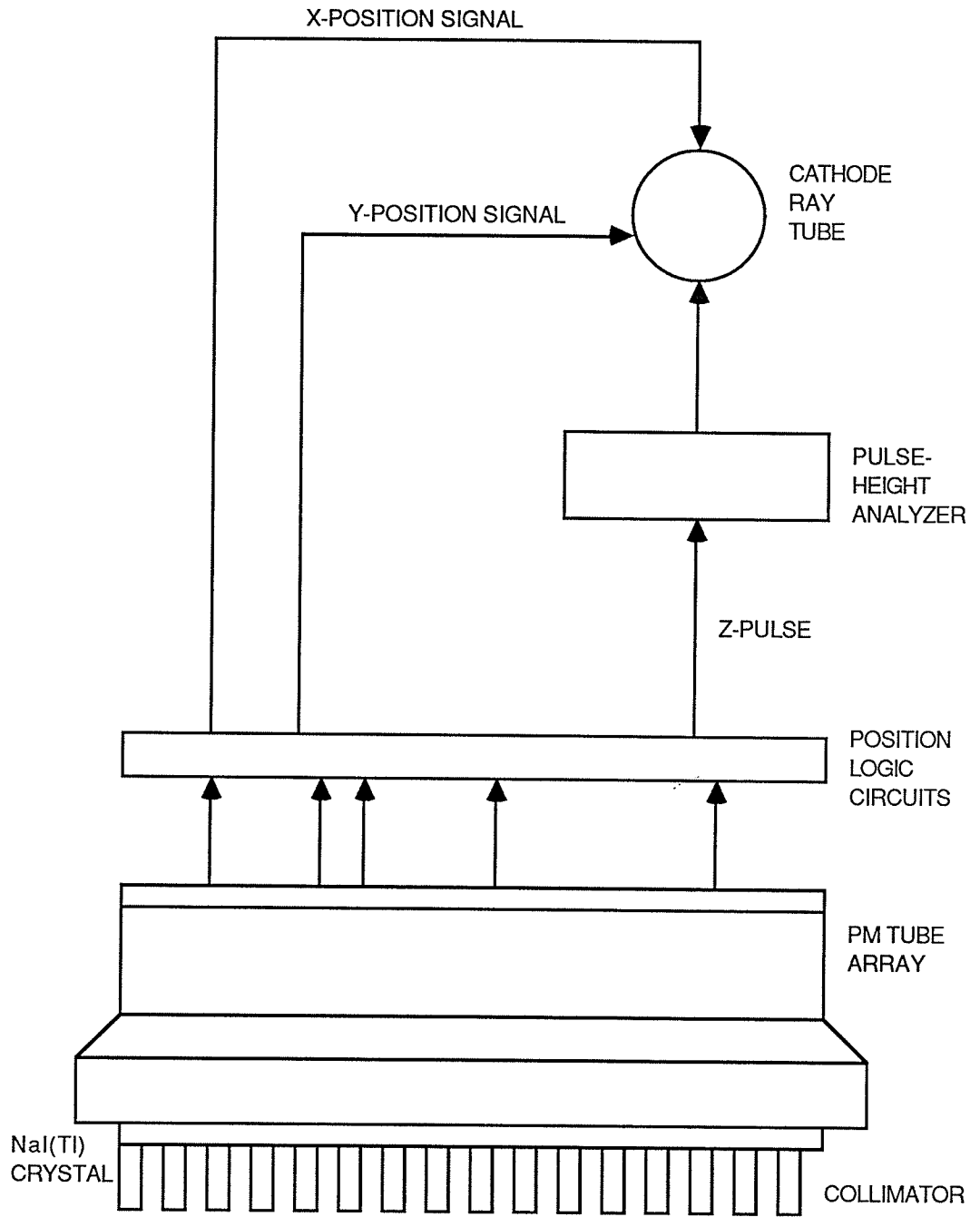


(ii) THE GAMMA CAMERA.

The gamma camera can produce an image showing the distribution of a radioactive source in the body of a patient. While individual types of gamma camera are not identical, they all have a number of features in common. These are shown in Fig.1.2.

The collimator projects the gamma image to the crystal. Those gamma rays not travelling in the direction dictated by the collimator septa are absorbed by them, while the remainder pass through the holes in the collimator and reach the crystal. In the crystal, the gamma photons produce scintillations which give a low intensity two-dimensional image of the distribution of the radioactivity, within the object or body being imaged. The image on the crystal cannot be viewed directly or photographed at this stage, but is detected by the photomultiplier (PM) tubes and converted into an image of electrical pulses. The PM tubes also amplify (or increase the intensity of) the image, providing gains of the order of 10^9 to 10^{10} .

Fig.1.2 Main features of the gamma camera.



The electrical pulses from the PM tubes now enter the electronic position logic circuits, which create three specific signals for each gamma photon detected by the camera. Two of these signals refer to the spatial location of the scintillation event in the image, while the size of the third pulse represents the energy of the photon. This last pulse enters the pulse height analyzer (PHA), and if it is within the selected energy range (window) it is recorded. Then the position signals deflect the electron beam of a cathode ray tube, to produce a flash on the screen at the location corresponding to the location on the crystal, and therefore within the patient's body. Each gamma photon detected on the crystal and accepted by the PHA produces one dot on the screen of the cathode ray tube (CRT). The image may be photographed or stored by computer for processing, viewing and analysis later.

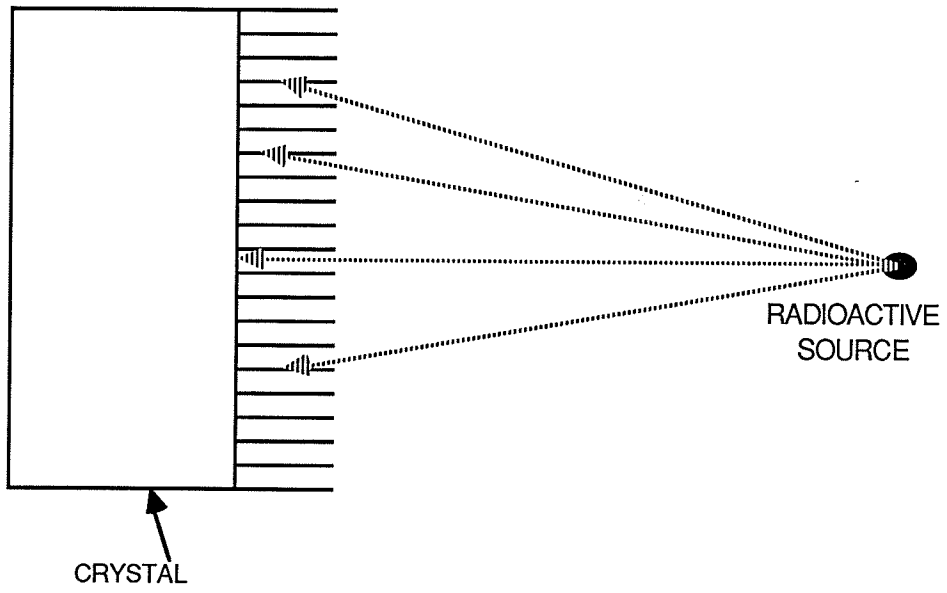
Let us now look in more detail at the various components of a typical gamma camera.

Collimator.

A collimator is used to "project" an image of a radioactive distribution onto the surface of the camera crystal. It is made from a metal, such as tungsten or lead, which is a good absorber of photons, and usually contains thousands of holes very close together (an exception to this is the pinhole collimator, discussed later). The collimator is constructed, such that each point on the crystal has a direct view of only one point on the surface of the body, which contains the radioactivity. Gamma photons, which are not travelling in the direction specified by the holes in the collimator, are absorbed by the collimator septa before reaching the detector, as illustrated by Fig.1.3. This is an inefficient process in that a lot of useful information is lost, and is a major cause of the relatively poor quality of radionuclide images.

The thin dividing walls, or septa, of a collimator are intended to prevent penetration of photons. However, in any given material, the penetrating power of incident photons usually increases with increasing photon energy.

Fig.1.3 Function of a collimator.



Therefore, relatively thin septa are adequate when using low-energy photons, while high-energy photons require thicker septa to prevent photons from crossing into adjacent holes. When the septal walls are thin, as in a low-energy collimator, it is possible for the collimator to contain more holes per unit area, and therefore to have increased sensitivity, which is advantageous. However, if this type of collimator is used with high-energy photons, there will be significant septal penetration of the thin walls leading to decreased resolution. On the other hand, if a high-energy collimator (with correspondingly thicker walls) is used with low-energy photons, the spatial resolution will be as normal, but the sensitivity of the camera will be less than optimal. A compromise exists between spatial resolution and sensitivity - for a given photon energy, a collimator can be selected to give maximum sensitivity, at the expense of reduced resolution.

The performance of any collimator depends on the shape, length and diameter of the holes. For a given septal thickness, the shape of the holes is selected to maximize the area of detector surface which is exposed.

The holes are usually round or hexagonal in cross-section, and arranged in a hexagonal close-packed array.

The collimator resolution, R_c , is given by:

$$R_c \approx d(l_e + b)/l_e \quad (1)$$

where b = distance from radiation source to collimator

d = diameter of holes

$l_e = l - 2\mu^{-1}$ = "effective length" of collimator holes

l = actual length of collimator holes

μ = linear attenuation coefficient of collimator material.

The efficiency of the collimator, g , is defined to be the fraction of gamma rays which pass through the collimator, for every gamma ray emitted by the source. For a source in air:

$$g \approx K^2 (d/l_e)^2 \cdot [d^2/(d + t)^2] \quad (2)$$

where t = septal thickness

K = constant, depending on hole shape.

Consideration of equation (1) indicates that, as the ratio of hole diameter to effective length (d/l_e) is decreased, the resolution improves; therefore, long, narrow holes in the collimator produce the best resolution. Equation (2) indicates that the collimator efficiency decreases approximately as the square of the ratio of hole diameter to length $(d/l_e)^2$. Consequently, to a good approximation, we may say that g is proportional to R_c^2 . In physical terms, this means that, for a given septal thickness, factors which improve the collimator resolution will decrease the collimator efficiency, and vice versa. (In fact, the existence of this compromise has already been indicated, earlier in this section, but is here confirmed in a more rigorous way.) However, increasing the septal thickness decreases the efficiency of the collimator.

As the distance, b , from the source to the collimator is increased, the resolution becomes poorer; therefore, those structures which are closest to the collimator are imaged in the greatest detail.

For a source in air, the efficiency of the collimator

is independent of the distance b , provided the count-rate for the entire detector area is included. This is because the efficiency of transmission of the radiation through any one collimator hole decreases in proportion to $(1/b^2)$, while the number of holes available for the radiation to use to reach the detector is proportional to b^2 ; these effects cancel and so collimator efficiency is independent of the distance between the source and the collimator. However, this does not apply when the gamma radiation is emitted by a source within a patient as attenuation by the body tissue must then be considered. Other factors which must be considered are septal penetration, and scatter of the photons from the walls of the holes in the collimator.

With respect to the orientation of the collimator holes, there are four main types of collimator.

1. Parallel-hole collimators, Fig.1.4(a). The holes are parallel to each other in this, the most commonly used, type of collimator. The image is neither magnified nor minified and the sensitivity is generally not affected by altering the distance between source and camera.

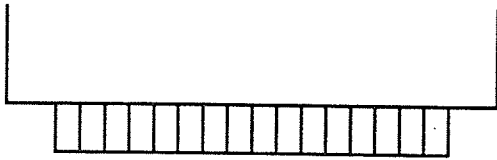
2. Diverging collimators, Fig.1.4(b). The holes diverge

from the detector face resulting in a minified image and a magnified field of view. This type of collimator is used mainly to enable cameras with small detectors to image large organs (e.g. liver, lungs). For a source, of activity sufficient to fill the field of view of the camera, the sensitivity of the camera decreases, with increasing distance, between the source and the camera.

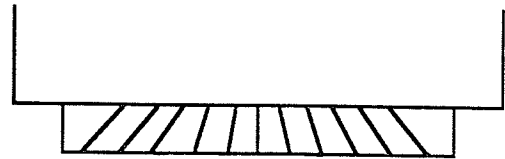
3. Converging collimators, Fig.1.4(c). The holes converge to a point in front of the collimator, resulting in a magnified image and increasing sensitivity as distance between camera and source is increased, again, for a source of sufficient activity to fill the field of view of the camera. It may be used for imaging small organs such as the thyroid gland.

4. Pinhole collimator, Fig.1.4(d). This has a single, small hole, rather than the several thousand holes present in the other types. It produces an inverted image of the source on the crystal, and may be used to give a magnified or minified image, depending on the distance between the source and the collimator. Since it has only one hole, it is less sensitive than the multihole collimators already mentioned.

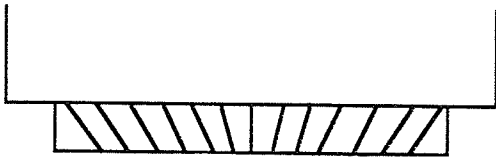
Fig.1.4 Types of collimator.



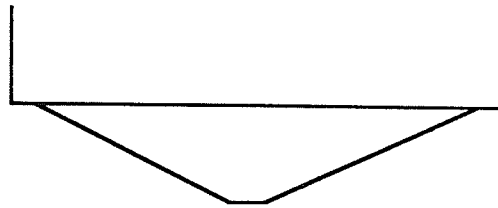
(a) PARALLEL-HOLE
COLLIMATOR



(b) DIVERGING COLLIMATOR



(c) CONVERGING COLLIMATOR



(d) PINHOLE COLLIMATOR

Thus, when selecting a collimator for a given application it is necessary to consider its effect on camera sensitivity and resolution, field of view, image magnification and image blur.

Scintillation crystal.

The two functions of the crystal are to absorb the gamma photons and to convert the gamma image into a light image. These crystals are usually in the form of disks, the diameter of which establishes the size of the field of view (which may then be modified by the choice of collimator and the source-camera distance). Typically, the crystal diameter is of the order of 20 to 50 cm and the thickness about 0.5 to 1 cm.

Within the crystal, a gamma photon will lose energy, via a photoelectric or Compton interaction, to electrons, which then travel a short distance, within which they undergo around 5000 interactions. The electron loses kinetic energy as a result, causing the crystal to scintillate. For gamma cameras, relatively thin crystals (around 0.5 cm thick) are preferred. These are less

efficient than thick crystals as radiation detectors, but give better intrinsic resolution and therefore improved image detail. The most common type of crystal used is sodium iodide doped with thallium, written as NaI(Tl). The impurity atoms (thallium) disturb the crystal lattice, which greatly increases the scintillation efficiency at room temperature.

Photomultiplier tubes (PMT).

The image is detected and amplified by an array of PM tubes placed behind the crystal. In modern, circular field of view, cameras there are generally 37, 61, 75 or 91 tubes, which may be round or hexagonal, arranged in a hexagonal pattern. The crystal and tubes are enclosed in a light-tight, magnetically shielded and lead-lined protective casing.

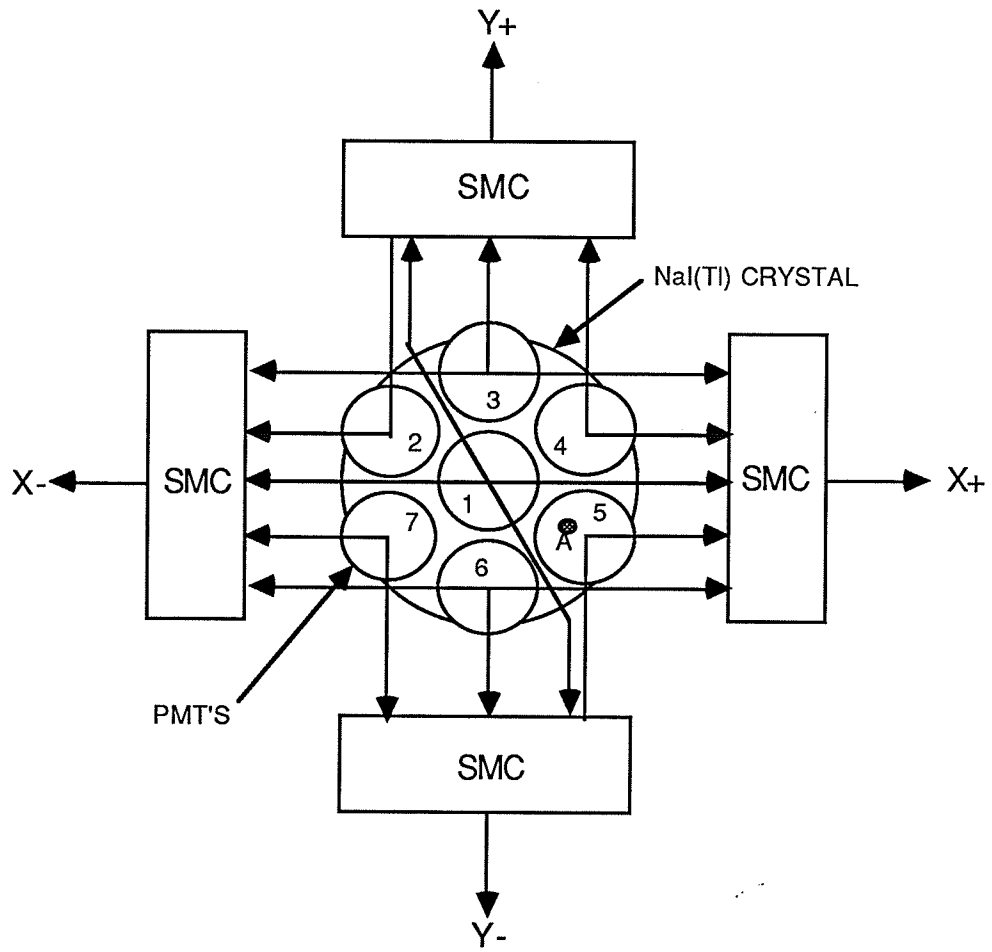
Positioning circuitry.

To transfer the crystal image to the viewing screen, it is necessary to know where, in the crystal, each gamma photon is absorbed. To help explain how the event-

positioning circuitry works, consider the hypothetical 7 tube camera shown in Fig.1.5 ; this was, in fact, the number of PM tubes in the first gamma camera. Consider a scintillation event at A in the crystal, and viewed by the PM tubes. The tubes closest to A receive most light and therefore produce outputs of larger amplitude. The outputs of tubes 1,3,4 and 5 are combined in a summing matrix circuit (SMC) to form the composite signal X^+ ; the outputs of 1,2,3,6 and 7 give X^- . Similarly, division of the array into vertical halves and summing appropriate outputs gives Y^+ and Y^- . Since A is towards the right and lower section of the crystal, the X^+ signal is greater than the X^- signal, and the Y^- signal is greater than the Y^+ signal.

The outputs of all 7 tubes are combined to give a Z signal, the amplitude of which is proportional to the total amount of light produced by the event in the crystal.

Fig.1.5 Schematic drawing of a gamma camera with seven PM tubes.



The X-position and Y-position signals are obtained by combining the X^+ , X^- , Y^+ and Y^- signals and normalizing with respect to Z:

$$X = k(X^+ - X^-)/Z \qquad Y = k(Y^+ - Y^-)/Z$$

where k is a scale factor determined by the deflection voltage characteristics of the CRT.

The X, Y and Z signals then go to the PHA and viewing unit.

Pulse-height analyzer.

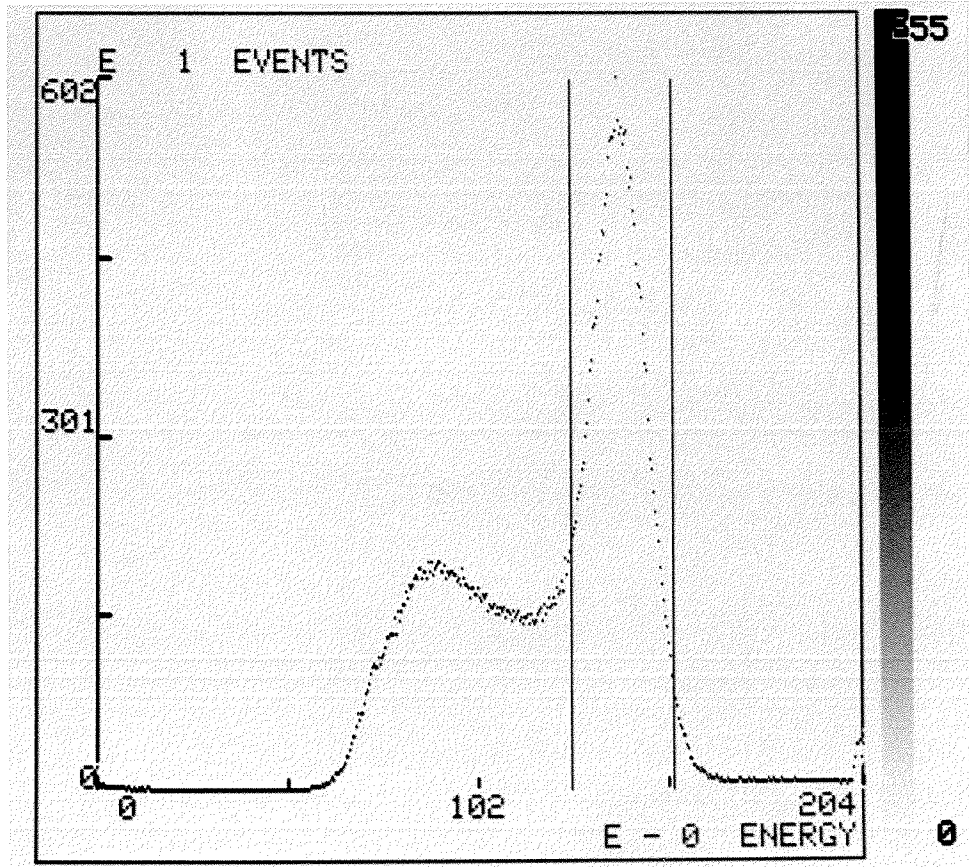
The PHA is a particular type of spectrometer (a device which permits the operator to select and use a specific portion of a spectrum). Pulses from the detector must pass through the PHA to be included in the image, the special feature of a PHA being that it may be set to exclude pulses other than those of a specified height or energy. The permitted pulse sizes are determined by setting the baseline and the window - the baseline specifies the minimum pulse amplitude that will be

accepted, and the window specifies the range of pulse amplitudes that will be accepted by the PHA.

The pulse-height scale is usually arbitrary, but the detector and amplifier may be calibrated to make the PHA scale correspond to a specific photon energy range. Thus, a PHA with a baseline setting of 60 pulse height units and a window width of 40 units, will accept pulses in the range 60 units to 100 units. With appropriate calibration, this could be made equivalent to an energy range of, say, 120 keV to 200 keV.

The window is generally positioned over the required portion of the spectrum, for example, the photopeak, as shown in Fig.1.6. Thus, a wide window setting increases the rate of counting of photons, and images can be formed faster. However, the ability to discriminate between the desirable and undesirable parts of the spectrum is reduced.

**Fig.1.6 PHA window positioned on the photopeak of a
Tc-99m spectrum.**



Consider again the signals originating from the camera shown in Fig.1.5 and mentioned earlier. If the energy (Z) pulse is within the range which allows it to be accepted by the PHA, it is directed to the CRT. It turns on the electron beam and causes a spot of light to be formed on the screen at a position determined by the X-position and Y-position signals. The spot of light on the screen is the image of a single gamma photon from the object or body being imaged. For every photon accepted by the gamma camera, this process is repeated, building up the pattern of spots which comprise the image.

(iii) CAMERA CHARACTERISTICS.Sensitivity.

Consider a distribution of radioactivity in a body or phantom, being imaged by a gamma camera. Photons emitted from this source distribution are equally distributed in all directions. However, only those which pass through the appropriate collimator hole and are absorbed in the crystal contribute to the image - the remainder are effectively wasted. The sensitivity of a gamma camera may be specified by the number of photons thus detected and used in the image, for each unit of radioactivity.

As already mentioned, the sensitivity is affected by the collimator design, although it must be remembered that the collimator which gives maximum sensitivity usually produces minimum spatial resolution.

Crystal thickness is also important because when photons pass completely through the crystal both detector efficiency and camera sensitivity are reduced. However, while a thicker crystal improves the sensitivity, it

usually compromises the spatial resolution.

Since the only photons which contribute to the image are those which are accepted by the PHA window, camera sensitivity may be significantly reduced by a too narrow or incorrectly positioned window.

Image quality.

This is determined by the characteristics of the camera components, the manner in which it is operated, the characteristics of the radiopharmaceutical (with respect to its efficiency of uptake into the organ of interest, its chemical stability, etc.), and by the patient (with respect to thickness of patient cross-section, ability to remain still, etc.). In this work, the images are obtained using a phantom; therefore only the camera characteristics are effective.

Image quality is generally assessed in nuclear imaging in terms of:

1. contrast
2. resolution
3. image noise
4. uniformity
5. distortion

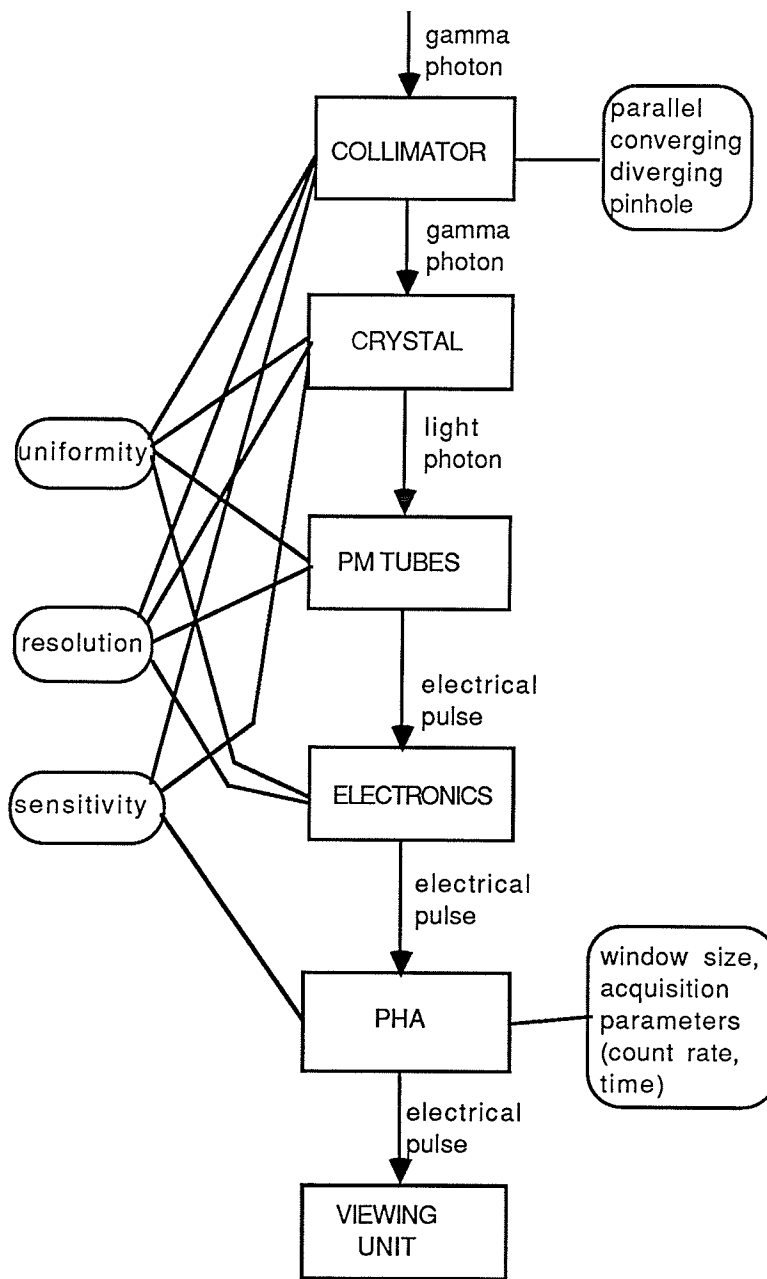
The main components of a gamma camera system and their relationship to each other and to the camera characteristics are summarized in Fig.1.7.

Fig.1.7 The components of a gamma camera system.

DEPENDENT
CAMERA
PARAMETER

CAMERA SYSTEM

OPERATOR
CHOICE



(iv) IMAGE CHARACTERISTICS.Contrast.

For an image of an object to be visible, it must differ from, or stand out against, the background - this is what is meant by the term "contrast". The amount of contrast refers to how much difference there is between the image and the background. Clearly, if its contrast is too low, the image of a given object will not be visible. The amount of contrast required for an image to be visible depends on several factors, including the size of the object and the background.

Contrast exists either when the radiation from the object area is more intense than the radiation from the background (a "hot" object), or when the radiation from the object area is less intense than that from the background (a "cold" object).

The radiation contrast can be measured and expressed in terms of the percentage difference between the object and background areas. The radiation making up the

background could be due to such factors as: radiation from the same radionuclide in surrounding tissue, radiation from other nuclides within the patient, scattered radiation and radiation from external sources.

The PHA may be used to discriminate between object radiation and background scatter. Eliminating this scattered radiation, which is of lower energy than the primary radiation, will improve contrast. This may be very effective as, in many cases, background scatter is the main cause of reduced contrast. Section I(d) and (e) address this topic in more detail. Similarly, if another radionuclide is present, and if the difference in their photopeak energies is sufficiently large, discrimination is possible using the PHA.

The term "contrast" is also applied to the image when it is recorded on film or displayed on a screen, however it is then referring to a difference in the optical densities of the object and background regions. The contrast may then be adjusted using the intensity control (for exposing films) or the contrast control (for screen displays).

Uniformity.

The sensitivity of a gamma camera should be uniform across the total image area if it is to produce images which show accurately the distribution of radioactivity. Non-uniformity (i.e. non-uniform sensitivity) usually results if the PMT outputs are not correctly balanced. Uniformity should be checked periodically using a flood source. In most modern gamma cameras, microprocessors are used to correct for non-uniformities in the array of detectors.

Spatial distortion.

In transferring the image from the crystal to the viewing screen, some points within the image may be moved with respect to each other, causing distortion of the size and shape of objects in the image. A gamma camera may be checked for spatial distortion using a test object, in which there is a series of uniformly spaced lines or holes, and determining if the image also exhibits uniform spacing. In fact, a large percentage of the non-uniformity just discussed is caused by spatial

distortion.

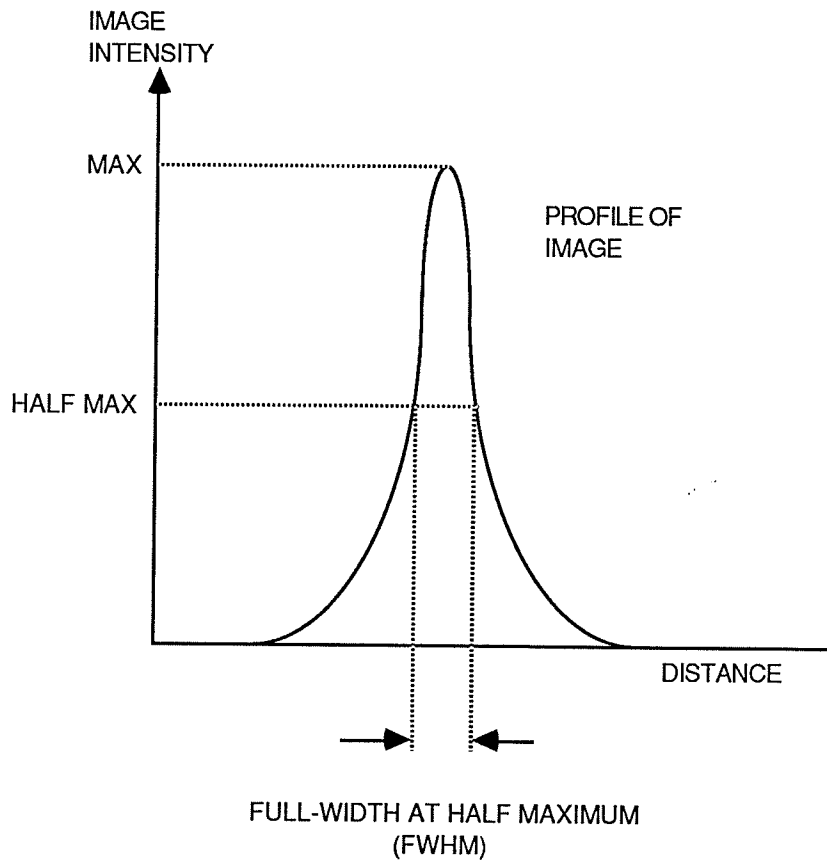
Spatial resolution.

The spatial resolution of an imaging system is defined as the ability of the system to resolve or separate small objects which are close together. It is affected by the blur characteristics of the system, which cause the image of an object point to be a circle with maximum intensity at the centre, decreasing gradually towards the periphery. Blurring is caused by such factors as motion of the object (or patient) during the imaging procedure, diffusion of light within the crystal (which is proportional to crystal thickness), and unsharpness due to the finite size of the collimator holes. Blur and resolution are inversely related.

Consider the profile of the image of a small radioactive source (for example, a drop of water containing Tc-99m) in Fig.1.8. Generally, the size of the image is expressed as the diameter of a circle positioned at half the maximum intensity, which corresponds to the full-width at half-maximum (FWHM) of

the profile, and may be used to measure the amount of blur in the system. Since resolution is inversely related to blur, this kind of measurement may be used to indicate the resolving capabilities of the system.

**Fig.1.8 Profile of the image of a small
radioactive source.**



(v) PLANAR IMAGING AND SPECT (McAinsh, 1986, Sorenson and Phelps, 1987)

Conventional nuclear medicine imaging is planar, in the sense that the images are two-dimensional projections of three-dimensional distributions of radioactivity. While these images are certainly useful, they have limitations, in that information from all depths is condensed and overlaid. The image of a structure at a given depth is obscured by the images of structures that are above and below. There is, therefore, a loss of image contrast which makes it difficult to distinguish regional changes in radionuclide distributions and to make an accurate evaluation of the shape, size and location of body organs.

In an attempt to gain some appreciation of three-dimensional structure, it is common practice to obtain multiple projections at different angles, for example, posterior, anterior, lateral and oblique projections. However, the physician reading the images is then required to combine mentally the different projections, and decide the nature of the three-dimensional

distribution of radioactivity. While this approach is successful to a degree, it is difficult to appreciate complex distributions in this way, or to visualize deep-lying organs, which will generally have many overlying structures at all angles.

Tomographic imaging is a more satisfactory approach to solving the problems described above. Tomographic images are two-dimensional representations of structures in a selected plane at a given depth in a three-dimensional object. X-ray computed tomography (X-ray CT), magnetic resonance imaging (MRI) and positron emission tomography (PET), all described earlier, are tomographic techniques, as is SPECT. In the next section the principles of SPECT will be discussed.

(c) PRINCIPLES OF SPECT

(English and Brown, 1986, Sorenson and Phelps, 1987)

Computed tomography techniques are based on rigorous mathematical algorithms. Although X-ray CT is a transmission technique, while SPECT is an emission technique, the basic principles of both are the same.

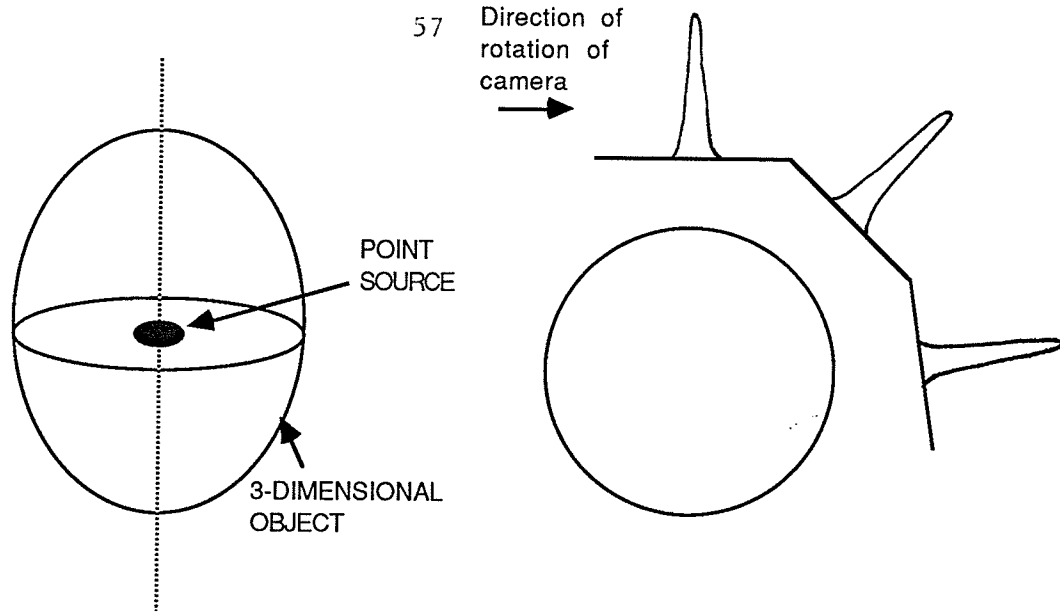
(i) RECONSTRUCTION OF IMAGES FROM PROJECTIONS

As the detector moves around the object, a set of two-dimensional projection images is acquired at angular intervals specified by the operator. These projections constitute the input data for the reconstruction process. Consider the simple case of a point source embedded in a three-dimensional object, Fig.1.9(a). If this is scanned at a series of angles, a set of projections such as those illustrated in Fig.1.9(b) are obtained. Although each individual projection indicates the position of the point source, in a direction parallel to the projection, the source could be anywhere along the line perpendicular to

the projection. As a first approximation, the information from each projection is projected back across the whole image (Fig.1.9(c)), i.e. each point in the original object plane, which contributes to the projection, is assigned an equal value. The resulting backprojection is added to the backprojections obtained from all other scans, to give an image of the object.

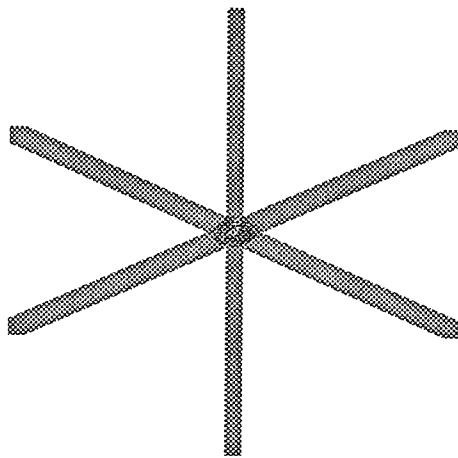
As shown in Fig.1.9(c), this image is considerably blurred. By increasing the total number of projections, or decreasing the angular interval, blurring may be decreased. However, it is not eliminated, even with an infinite number of projections, and so another way to improve the image quality must be found.

**Fig.1.9 Reconstruction of an image by
backprojection.**



(a) POINT SOURCE EMBEDDED IN A 3-DIMENSIONAL OBJECT

(b) TO ILLUSTRATE HOW THE CAMERA SCANS OBJECT, OBTAINING PROFILES AT VARIOUS ANGLES



(c) BACKPROJECTION, AND SUPERPOSITION OF PROFILES TO OBTAIN AN APPROXIMATION TO THE ORIGINAL SOURCE DISTRIBUTION

The blurring may be described (Sorenson and Phelps, 1987) by the function $1/r$, if r represents the distance from the point source. Now, the method just described for obtaining an image is known as "linear superposition of backprojections" or LSBP. Mathematically,

$$\text{LSBP} = \text{true image} * 1/r \quad (3)$$

where $*$ represents convolution (Bracewell, 1965).

Then, by taking the Fourier transforms, equation (3) becomes

$$F(\text{LSBP}) = F(\text{true image}) \times F(1/r) \quad (4)$$

since convolution in the spatial domain and multiplication in the frequency domain are equivalent. By rearranging (4) we obtain:

$$F(\text{true image}) = F(\text{LSBP})/F(1/r) \quad (5)$$

Now

$$F(1/r) = 1/f \quad (6)$$

where f = spatial frequency, so (5) may be written as

$$F(\text{true image}) = F(\text{LSBP}) \times f \quad (7)$$

The inverse Fourier transform of (7) yields

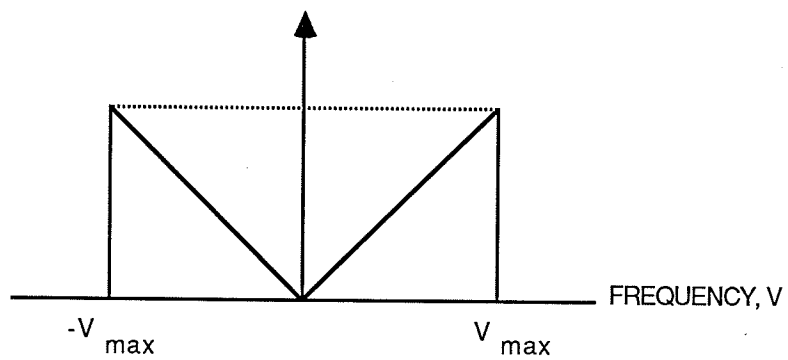
$$\text{true image} = \text{LSBP} * g \quad (8)$$

where g is some function in the spatial domain, which undergoes Fourier transform to give f in the frequency domain. Thus, there are two equivalent ways to eliminate the blur shown in Fig.1.9(c). The first method is to convolve each projection with a correction function or "filter" g ; the second is to obtain the Fourier transforms of the projections, and then multiply every frequency component by some factor which is proportional to the spatial frequency f .

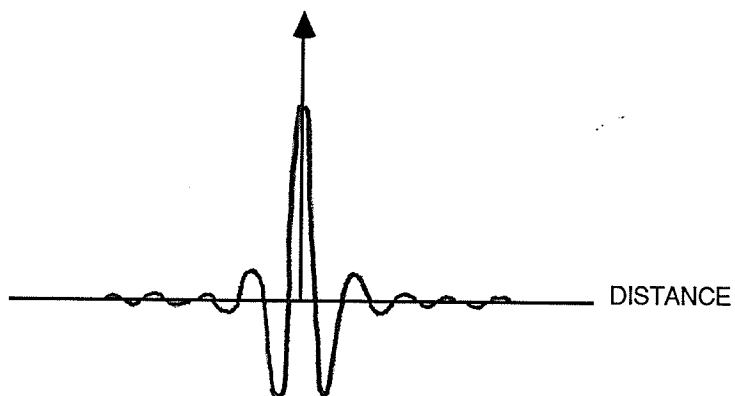
Filter functions.

The shape of the correction filter in both spatial and frequency domains is shown in Fig.1.10; it is often called a ramp filter because of its shape in the frequency domain. Fig.1.10 indicates that correction by this method is equivalent to increasing the representation of the higher spatial frequencies in the Fourier transform of the LSBP image, which corresponds with the practical situation, since the suppression of high frequency information is a major contribution to image blur.

Fig.1.10 Shape of ramp filter in frequency and spatial domains.



(a) FILTER TO CORRECT FOR $1/r$ BLURRING
(RAMP) IN FREQUENCY DOMAIN



(b) FILTER TO CORRECT FOR $1/r$ BLURRING
(FOURIER TRANSFORM OF RAMP) IN
SPATIAL DOMAIN

The filter functions used, in practice, fall off at high frequencies, to reduce the effects of excessive amplification of high frequency noise. Linear superposition of these filtered backprojections eliminates the $1/r$ blurring, as illustrated in Fig.1.11. Increasing the number of projections further improves the image.

The kinds of filters available to the reconstruction software, used in this work, are described in section II(d)(iv).

Windows.

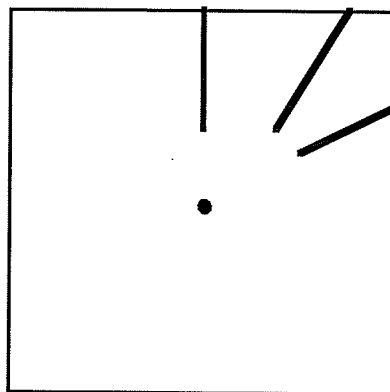
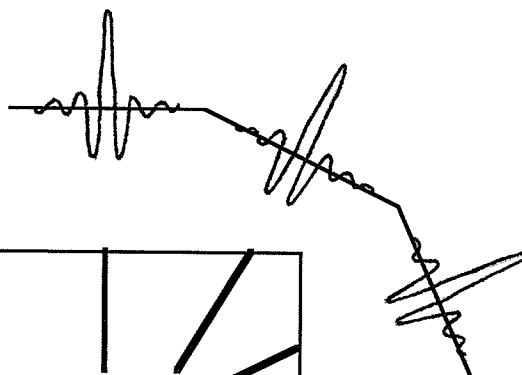
The ramp filter alone cannot be used in routine low-count SPECT examinations, since it includes the high-frequency noise in each projection. While this might be satisfactory if each projection was to represent millions of counts, SPECT data, reconstructed using only a ramp filter, exhibits overwhelming noise artifacts.

To improve the signal-to-noise ratio, the ramp is multiplied by a window function. The resulting function,

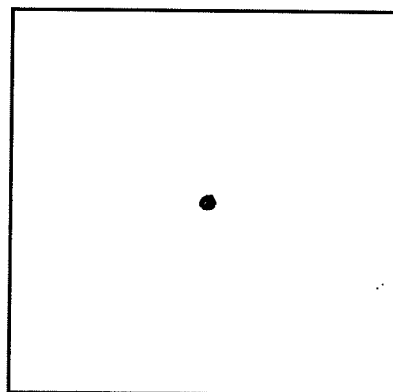
which is truncated at high frequencies, is used in the reconstruction process. The cut-off frequency of a window function may be altered, permitting the user to suppress selected high frequency components in the data as required. However, the inclusion of the lower frequency, background components of the image data is essential.

**Fig.1.11 Linear superposition of filtered
backprojections.**

SCAN PROFILES
AFTER APPLICATION
OF RAMP FILTER



(a) LINEAR SUPERPOSITION OF FILTERED
BACKPROJECTIONS



(b) EFFECT OF INCREASING THE NUMBER OF SCAN
PROFILES

Sampling.

The resolution in the reconstructed image is largely determined by, the linear and angular sampling intervals, the cut-off frequency of the correction filter, and the detector resolution.

According to the sampling theorem (Bracewell, 1965), the highest spatial frequency to be obtained must be sampled at least twice per cycle. Image artifacts (see next section), known as aliasing, result from sampling less often.

A compromise situation exists between detector resolution and filter cut-off frequency, as the limiting resolution in the final image is determined by the lower of the two. The sampling interval should be selected only after this limiting resolution is established.

(ii) ARTIFACTS

Artifacts are defined as being those parts of an image which do not exist in the original source distribution (English and Brown, 1986), and have many causes.

In SPECT imaging, performance standards which may be acceptable in planar imaging, may be the source of serious artifacts - hence the emphasis in the preceding discussion on suppression of noise. A gamma camera suitable for SPECT imaging must have linearity to within 0.5 mm across the camera face, and uniformity of 1 to 2%. The reasons for these stringent standards become apparent, upon consideration of a slight defect in the detector's field of view, resulting in an area of reduced counts. When this is tracked through a complete 360 degree rotation and reconstructed, a circular path of decreased counts results, and appears in the final image as a ring-shaped artifact. The significance of these artifacts is greater at the centre of the reconstructed image than on the periphery, since there are fewer pixels in each increment over which to distribute the defect.

The influence of these uniformity artifacts may be reduced, by correcting the planar projections with correction floods having very high counts (of the order of 30 million counts - giving a standard deviation of around 1%).

Misalignment of the centre of rotation of the gamma camera will cause misplacement of counts in pixels in the image, which may then indicate "hot" spots in areas which are, in fact, "cold". This problem may be caused by mechanical degradation in the gantry, movements of the crystal within the detector head, or shifts in the origin of the gamma camera coordinate system. It may be avoided by routine monitoring of these parameters, followed by adjustments when necessary.

Successful SPECT imaging requires that the performance characteristics of the system, be subject to a rigorous quality control program, accompanied by thorough maintenance. The camera system employed in this work is checked daily; tests include optical calibration of the photomultiplier tube gains and tests of flood uniformity. In addition, weekly tests of linearity,

spatial resolution and centre of rotation are performed, and sensitivity maps for Tc-99m are renewed at least every two weeks.

(d) PROBLEMS WITH QUANTITATIVE SPECT IMAGING

The aim of quantitative SPECT imaging, summarized by Floyd et al, (1986), is to determine the concentration of photon-emitting radiopharmaceutical inside a body, or body organ, by measuring the photon flux outside the body. However, there are many obstacles to be surmounted before this aim is realised. A major physical problem is posed by correction for the interaction of photons with matter, and it is in this area that this work has been concentrated.

Let us consider the kinds of problems which may arise as a result of this interaction. Between the emission source within the object and arrival at the detector, photons are lost - this process is called attenuation. Secondly, photons may arrive at the detector in such a way as to be falsely positioned in the image - this is due to scatter in the material between the emission source and the detector. Both attenuation and scatter arise from the kind of interactions which can occur between all high energy photons (such as gamma rays) and

atoms, nuclei and electrons, and which result in a transfer of energy from the photon to matter. The interactions may be viewed as simple "collisions" between the photon and a target atom, nucleus or electron. As a result of these collisions, electrons may be ejected and go on to cause the ionization effects which are used to detect high energy photons, and which cause radiobiological effects.

There are many possible interactions between photons and matter; Sorenson and Phelps (1987) suggest nine, while Beck (1982) quotes twelve. However, only three are directly relevant to nuclear medicine:

(1) the photoelectric effect is an atomic absorption process. An atom completely absorbs the energy of an incident photon, which then disappears. As a result of absorbing this energy, an orbital electron (called a photoelectron) is ejected from the atom.

(2) Compton scattering is the name given to a collision between a photon, and a loosely bound outer shell orbital electron. The interaction may be considered as a collision between a photon and a "free" electron, because the photon energy is so much greater than the binding

energy of the electron. As a result of the collision, the photon loses part of its energy to the electron, which then recoils, and the photon is deflected from its original path.

(3) pair production is caused by interaction of the photon with the electric field of a charged particle, usually an atomic nucleus. As in the photoelectric effect, the photon disappears, but in this case its energy is used to create a positive-negative electron pair. Occasionally, pair production may occur near an electron, which receives energy from the photon and is ejected from the atom. This is then termed triplet production.

The probability of occurrence of any one of these three kinds of interaction depends on the energy of the incident photon. Up to approximately 50 keV, the photoelectric effect is the most prevalent, and then Compton scattering becomes significant. Between approximately 100 keV and 2 MeV, Compton scattering is most prevalent in tissue. For pair production to take place, the photon must have an energy of at least 1.02 MeV, although this only gains importance for energies

greater than 5MeV. In nuclear medicine, as mentioned in I(b)(i), the photon energies typically are of the order of a few hundred keV, as illustrated by the examples listed below:

RADIOISOTOPE	PRINCIPLE PHOTON ENERGY (keV)
Ga-67	92,184,299,393
Tc-99m	140
I-123	159
I-131	284,364,637,723
Tl-201	135,166

The probability of occurrence may also depend on the atomic number, Z , of the medium through which the photon passes. In general, the probability of a photoelectric interaction depends on Z^3 , and it is therefore more likely to occur in materials of high atomic number, such as bone. The probability of Compton scattering is almost independent of atomic number, although it depends very strongly on the electron density of the medium. The probability of pair production varies in an almost linear fashion with the atomic number of the medium; in soft

tissue, it makes up only a small fraction of the interactions of photons with energies between 1.02 MeV and 10 MeV.

The relative importance of these three interactions, with respect to atomic number and photon energy, are summarized in Fig.1.12. The lines show atomic numbers and photon energies at which adjacent effects are equally probable.

These are the basic interactions which occur between photons and matter. In general, energy is transferred from the photon to matter via a series of these interactions, such as in Fig.1.13. It is as a result of such interactions that scatter and attenuation occur in nuclear medicine imaging. Each interaction produces secondary photons and/or electrons, which are ultimately responsible for the deposition of energy (by ionization and excitation) in matter.

**Fig.1.12 Relative importance of photoelectric effect,
Compton effect, and pair production.**

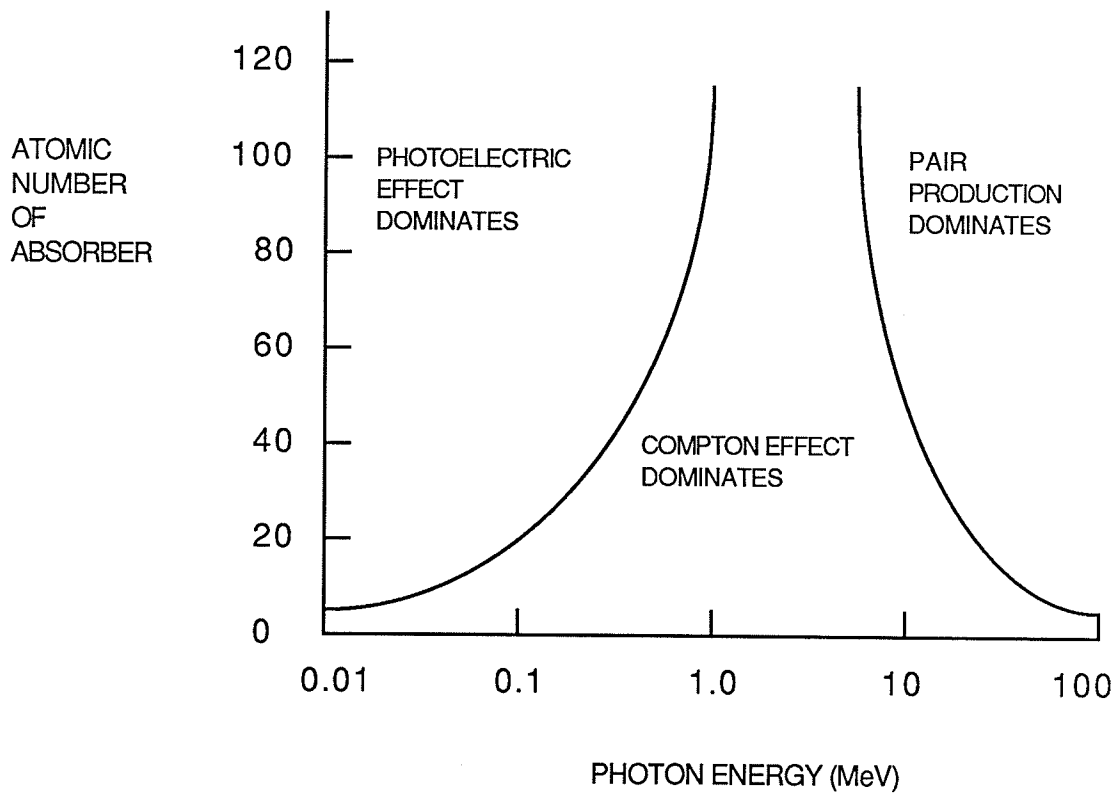
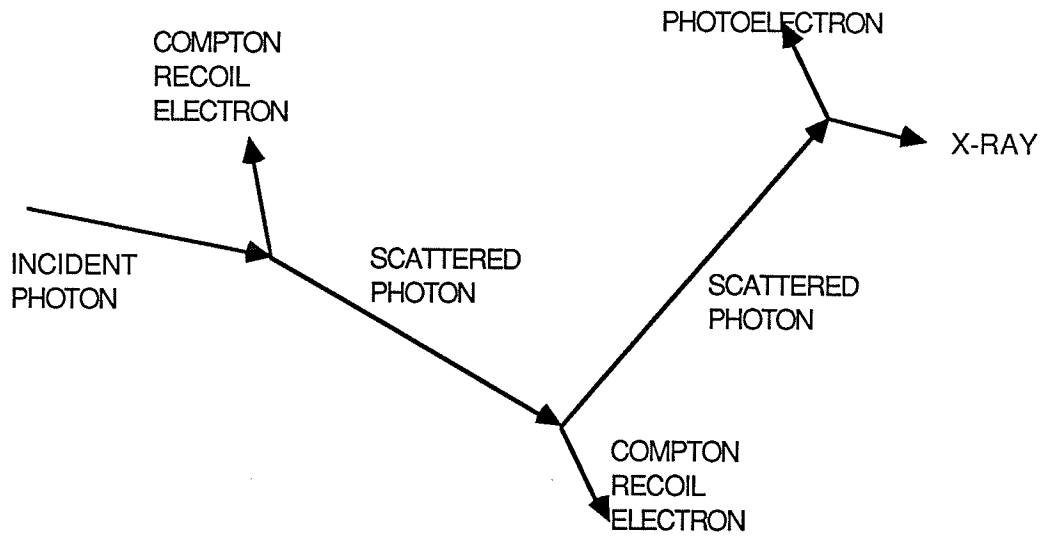


Fig.1.13 A possible sequence of interactions of a photon, passing through matter.

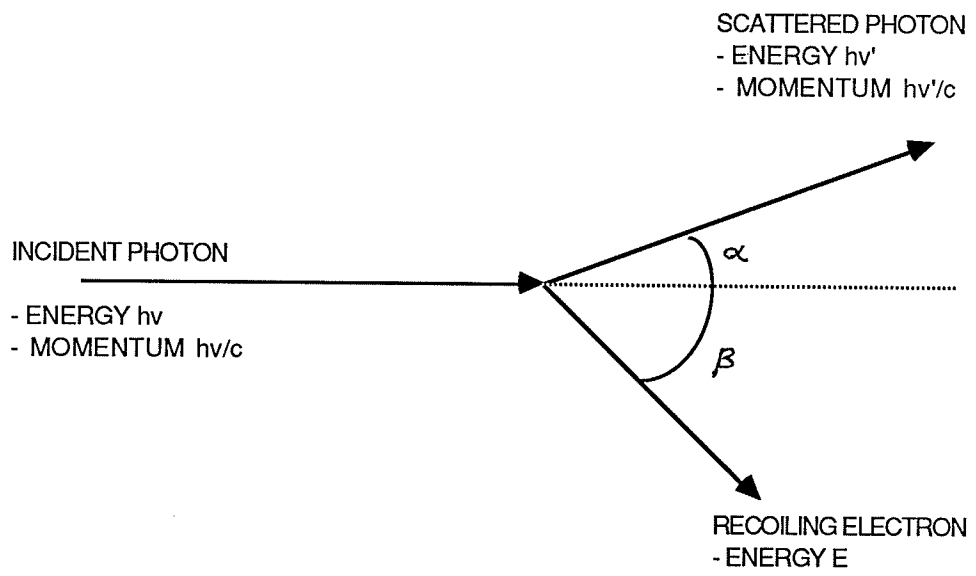


(i) SCATTERWhat is scatter?

As already mentioned, the gamma photon may interact with an electron in any of three ways. In tissue-like materials, at the energies typically encountered in nuclear medicine, it is most probable that the interaction will be Compton (or incoherent) scattering. The process is named after A.H.Compton who published the first accurate, quantum-mechanical description of this interaction (1923). He made the assumption that the scattering process may be considered as an elastic collision between a photon and a free electron, with energy and momentum being conserved in the collision.

As a result of a Compton collision some of the photon energy is transferred to an electron and some is scattered, the amounts of each depending on the angle at which the scattered photon is emitted, and the incident energy of the photon. A Compton collision is shown in Fig.1.14.

Fig.1.14 Representation of a Compton collision.



Energy is conserved in the collision so:

$$h\nu' = h\nu - E \quad (9)$$

i.e. the scattered photons have less energy than the incident photons.

If the incident photon makes a direct hit on the electron, the recoil electron travels straight forward ($\beta = 0^\circ$) and the scattered photon emerges with $\alpha = 180^\circ$ - in this case the energy transferred to the electron is maximum, while that transferred to the photon is minimum.

If the incident photon makes a glancing hit on the electron, the electron recoils with $\beta \approx 90^\circ$ and the scattered photon emerges almost in the forward direction ($\alpha \approx 0^\circ$). In this type of collision the scattered photon emerges with almost all of the energy of the incident photon, while the recoil electron emerges with almost no energy. These are the extreme cases - clearly, all kinds of intermediate collisions, with the electron and photon emerging with different proportions of the energy of the incident photon, are possible. A simple

expression can be derived for the energy loss, as a function of scattering angle:

$$E = hc/(1-\cos\alpha)\lambda_c \quad (10)$$

where $\lambda_c = h/mc = 2.43 \times 10^{-12}$ m is the Compton wavelength

$h = 6.626 \times 10^{-34}$ Js is Planck's constant

$m = 9.109 \times 10^{-31}$ kg is the electron rest mass

and $c = 2.998 \times 10^8$ m/s is the speed of light in a vacuum.

(Eisberg and Resnick, 1974)

The probability of this kind of collision is almost independent of atomic number, and decreases as the photon energy increases.

What is the effect of scatter?

Evaluation of equation (10) for an incident gamma ray photon of energy 140 keV, and scattered through 45° , reveals that the emerging photon will have an energy of

approximately 130 keV. This photon is very likely to be accepted by the PHA, and to be included in the final SPECT image. Thus, the effect of scatter is to include extra photons in the final image, and to alter the distribution of energies of radiation striking the detector.

The amount of scatter depends on many factors, including the source distribution, the shape of the scattering material, the distance between the scattering material and the detector, the size of the energy window, and its position on the photopeak.

The energy resolution of the detector is a particularly important factor, in that the scintillation detectors which are generally used have poor energy resolution, with the result that the number of scattered counts can be as much as 50% of the total collected in SPECT. A possible clinical implication is that a cold region deep within a patient may be observed as being radioactive, with up to 50% of the activity observed in neighbouring regions. This effect has been observed by many investigators using phantoms, for

example, Heller and Goodwin, (1987).

As the photon energy decreases, the scattered photon retains a progressively larger proportion of the incident photon energy. As the depth of the source within a scattering medium increases, so does the ratio of scattered to primary photons in the photopeak. The presence of these scattered photons adds a structured background to the projection images, with the result that lesion contrast and spatial resolution are decreased, making it more difficult not only to detect the lesions, but also to locate the lesion border.

For accurate quantification in SPECT, it is important to know the contour of the organ or lesion under study. Therefore scattered radiation is clearly one of the major factors which must be overcome, if quantitative SPECT is to become a reality. This is discussed in I(e)(i).

(ii) ATTENUATION (Sorenson and Phelps, 1987)

What is attenuation?

When a photon passes through matter, the probability that it will undergo an interaction, such as a photoelectric interaction, and be removed from the beam, depends on the energy of the photon, and the thickness and composition of the matter through which it passes.

We consider a monoenergetic photon beam, traversing a distance x of absorber, composed of a single element of atomic number Z . Only those photons which emerge from the absorber without interacting will be detected. In conditions of narrow beam geometry, the intensity, I_x , of the transmitted photon beam is given by:

$$I_x = I_0 e^{-\mu x} \quad (11)$$

where I_0 = intensity recorded in absence of the absorbing material

μ = linear attenuation coefficient of the absorber at the energy of the photon beam.

This equation governs the relationship between attenuation and distance (i.e. the greater the distance traversed, the greater the probability that a given photon will interact, and be removed from the beam). However, as mentioned above, the attenuation is also related to the absorbing material and the photon energy. Now, at lower photon energies, such as those used in SPECT imaging, the attenuation coefficient is greater than at higher energies. In addition, at the range of energies used in nuclear medicine, the predominant interaction of photons passing through material having $Z \leq 20$ (such as body tissue) is Compton scatter. Also, we have assumed that "narrow beam" conditions prevail, which is certainly the case for the individual narrow holes in the collimator, but is not true for the collimator in its entirety. If the combined effects of all the narrow holes in the collimator are considered, "broad beam" conditions are a closer representation of the practical situation. So there is, in fact, a very noticeable amount of scattering in the material surrounding the radiation source.

Thus, while corrections must be made for both

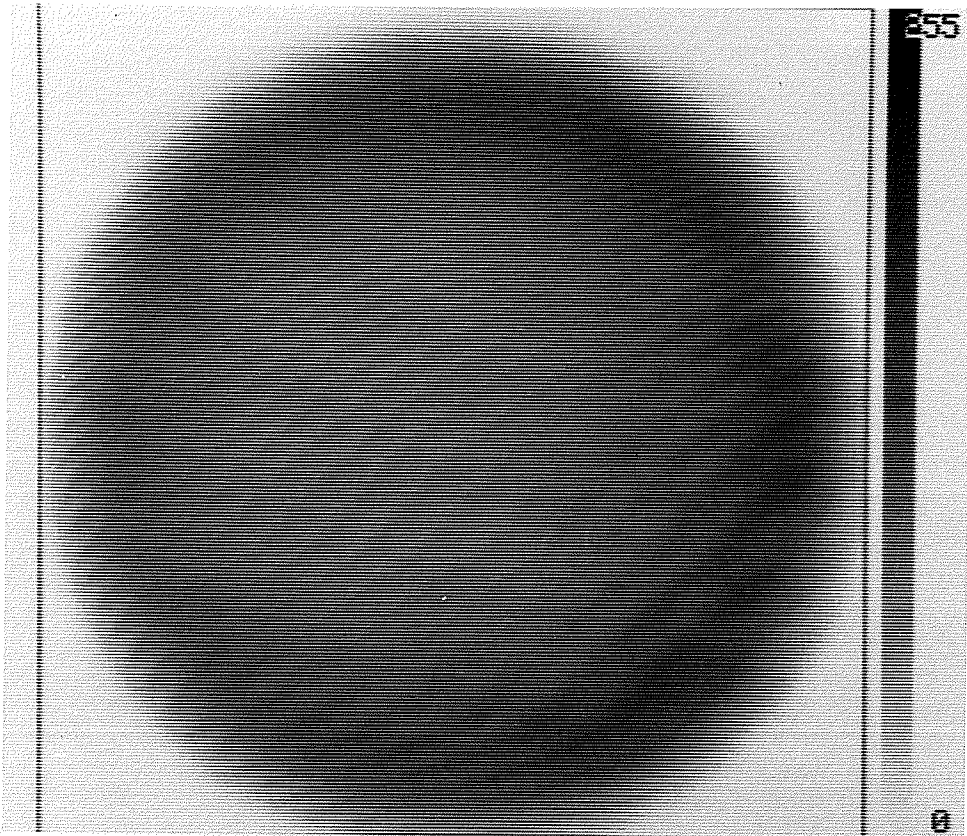
attenuation and scatter, it is more important to accurately compensate for scattering of radiation.

What is the effect of attenuation?

Since the same images could be obtained from a strong source X, attenuated by a distance x , and a weak source Y, attenuated by a shorter distance y , radionuclide images, including SPECT images, contain some ambiguity. They tend to mix information regarding the distribution of radioactivity, with information regarding the distribution of the attenuating medium.

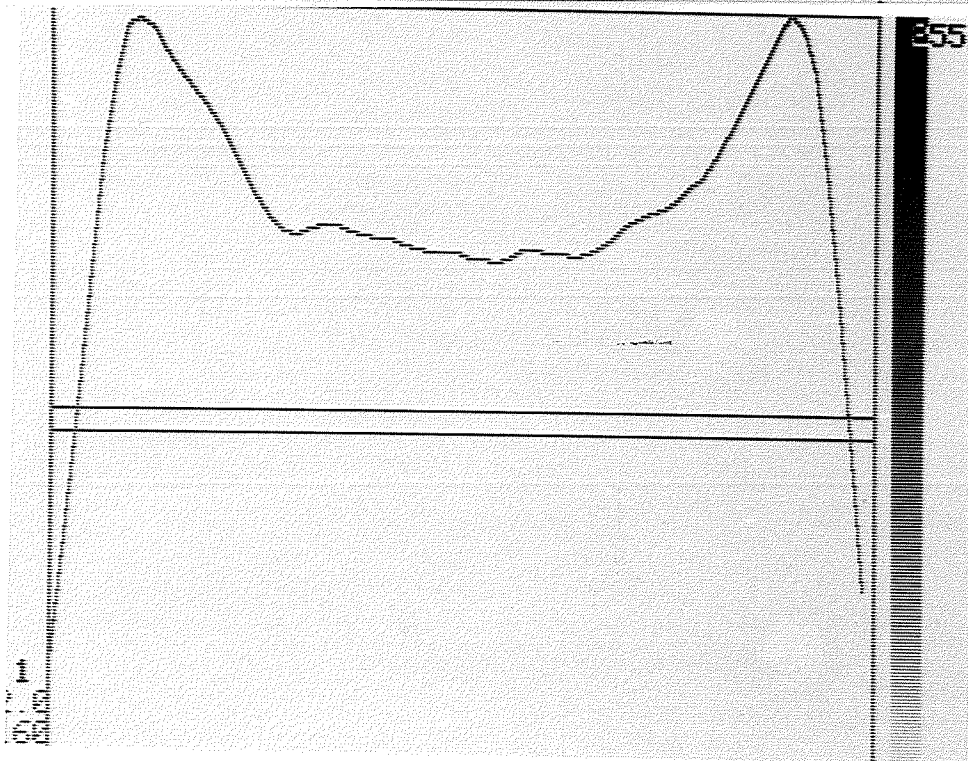
The effect of attenuation is illustrated by Fig.1.15, which is an image of a uniform "flood" phantom, reconstructed without any correction for attenuation. Beneath the image is a plot of the measured concentration of activity, along a horizontal line, through the centre of the cylindrical source. In the middle of the graph, a very marked decrease, caused by a loss of information due to attenuation and scattering, is indicated. This

Fig.1.15 Transaxial slice through a "flood" phantom, with corresponding count profile, along a line through the centre.



255

0



255

0.1
0.05
0.025

decrease makes it difficult to obtain, from SPECT images, accurate quantitative information on radiotracer uptake.

This reduction in counts can lead to problems when SPECT is used clinically; physicians are often faced with a decision as to whether a count reduction is caused by attenuation, or by reduced deposition of activity. Lesion contrast is reduced, making it difficult to detect small or deep lesions, or there may be a deformation in the perceived volume, which makes it difficult to evaluate the size of a lesion.

There are several other problems associated with quantitative SPECT imaging, for example, poor spatial resolution, the partial volume effect and image noise. This work focusses on the area of scatter and attenuation compensation, therefore the discussion in this section has been restricted to cover only these areas.

(e) CORRECTIONS FOR SCATTER AND ATTENUATION**(i) COMPENSATION FOR SCATTER**By reduced attenuation coefficient

Perhaps the simplest approach to scatter correction is to assume that a fixed fraction of the attenuated primary photons can be replaced by scattered photons, which behave like unattenuated photons (Jaszczak et al, 1981). A reduced value for the linear attenuation coefficient is used in the attenuation correction algorithms discussed later (I(e)(ii)).

By use of average scatter fraction

To use this approach, define the scatter fraction, SF_{avg} , as the ratio of scattered to unscattered photons (Jaszczak et al, 1984a). Then a first order compensation is possible, by assuming that the scatter fraction does not vary across the sectional images, or that if it does, even large variations in the value of SF_{avg} cause only

small errors in quantification of the parameter under study (Jaszczak et al, 1985a).

A value for average scatter fraction may be obtained experimentally, analytically (Jaszczak et al, 1985b) or from Monte Carlo simulations (Manglos et al, 1987; Floyd et al, 1984; Floyd et al, 1987) and may be used to correct quantitative measurements of the contrast (discussed in sections I(b)(iv) and III(f)) of a lesion image, and to obtain the uptake ratio C_{obj} of a radionuclide. The uptake ratio is defined as $(Q_s - Q_b)/Q_b$ where Q_s is the radionuclide concentration in a hollow sphere, located in a cylinder which contains a uniform source distribution of concentration Q_b . A more accurate estimate of uptake ratio, using the scatter fraction, is obtained from the equation (Jaszczak et al, 1985a):

$$C_{obj} = (C_{image}/CF_{avg})(1+SF_{avg}) \quad (12)$$

where C_{image} = SPECT measured image contrast for lesion

CF_{avg} = contrast loss factor due to the system's
spatial resolution

= reciprocal of the recovery coefficient

SF_{avg} = estimated value for average scatter
fraction in reconstructed SPECT image

and the recovery coefficient is the ratio of the apparent concentration of activity to the true concentration of activity in a specified test object or lesion.

Use of the average scatter fraction, in this way, can improve SPECT quantification of concentration ratios (Jaszczak et al, 1985b), but is flawed in the assumption of a uniform scatter image. In fact, the scatter image has a structure of its own, and so the absolute concentration of a radionuclide cannot be accurately obtained in this way.

By use of asymmetric or narrow energy windows

Photons which undergo Compton scattering, lose energy at each successive scattering event, so it would seem that a reduction in the number of scattered photons detected could be achieved, by using analyzer windows asymmetrically high on the photopeak (i.e. the lower energy cut-off is closer to the photopeak central energy than the higher energy cut-off), or narrower windows

(King et al, 1983). However, many scattered photons do not lose enough energy to be excluded by this type of energy window, and the energy resolution of a NaI(Tl) gamma camera is sufficiently poor (≈ 10 to 12%) that true photopeak counts will be excluded. Nonetheless, several investigators (King et al, 1983; Lewellen, 1982; La Fontaine et al, 1983) have noted improvement in lesion contrast and edge definition due to the use of asymmetric windows, while Croft et al, (1982), investigated the use of narrow energy windows. Graham et al, (1986), attempted to quantify the degree of asymmetry which produced 75 to 100% of the maximum improvement in resolution, but also noted that off-peak imaging produced flood non-uniformity to an extent which was unacceptable for SPECT, since it would lead to artifacts in the reconstructed images. They found that fairly small degrees of asymmetry, in the energy window, offered the greatest improvement in contrast and spatial resolution, and suggested that using highly asymmetric windows would not result in proportionately greater benefits and might, in fact, cause other problems due to a marked decrease in the detectable count-rate. Heller and Goodwin, (1987), suggest acquiring an energy map, using a uniform scatter

medium, as a method to help retain energy uniformity, if this technique is used with patient studies. However, they also note that since the scatter distribution changes with angle, so may the uniformity.

By subtraction (and use of secondary windows)

This method was proposed by Jaszczak et al (1984b). The assumption is that a scatter image reconstructed from events collected in a secondary energy window, at an energy less than the photopeak energy, may be considered to be a reasonable approximation to the scatter component of the image, reconstructed with data collected in the photopeak energy window. In practice, two sets of images are reconstructed and a fraction of the secondary (scatter) image is then subtracted from the photopeak image. Alternatively, a fraction of the projection data obtained using the secondary window, may be subtracted from the projection data obtained using the photopeak window. The process may be summarized by an equation; if

I_{scat} = image reconstructed using the lower energy
window

I_{pp} = image reconstructed using photopeak window
and I_{corr} = compensated image, then

$$I_{corr} = I_{pp} - kI_{scat} \quad (13)$$

where k = a fraction, the value of which has to be determined experimentally for a given system, such that the procedure is optimised for the specific group of source geometries and window settings being used.

In this study (Jaszczak et al, 1984b), the photopeak window was centred at 140 keV, and the window width was such that energies from 127 to 153 keV were included. The secondary window, for collecting scattered events, bracketed energies from 92 to 125 keV. Technetium-99m line source and phantom data were obtained, and it was found that k should be 0.5. Improvements in contrast, even for smaller lesions, and increased sharpness of lesion edges, were also noted. It was found that this type of procedure was easy to implement, although the authors do point out that an optimum value for k must be determined for each system and set of source geometries.

Axelsson et al, (1984), also propose a subtraction technique, but estimate the scatter contribution from the measured data, as a convolution of the measured projection data with an exponential function, the parameters of which are determined experimentally. This scatter distribution is then subtracted from the original projection data, and improved contrast is noted, provided the source is not at the edge or centre of the phantom.

By deconvolution

The technique just referred to, of Axelsson et al, (1984), basically has two stages. These are: a convolution to obtain an estimate of the scatter, followed by a subtraction of the estimate from the acquired projections. A similar technique is proposed by Floyd et al, (1985), except that: (a) scatter is modelled by a convolution of the non-scattered projection data and an exponential function, (b) the parameter values of the exponential function are determined from a Monte Carlo simulation, and (c) the final stage, which is termed a "deconvolution", is performed on the total projections as a modification of the normally used backprojection

filter. Using this method, contrast improvement is reported. However, this algorithm does not reduce interplane scatter - to do this would require a full three-dimensional reconstruction with a two-dimensional deconvolution at each angular projection.

(ii) COMPENSATION FOR ATTENUATION.

By correcting SPECT images for attenuation, it is possible to improve the capability to perform a qualitative comparison, of the distribution of radioisotope in the images. However, image contrast and edge definition are not improved. This is because the attenuation of photons in each projection tends to increase the system noise during the backprojection procedure, while the levels of the lesion and the background are reduced by the same ratio (Heller and Goodwin, 1987). The more fundamental problem is actually scatter of radiation, and ideally this problem must be solved first. Since several of the techniques proposed and tried for scatter compensation have already been discussed, a selection of those used to compensate for attenuation will now be described, followed by some more recent, and more elaborate, techniques proposed to compensate for scatter, attenuation and other factors within the same algorithm.

There are three main categories of attenuation correction algorithm (Gullberg et al, 1983):

(1)Preprocessing correction - projection data are first modified to correct for attenuation, then a reconstruction algorithm is applied.

(2)Intrinsic correction - a specially designed reconstruction algorithm corrects for attenuation.

(3)Postprocessing correction - the image is reconstructed and then each pixel value is modified relative to an average attenuation factor.

Sorenson, (1974), gives a postcorrection approach, applying a hyperbolic sine correction to the geometric mean of opposing projections. Assuming that the administered radioactivity is distributed uniformly in an absorbing medium of constant attenuation μ , and that a measured projection ray travels through a distance L of absorber, along which the element of length fL has a constant source strength, then a corrected projection measurement at angle θ and lateral position x is given by:

$$p_{corr}(x, \theta) = p_{geom}(x, \theta) \cdot \mu l \cdot e^{\mu l / 2} / 2 \sinh(\mu l / 2) \quad (14)$$

where $p_{geom}(x, \theta)$ is the geometric mean of opposing projections. (The geometric mean is the square root of the product of opposing line integral measurements.)

Use of the arithmetic mean (or average) is proposed by Kay and Keys (1975). By this method, the corrected projection is given by:

$$p_{corr}(x, \theta) = 4p_{arith}(x, \theta) / (1 + e^{-\mu l} + 2e^{-\mu l}) \quad (15)$$

Chang (1978) proposes a post-correction method, in which the image is first reconstructed without attenuation correction, and then each pixel is multiplied by the following correction factor:

$$C(x, y) = [1/m \sum_{i=1}^m \exp(-\mu l(x, y, \theta_i))]^{-1} \quad (16)$$

where $l(x, y, \theta_i)$ is the distance from the point (x, y) to the boundary of the attenuating material along the projection ray, at the angle perpendicular to the detector and traversing the point (x, y) .

This correction factor is the inverse of the averaged measured attenuation of a source at the point (x,y) , and may be modified by integrating the distribution along the lines $l(x,y,\theta_i)$, if the true distribution of attenuating material is known.

There are many other iterative methods for performing attenuation correction, and they do produce more accurate results, but with the disadvantage of requiring longer computing times. Iterative methods have the advantage, also, of being able to use an "exact" attenuation distribution (such as may be obtained from a CT scan of the same cross-section), instead of the more generally used ellipsoidal shapes, with an assumed uniform attenuation coefficient inside the ellipse (Moore, 1982).

Bailey et al, (1971), describe a method for performing transmission tomography, using a radionuclide flood source attached to a rotating gamma camera. The studies are performed simultaneously, using different radionuclides for the emission and transmission studies, separation being by pulse height energy discrimination.

The labelled tracer is the higher energy radionuclide (Tc-99m), so the conventional SPECT study is unaffected by scatter. The transmission radionuclide (Gd-153) is in a flood tank fixed to the camera head, so that the patient is always between the uncollimated transmission source and camera head as it rotates. Two sets of images are obtained - the usual emission scan from the upper photopeak window, and the image from the lower energy window containing the transmission scan, degraded by scatter from the administered radiotracer. The scatter image is predicted from the emission scan, using earlier work by the same authors, and subtracted from the degraded lower energy image. It is possible, using this technique, to determine accurately the values of the linear attenuation coefficient, for each voxel within the field of view. The degree of error introduced by using the two radionuclides was not completely assessed, however.

Axelsson et al, (1987), report on a multiplicative algebraic technique to account for both attenuation and scatter. They estimate the scatter contribution, by convolving the measured projection data with a scatter

distribution function, obtained from measurements of line spread functions. The scatter component is then subtracted from the measured projection data, and the result is used as input for the attenuation correction. Attenuation correction is via a two-stage procedure comprising a simple pre-reconstruction correction, AT1, and a more advanced post-reconstruction, AT2; the aim being that the user should be able to choose the less accurate, but faster, pre-reconstruction stage for routine qualitative imaging, and the more time-consuming post-reconstruction stage only in certain special cases. It was found that quantification accuracy and contrast were both improved when AT2 was used, rather than just AT1. However, the best results were obtained when the scattered radiation was treated completely separately, and subtracted before attenuation correction and reconstruction were performed.

Floyd et al, (1986), use an inverse Monte Carlo algorithm, which performs simultaneous compensation for scatter, attenuation and collimator divergence. The algorithm uses physical characteristics of the acquisition apparatus (e.g. energy window setting, system

energy and spatial resolution and radius of rotation), and of the body (e.g. contour and density), to model the system and estimate the source distribution. In this way the necessity for empirical parameters, such as attenuation coefficient and scatter fraction, is eliminated. When compared with filtered backprojection, the inverse Monte Carlo produced results with less noise and better resolution, the most dramatic improvement being in studies with few photon events. This is important since clinical SPECT studies tend to have few counts. The main disadvantage is in the increased computer time necessary to construct an image; using a VAX 11/780 minicomputer, clinical images were produced in twenty five hours, while in current routine clinical SPECT slices can be produced in a matter of seconds. However, preliminary investigations by this group indicated that significant improvements were possible, and that these would help to make inverse Monte Carlo clinically useful as a SPECT reconstruction algorithm.

(f) PURPOSE OF THIS RESEARCH

A number of methods designed to compensate for the effects of scatter and attenuation have been outlined in section I(e). A selection of these will be evaluated, using an Elscint ECT system, in terms of their effect on image quality and their ease of implementation. If possible, a protocol will be developed which produces measurable improvement of image contrast and measured size, within a clinically realistic time-span (of the order of minutes/hours). The correction methods to be tested are as follows.

Scatter correction by using a selection of sizes of symmetric photopeak energy windows, and by using a constant-width energy window positioned asymmetrically at different locations on the photopeak, will be performed. In addition, scatter images, reconstructed using data acquired separately on the Compton peak, will be subtracted from the photopeak images.

Attenuation correction is performed post-reconstruction by using Chang's correction, calculated by the computer with an experimentally determined value of attenuation coefficient. To do this, a method for obtaining, reproducibly, the appropriate attenuation coefficient must be developed.

CHAPTER II EQUIPMENT

(a) THE PHANTOM

The phantom used for this work is shown in Fig.2.1(a). It is cylindrical in shape, 20 cm in length and in diameter, and made from plexiglass; since it is hollow, it may be filled with water containing a quantity of radioisotope. One half of the phantom is empty of internal structure (as shown) and may therefore be used to reconstruct "flood" images. The other half contains plexiglass rods of varying diameter, located at varying distances from the centre of the phantom, as shown in Fig.2.1(b); the plexiglass rods mimic the behaviour of cold lesions in biological tissue. Transaxial slices, reconstructed using data from this section of the phantom, will contain images of these rods or lesions.

During ECT scans, the phantom was supported on a specially constructed trolley, having a system of screws and sliding mechanisms to permit vertical and lateral adjustment. In addition, the trolley made possible reproducibility of the phantom position.

Fig.2.1(a) The phantom - longitudinal view.

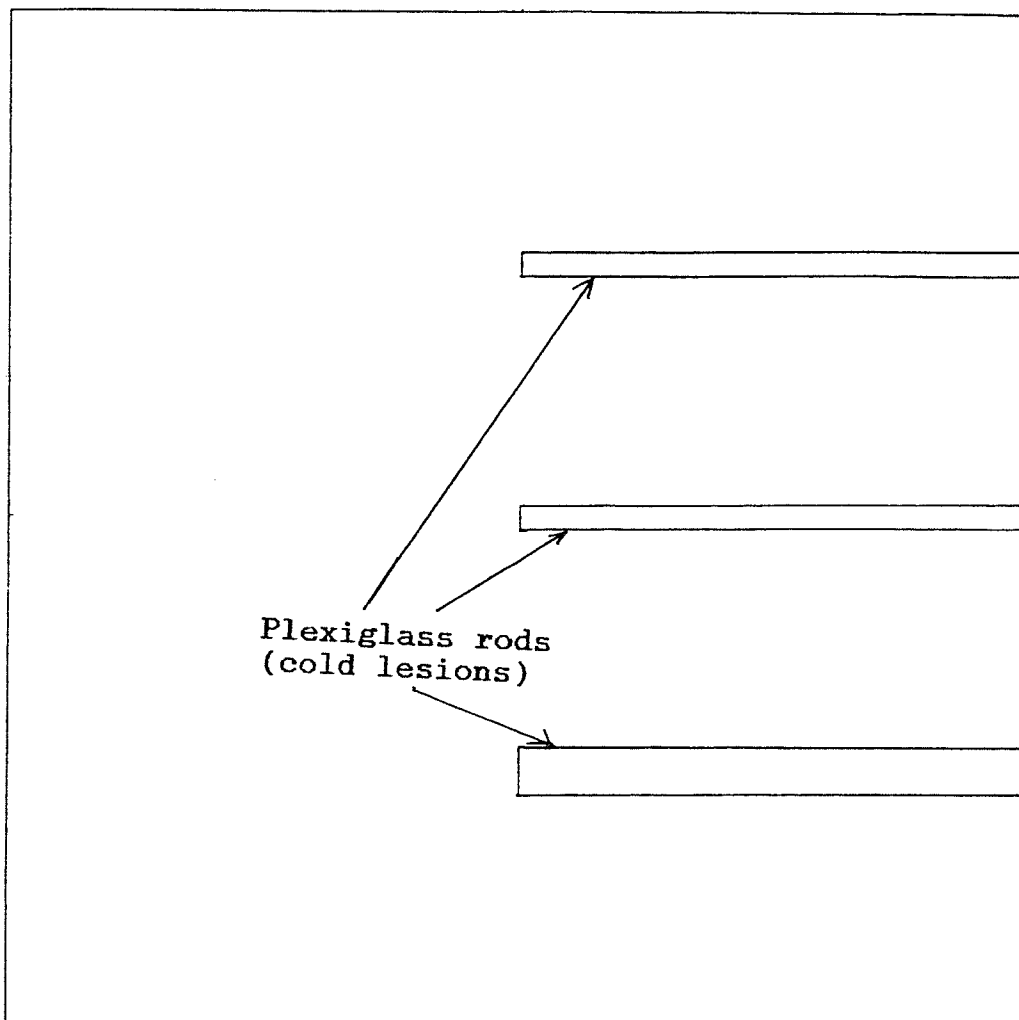
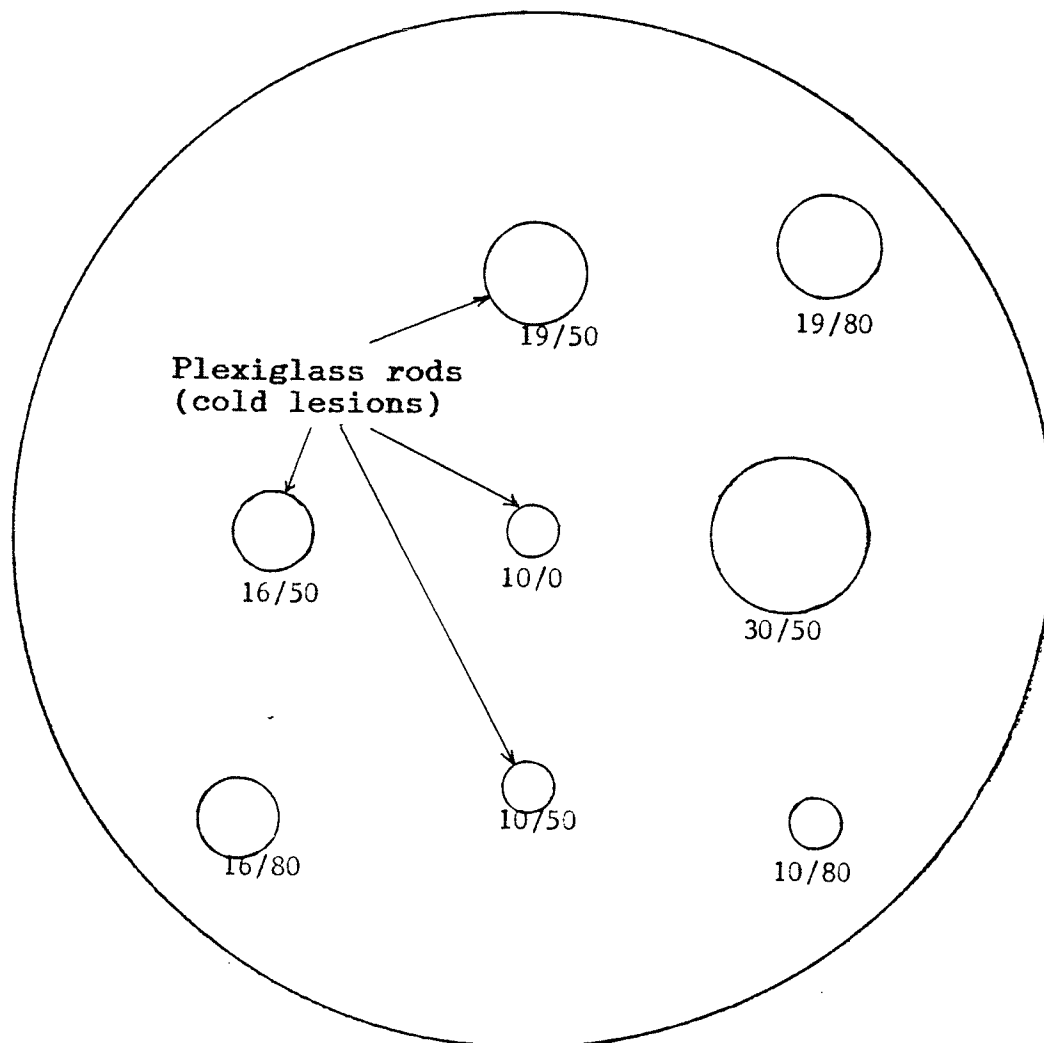


Fig.2.1(b) The phantom - transaxial view, to
illustrate internal structure



Meaning of numbers x/y :

x indicates lesion diameter in mm
 y indicates radial distance of lesion
from centre of phantom in mm

(b) THE RADIOISOTOPE

Before each scan, the phantom was filled with water containing technetium 99m. The principal emission of this radioisotope is a gamma ray having an energy of 140 keV. A more detailed description of Tc-99m is given in section I(b)(i), and will not be repeated here.

(c) THE SYSTEM HARDWARE

The system used in this research is the Elscint ECT. This consists of a large field of view detector head mounted on a rotating gantry, with the keyboard, monitors and data processing and storage system located on a separate operator's console.

The detector field of view is 15.7" and the NaI(Tl) crystal is 3/8" thick. The crystal is viewed by 37 photomultiplier tubes each with a diameter of 3". The gains of the photomultiplier tubes and their associated circuitry are maintained, by a tuning system, at the values which existed when the correction maps (to be discussed later) were obtained. The detector head is free to move in three directions. The rotating gantry is free to rotate clockwise or counter-clockwise; it has an aperture of 600 mm diameter.

The central memory of the computer system stores the correction maps which are needed during acquisition, the software which controls the data acquisition, and the

data acquired. In addition, there is a fixed disk storage, for the correction maps which are not being used, the software required to operate the system, and for acquired images. Data and reconstructed images may also be stored on floppy disks.

(d) OPERATION OF THE SYSTEM**(i) ECT DATA ACQUISITION**

The camera rotates about an axis, generally located on the longitudinal axis of the patient's body, while projections are acquired at specified angles of rotation. Any angular range of rotation from 180 to 360 degrees, and acquisition intervals of 1, 2, 3, 4, 6 and 9 degrees, may be selected. The projections thus acquired produce a series of two-dimensional profiles, which are reconstructed, using the filtered backprojection method, to yield a series of transaxial slices through the scanned object.

(ii) WORD TO BYTE FRAMING

The parameters which characterize the digital image are the matrix size and the mode (byte or word). The matrix size defines the number and the size of the pixels in the image, and therefore the degree of spatial detail which can be displayed. In nuclear medicine generally,

matrix sizes range from 32 x 32 to 512 x 512 pixels. In the Elscint ECT system, matrix sizes of 64 x 64 and 128 x 128 are available. "Byte" and "word" mode are terms which refer to the pixel depth, that is, the maximum number of events which may be recorded by each pixel. A pixel depth of 8 bits can store $2^8 = 256$ events, in which case counts in the range from 0 to 255 can be stored, and any additional events will be disregarded. A pixel depth of 16 bits can store $2^{16} = 65536$ pieces of information, in which case counts in the range from 0 to 65535 can be stored. Byte mode makes available, to each pixel, 8 bits of memory, while word mode makes available 16 bits of memory.

After acquisition of a study in word mode, the data is normalized to a highest pixel value of 220, with the remainder of the study in proportion (word to byte framing). The value of 220 allows space for subsequent corrections for sensitivity and variations in the rotational motor speed.

(iii) ECT DATA NORMALIZATION AND SENSITIVITY CORRECTION

The software includes a function which calculates the physiological half-life time (in minutes) of the isotope. After corrections for angular velocity and isotope decay, the number of counts in the first and last frames will be the same. This process is called normalization.

As mentioned in section I(c), even very small non-uniformities in the collimator will, after ECT reconstruction, give rise to ring artifacts. It is therefore necessary, to perform sensitivity correction, on all acquired data before reconstruction. A flood (or sensitivity map) is acquired with the same acquisition parameters as those used for ECT data, and is applied during the normalization procedure.

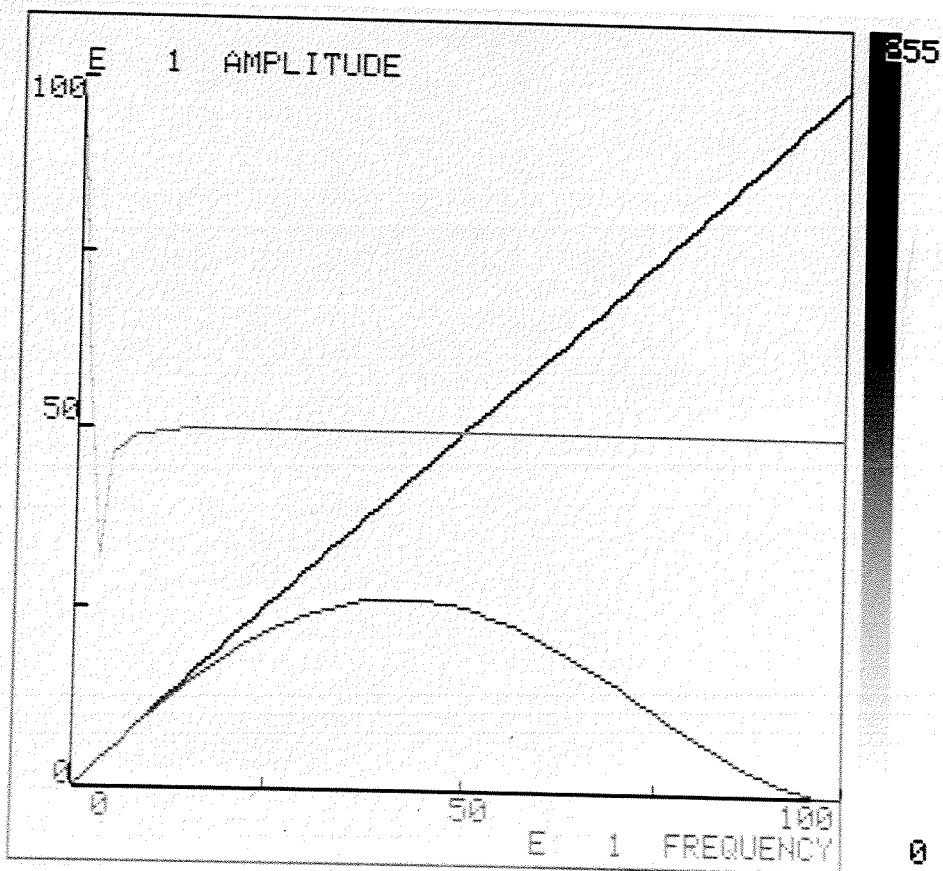
(iv) ECT RECONSTRUCTION

Reconstruction is by the filtered backprojection method and so a filter must be selected. Eight different filters are available in the software of the system being used, as follows: Hanning, Butterworth, Ramp, Metz,

Wiener, Shepp-Logan, Hamming and Parzen. Details of these filters are to be found in texts such as those by Pratt (1978), Blinchikoff and Zverev (1976), and Childers and Durling (1975), articles such as that by Budinger et al (1979), and also in the papers by Shepp and Logan (1974), and Metz and Beck (1973). The Hamming, Parzen, Shepp-Logan and Ramp are defined, and may not be modified. However, the Hanning and Butterworth filters may be altered if this is required.

Fig.2.2 shows the characteristics of the Hanning normal filter. A ramp filter is shown for comparison, as it is the ideal to be used with an infinite number of views, each having perfect data. In reality, we require a filter which rolls off at high frequencies, and this is shown in the second graph. The third graph is the Fourier transform of the filter.

Fig.2.2 Characteristics of Hanning normal and Ramp filters.



CHAPTER III METHOD

(a) ACQUISITION INFORMATION

The phantom described earlier, containing water and 350 to 400 MBq of Tc-99m was supported on the trolley and levelled. It was positioned so that the axis of the phantom was along the axis of rotation of the camera. The camera head and gantry were positioned so as to give a radius of orbit of 12.5 +/- 0.5 cm. This is the smallest possible radius of orbit the camera can attain, without touching any part of the phantom or its supporting trolley. In all cases 360 degree, continuous, circular scans were performed, with data acquired over 2 degree intervals. The frame size was 64 x 64 and word mode was employed.

In the first series of experiments, the PHA window was centred on the 140 keV photopeak, but the window width was increased symmetrically about the 140 keV position. The window sizes used were 5-5%, 8-8%, 10-10%, 12-12% and 15-15%, with respect to the 140 keV mid-window position.

In the second series of experiments, the total window width was maintained at 12%, but the window was moved through a series of positions across the 140 keV photopeak. The window positions used were 10-2%, 8-4%, 6-6%, 4-8% and 2-10%.

In the third series of experiments, an energy window on the Compton scatter peak was used, in addition to the photopeak window. A 10-10% window centred on the 90 keV peak was used to acquire projections consisting of scattered radiation, which were later used to reconstruct images. Photopeak images were acquired using 10-10%, 8-4% and 6-6% windows respectively. It was necessary to obtain the scatter images prior to the photopeak images, because the acquisition software available was incapable of carrying out simultaneous acquisition over 2 degree intervals and in word mode (although this was possible for other combinations of acquisition interval and mode type).

(b) SENSITIVITY MAPS

The sensitivity map used to correct the acquired photopeak data was that currently in use for clinical imaging. This map was acquired at a photopeak energy of 140 keV, with the PHA window at 10-10%. The assumption is that the sensitivity map provides adequate correction for the acquired data. Since acquisition of calibration images for a number of different energies is clinically impractical, and since artifacts are not observed in the reconstructed flood images, this assumption was considered to be valid.

A new energy sensitivity map was acquired for the Compton peak, centred at 90 keV (a value chosen by inspection of the spectrum obtained using a Tc-99m source placed under the camera head) with 10-10% windows.

(c) ECT RECONSTRUCTION

For all window sizes and positions the reconstruction process was similar. The normalized data was used for the reconstruction, as this has been corrected for irregularities in the camera motion. For backprojection, the commonly used Hanning normal filter was selected. The thickness of the reconstructed slices is user-selectable. Two slices, each 14 pixels deep, were reconstructed, as shown in Fig.3.1. The first slice is a flood image, while the second slice contains images of the plexiglass rods (representing cold lesions). The radius of the reconstructed slices was chosen to be 16 pixels, giving a zoom, or magnification, factor of 2. A typical set of reconstructed slices is shown in Fig.3.2.

Fig.3.1 Images of the phantom: 2 slices, each
14 pixels deep.

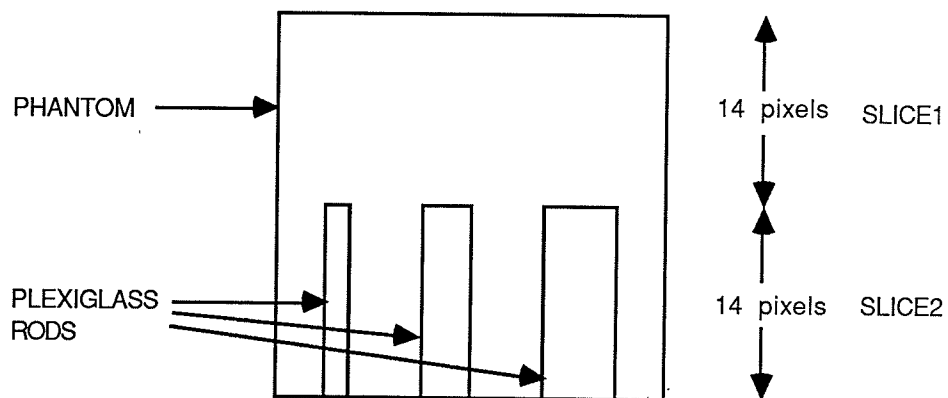
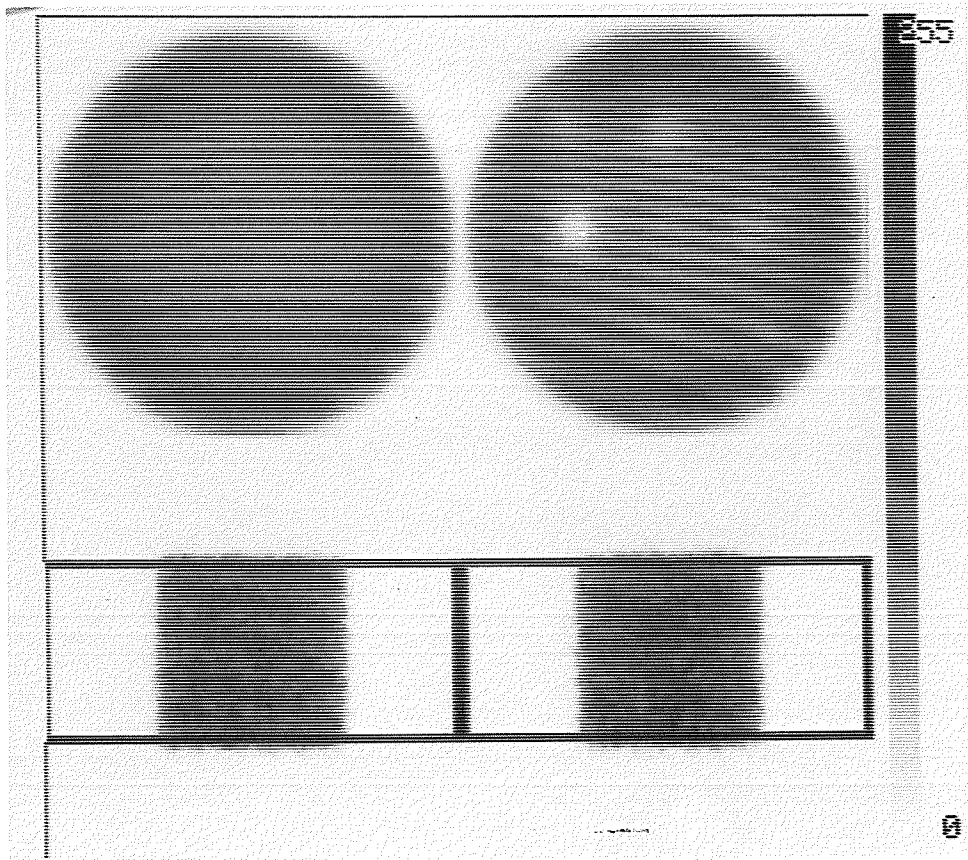


Fig.3.2 A set of reconstructed slices.

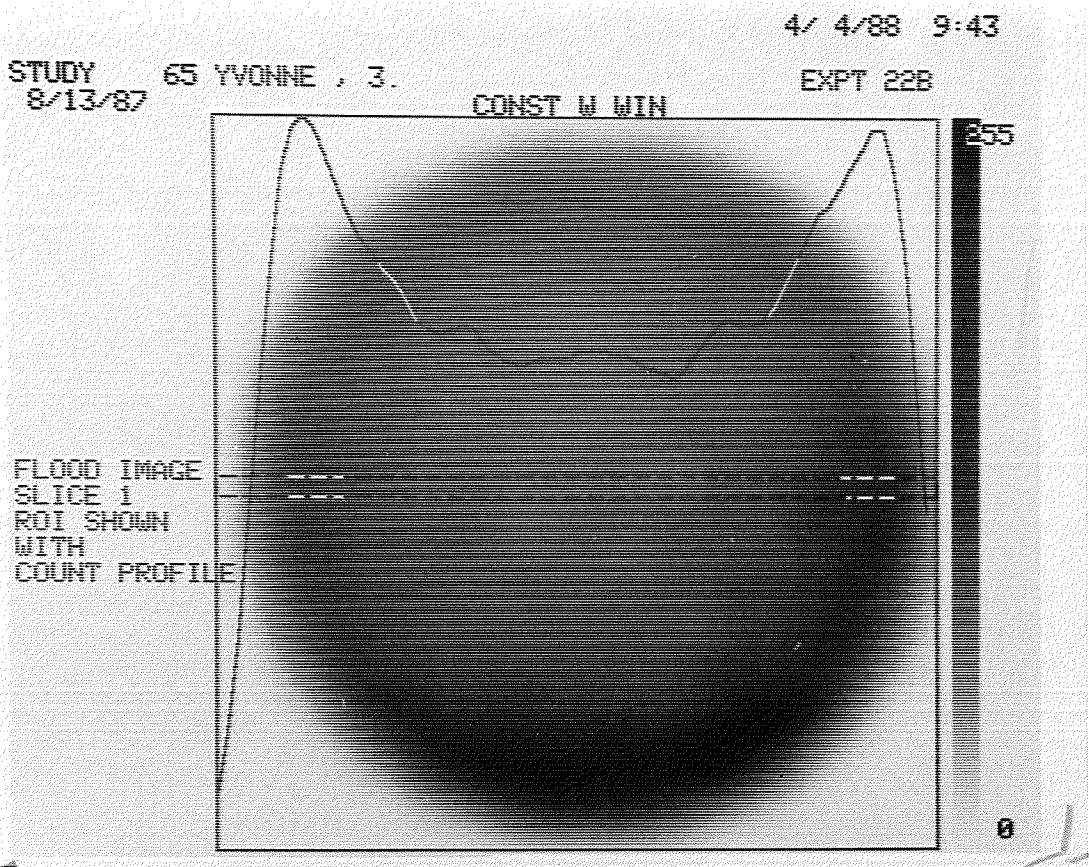


(d) VALUE OF THE ATTENUATION COEFFICIENT

Recall that for each data acquisition 2 slices, 14 pixels deep were reconstructed, and, of these, the first was a flood image, as shown in Fig.3.2. This slice was selected and zoomed by a factor of 8 to fill the screen. A rectangular region of interest, 2 pixels deep and 64 pixels wide, was constructed across the mid-section of the slice, and became the basis for a profile of counts versus lateral distance, in this volume element of the slice. Fig.3.3 shows such a slice, with the region of interest and profile as described.

The software in the Apex system calculates the Chang correction factor (Chang, 1978), given in equation 16, with the value of attenuation coefficient selected by the user, and applies it to every pixel in the image. The corrected images may be replayed on the screen, where the region of interest mentioned above may again be used as the basis of a count profile.

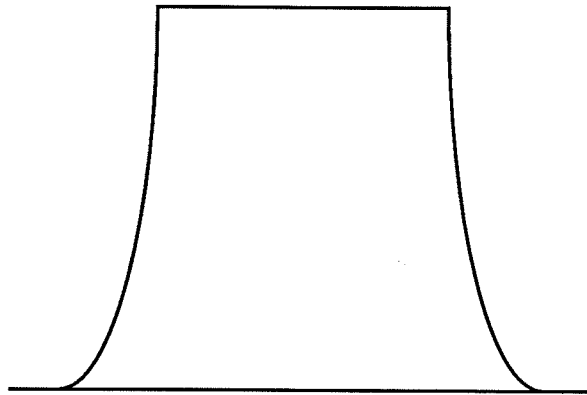
Fig.3.3 Flood slice with count profile.



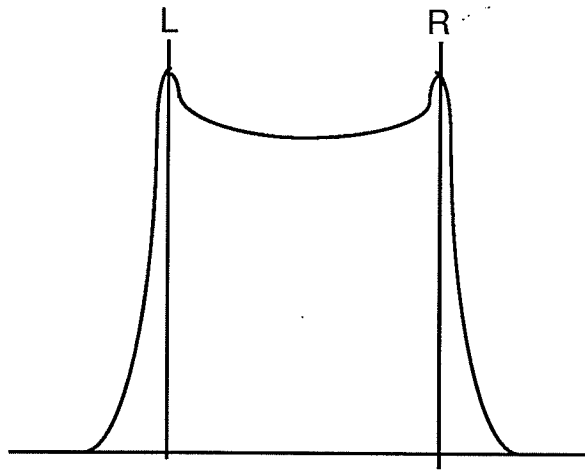
Consider why this profile is informative. In the absence of attenuation of the gamma rays, such a profile should have the flat-topped appearance shown in Fig.3.4(a). In practise, the gamma rays suffer attenuation, causing the profile to assume an appearance similar to that shown in Fig.3.4(b). By applying the appropriate Chang correction factor (calculated using the "best" value of the attenuation coefficient) it should be possible, in theory, to compensate for the effect of the attenuation of the gamma rays, so that the profile under discussion more closely resembles Fig.3.4(a).

The problem, then, was to identify the "best" value of the attenuation coefficient. A possible solution was simply to try a series of numbers, drawing the relevant profiles and assessing by eye when the profile became flat-topped. However, this was a crude approach and was open to many errors, since it was difficult to assess which of a series of very similar, and noisy, profiles best approximated to flatness.

Fig.3.4 Idealized count profiles,
to show the effect of attenuation.



(a) FLAT-TOPPED PROFILE



(b) U-SHAPED PROFILE

Consider the shape of the profile of Fig.3.4(b) between the markers L and R, as indicated. In this region, the profile was assumed to approximate to a parabola, described by an equation of the form $ax^2 + bx + c$. Therefore, by applying a polynomial fit to points between appropriately chosen markers, such as those illustrated, the value of the coefficient 'a' may be used as an indicator of the flatness of the profile. The attenuation coefficient which results in the value of 'a' being equal to zero may be assumed to be the "best" value. In fact, to be strictly rigorous we require both 'a' and 'b' to be zero; however, since coefficient 'a' has the stronger influence, and since priority is given to developing a method which is convenient to use on a day-to-day basis, the requirement on 'b' was relaxed.

Now, in general, it was not found that any one value of selected attenuation coefficient resulted in 'a' being exactly zero. In general, it was only possible to obtain a series of values of 'a' which, although very close to zero, moved from being slightly negative to being slightly positive. However, a plot of 'a' against attenuation coefficient reveals a linear relationship, as

shown in Fig.3.5(a). Therefore, a linear least-squares fit may be employed to obtain the slope and intercept, and hence the value of attenuation coefficient corresponding to 'a' = 0 (that is, the point of intercept on the x axis).

Practically, this was a convenient process to accomplish using the Apex system. After reconstruction of the image slices, a set of, say, five corresponding values of attenuation coefficient and coefficient 'a' are required. A protocol for this purpose was created by linking the appropriate commands together, and was assigned to a key. The system also has the capability to perform the linear fit; it was used to plot 'a' against attenuation coefficient and perform the least-squares fit shown in Fig.3.5(b). A possible improvement to this method would be to upgrade the protocol described to require less user intervention, thereby reducing the time required to produce the appropriate attenuation coefficients. At present, it requires approximately seven minutes to obtain a useful set of five 'a' values, and the corresponding attenuation coefficients, followed by a further few minutes to perform the least-squares fit, and

calculate the final value of the attenuation coefficient. The least-squares fits performed on the Apex system were double-checked using an Amdahl computer system, which also gave the error values on each fit, making it possible to calculate an error on the final value of attenuation coefficient obtained. These calculated error values are reported, with the appropriate attenuation coefficients in Tables 4.1, 4.2 and 4.3.

Fig.3.5 Coefficient 'a' plotted against attenuation coefficient.

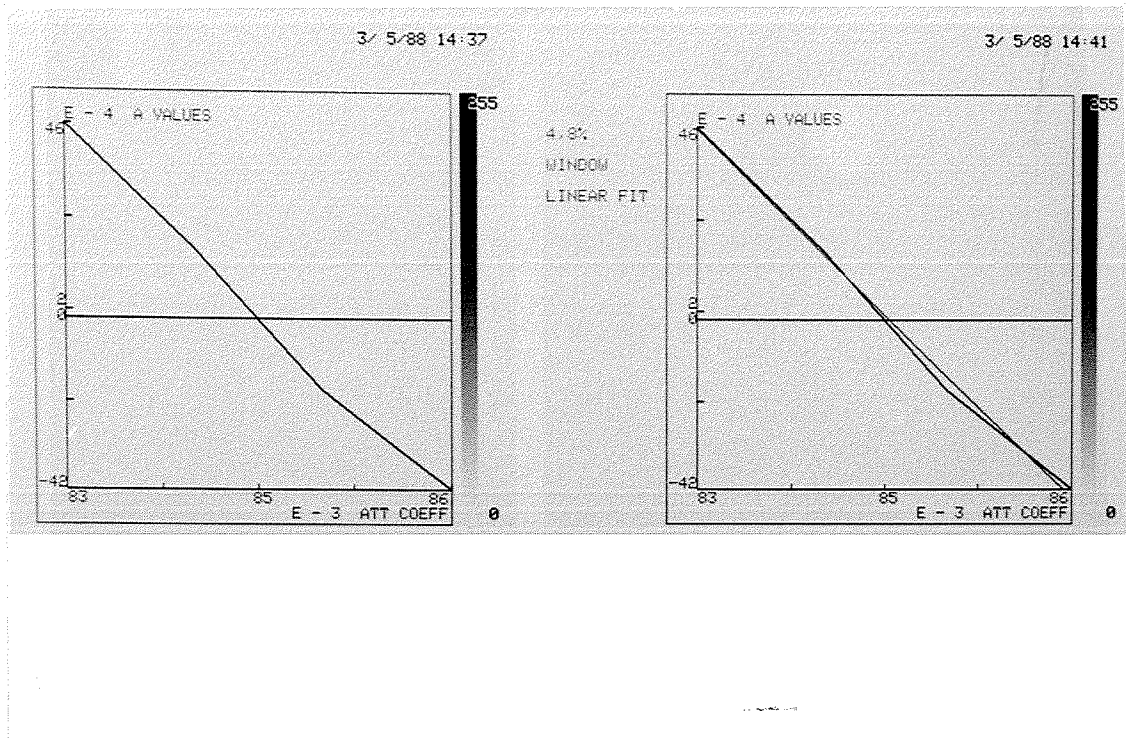


Fig 3.5(a)

Fig 3.5(b)

(e) SUBTRACTION

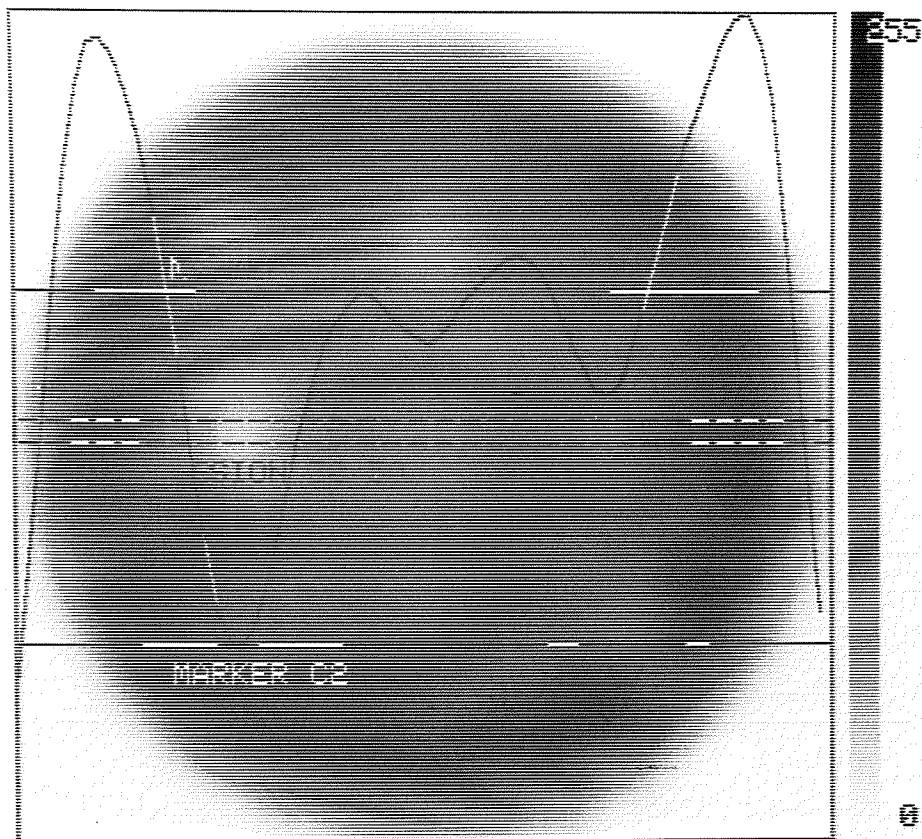
The data obtained in the third series of scans, as described in section III(a), was reconstructed, and attenuation coefficients were obtained using the flood images as described. The attenuation coefficients were then applied to the images of the lesions (plexiglass rods). The corrected images were then subtracted. The system software provides the facility to subtract a user-selectable fraction of one specified image from another specified image. Thus, fractions of the scatter image, from 0.0 to 0.9 were subtracted from each of the 10-10%, 8-4% and 6-6% photopeak images in turn. The resulting images were analysed for contrast and resolution as described below.

(f) LESION SIZE AND CONTRAST

The second slice of the reconstructed images, in each case, was selected and zoomed by a factor of 8 to fill the screen. It will be recalled that this slice contains the lesion images, while slice one contains the flood image. A rectangular region of interest, 2 pixels deep and 64 pixels wide, was positioned across the lesions under study and used to draw a profile across the slice. A horizontal marker was used to locate the trough and peak corresponding to the lesion under study. If C_1 and C_2 correspond to the peak and trough respectively, then the contrast of the lesion image is given by $(C_1 - C_2) / (C_1 + C_2)$. This is illustrated by the example in Fig.3.6, which shows how the contrast of the lesion at the extreme left of the region of interest is obtained (identified as lesion 30/50 throughout this document).

The position of C_1 was selected always as the lowest of the two peaks on either side of the trough, since this indicated the background against which it was most difficult to identify the lesion.

Fig.3.6 To show how the contrast values were obtained.



Next, a horizontal marker was positioned at half-height (that is, at $(C_1 + C_2)/2$). A vertical marker was used to locate the intersections of the horizontal marker with the profile. The difference in these numbers gave the FWHM of the peak in pixels. Using the scale factor, which is automatically recorded with the study (0.3440 cm/pixel in this case), the FWHM in cm may be calculated.

This procedure was performed on the lesion images, before and after attenuation correction, for each window size, or after subtraction of the scatter images. In this way, the effect of the various methods of scatter and attenuation correction on contrast and resolution, and therefore on lesion detectability and measurement of size, was assessed. Results are presented for selected lesions as given in Table 3.1. Individual lesions are denoted by a symbol of the form x/y , where x represents the diameter of the lesion in millimetres, and y represents the distance of the lesion from the centre of the phantom, also in millimetres.

TABLE 3.1 LESIONS FOR WHICH RESULTS ARE QUOTED

NOMENCLATURE	DIAMETER	DISTANCE FROM CENTRE
lesion 19/80	19 mm	80 mm
lesion 30/50	30 mm	50 mm
lesion 16/50	16 mm	50 mm

(g) ASSESSMENT OF ERRORS IN CONTRAST AND LESION SIZE
MEASUREMENT

From count profiles through the lesion images, the contrast and FWHM were determined. For a profile having a maximum value of C_1 and a minimum value of C_2 , the contrast was given by $(C_1 - C_2)/(C_1 + C_2)$. The uncertainty in determining both C_1 and C_2 was ± 0.250 pixels, therefore the uncertainty in the quantities $(C_1 - C_2)$ and $(C_1 + C_2)$ was ± 0.500 pixels. The fractional error in the contrast was then $C_1/(C_1^2 - C_2^2)$. The uncertainty in establishing the FWHM of an individual profile was estimated to be ± 0.500 pixels.

CHAPTER IV RESULTS AND DISCUSSION

(a) ATTENUATION COEFFICIENTS

Tables 4.1 and 4.2 show the values of attenuation coefficient obtained, as described, for the various symmetric and asymmetric windows respectively. Noticeable in Table 4.1 are the error limits on the values obtained for the 8-8% and 10-10% values, which are large enough to include all the other values. In Table 4.2, a decreasing trend is exhibited, as expected.

As the constant width window is moved towards higher energies, the average photon energy included increases, and this may be expected to lead to a decrease in attenuation coefficient. The same is not true of the symmetric windows listed in Table 4.1 - as the width of the window increases the average energy included will not alter significantly, because the numbers of both low and high energy photons, included by the window, will be increased. Therefore, an overall decrease in attenuation coefficient is not anticipated, and, within the quoted limits of uncertainty, is not observed.

Table 4.3 shows the attenuation coefficients obtained for the windows specified, using the same method as was used to obtain the values listed in Tables 4.1 and 4.2. Completely new data was acquired and analysed to obtain these results. Comparison of these values with the attenuation coefficients for the 10-10%, 8-4% and 6-6% windows in Tables 4.1 and 4.2 reveals agreement within the limits of experimental error, which confirms the reproducibility of these numbers.

The same method was employed to obtain the attenuation coefficient for the 10-10% window positioned on the Compton peak. The values indicated in Table 4.3 are those which are used to apply attenuation correction to the corresponding images before subtraction, as described in the previous chapter.

TABLE 4.1: ATTENUATION COEFFICIENTS FOR SYMMETRIC WINDOWS

WINDOW SIZE	ATTENUATION COEFFICIENT
5-5%	0.097 +/- 0.006
8-8%	0.094 +/- 0.020
10-10%	0.095 +/- 0.026
12-12%	0.089 +/- 0.005
15-15%	0.089 +/- 0.009

TABLE 4.2: ATTENUATION COEFFICIENTS FOR ASYMMETRIC WINDOWS

WINDOW SIZE	ATTENUATION COEFFICIENT
10-2%	0.108 +/- 0.007
8-4%	0.105 +/- 0.009
6-6%	0.098 +/- 0.005
4-8%	0.085 +/- 0.007
2-10%	0.074 +/- 0.005

TABLE 4.3: ATTENUATION COEFFICIENTS FOR WINDOWS USED FOR SUBTRACTION

WINDOW SIZE (OR POSITION)	ATTENUATION COEFFICIENT
10-10%	0.096 +/- 0.010
8-4%	0.104 +/- 0.017
6-6%	0.095 +/- 0.011
10-10% on Compton peak	0.042 +/- 0.003

(b) LESION CONTRAST AND SIZE MEASUREMENTS

Results are presented for three lesions, as listed in Table 3.1. Before proceeding, it may be helpful to recall that the lesion nomenclature, x/y , indicates the diameter of the lesion, (x), and the distance of the centre of the lesion from the centre of the phantom, (y), both quantities stated in millimetres. In the graphs which follow, error bars have been included on all data points. However, in many cases, the magnitude of the measurement error is such that the bars do not appear to be present.

Fig.4.1 shows the variation in contrast of the three selected lesions, as the width of the symmetric window is increased, without attenuation correction being applied, while Fig.4.2 shows the variation in contrast as the position of the constant width, asymmetric window is moved towards higher energies. Figs.4.3 and 4.4 show the same data as Figs.4.1 and 4.2, after the appropriate attenuation correction (as listed in Tables 4.1 and 4.2) has been applied to the images.

In Fig.4.1, the contrast exhibits a decreasing trend, as the window width is increased to include a wider range of energies. The degradation in contrast, may be attributed to the inclusion of an increasing proportion of scattered photons, as the window width increases.

In Fig.4.2, there is an overall increasing trend as the window position moves towards higher energies, which may be attributed to the exclusion of scattered photons. In both Figs.4.1 and 4.2 the trends described are most clearly demonstrated by the results for lesion 30/50.

Comparison of Fig.4.3 with Fig.4.1 and of Fig.4.4 with Fig.4.2 shows that attenuation correction does not radically alter the general trends exhibited. However, it does have a marked effect on the relative contrast of lesions 19/80 and 16/50, in that the plots, which were previously separated, now overlap. The contrast of lesion 19/80 is reduced, while that of 16/50 is increased, with the result that for virtually all window sizes the values are almost the same.

Fig.4.1 Contrast of three lesions, without attenuation correction, plotted against (symmetric) window size.

Fig.4.2 Contrast of three lesions, without attenuation correction, plotted against (asymmetric) window size.

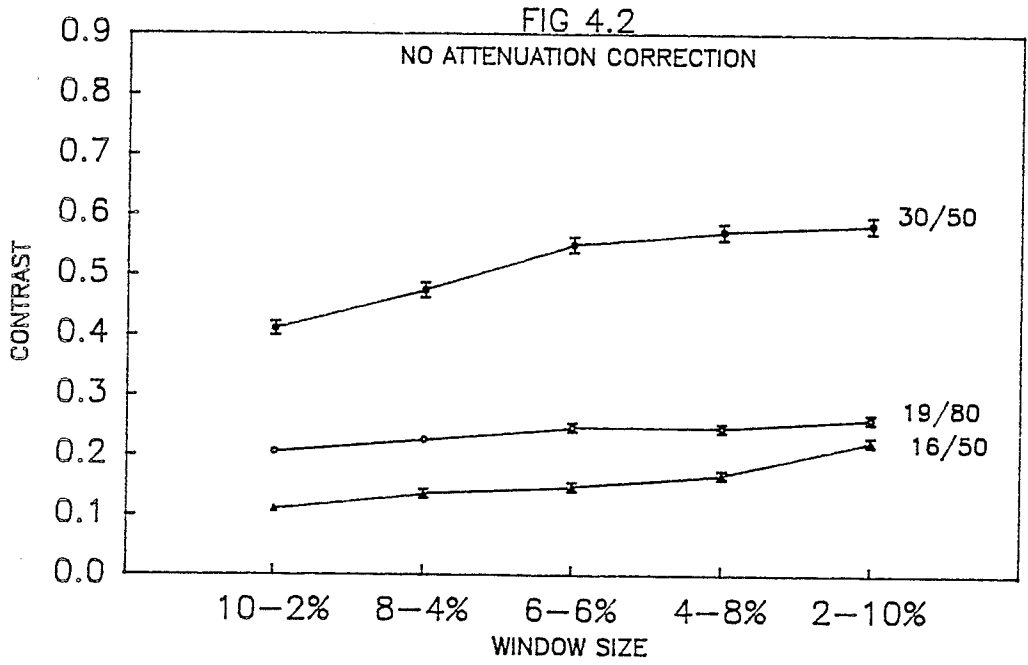
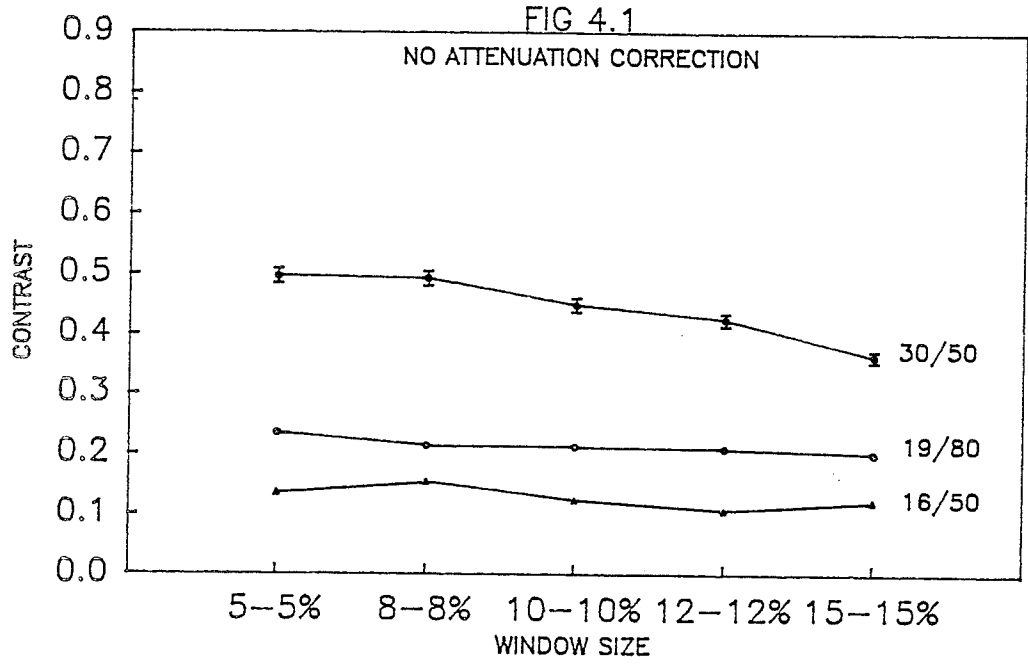
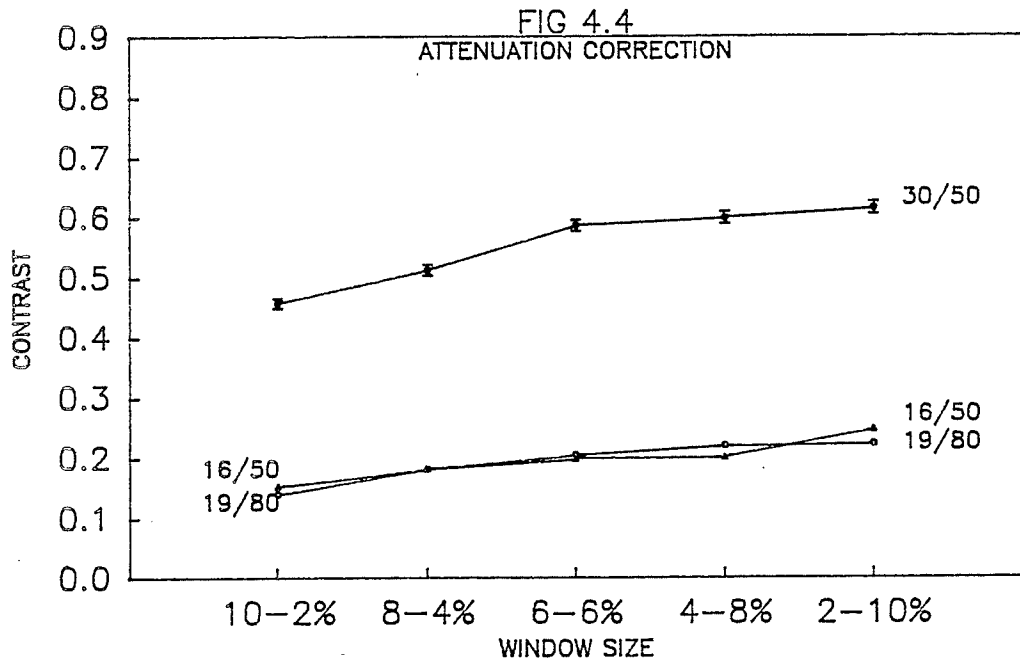
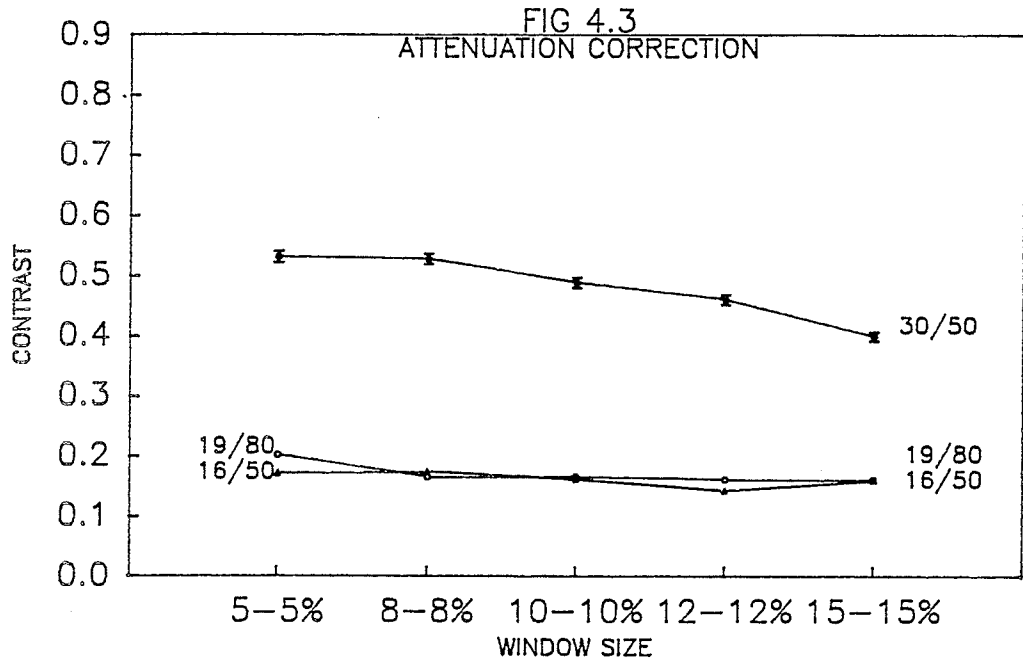


Fig.4.3 Contrast of three lesions, after attenuation correction, plotted against (symmetric) window size.

Fig.4.4 Contrast of three lesions, after attenuation correction, plotted against (asymmetric) window size.



(c) SYMMETRIC WINDOWS

Figs.4.5 to 4.7 illustrate the effect of attenuation correction, on the contrast and resolution of each lesion, when symmetric windows of increasing width are used to acquire the data.

Figs.4.5(a) and 4.5(b) refer to lesion 19/80. Of the three lesions reported, it is closest to the surface of the phantom. Application of attenuation correction decreases the contrast at all window sizes, although the overall shape of the graph is not altered. The highest contrast is achieved with a 5-5% window and no attenuation correction. The measured size of the image of the lesion is decreased at all window sizes, after attenuation correction. The actual size of the lesion (equivalent to 5.52 pixels, as indicated on the figure) is included within the error bars of the measurements of size of the uncorrected image, at all window sizes, without attenuation correction.

Figs.4.6(a) and 4.6(b) refer to lesion 30/50. Application of attenuation correction causes a small increase in contrast (for example, from 0.492 to 0.527), and also increases the measured size of the lesion at all window sizes. As indicated, the actual size of the lesion is 8.72 pixels. Without attenuation correction, this is encompassed only by the measurement performed on the image obtained using an 8-8% window. After attenuation correction, the actual size is included within the error limits of the measured size, for all window widths, except the 8-8% window.

It is interesting to note the results obtained with the 10-10% window. With or without attenuation correction, the contrast is less than obtained with the 5-5% or 8-8% windows, although probably this is not a major disadvantage with respect to this already relatively high contrast lesion. However, if accurate measurements of the lesion size are required, Fig.4.6(b) indicates that there will be a substantial underestimate without attenuation correction (7.875 +/- 0.005 pixels as compared with an actual size of 8.72 pixels).

Figs.4.7(a) and 4.7(b) refer to lesion 16/50, which is relatively difficult to detect, due to its depth within the phantom and its smaller size. The 5-5% and 8-8% windows give the best contrast values, but with or without attenuation correction (which has very little effect on the contrast), these are never more than 0.180. The corresponding measurements of the diameter of the lesion are a considerable overestimate of the actual size (4.65 pixels, as indicated on the figure), for all window sizes, with or without attenuation correction. There does, however, appear to be a decreasing trend in the measurements of size, as the window width is increased.

The observation that, in general, optimal results were obtained with the narrower windows, influenced the selection of the window width to be used to investigate the effect of a constant width window, at various positions on the photopeak. As a compromise between exclusion of scattered photons, and inclusion of sufficient numbers of primary photons, an overall window width of 12%, positioned at 10-2%, 8-4%, 6-6%, 4-8% and 2-10%, was selected for the asymmetric window measurements discussed below.

Fig.4.5 Contrast and resolution of lesion 19/80, with and without attenuation correction, plotted against (symmetric) window size.

167
FIG 4.5(a)

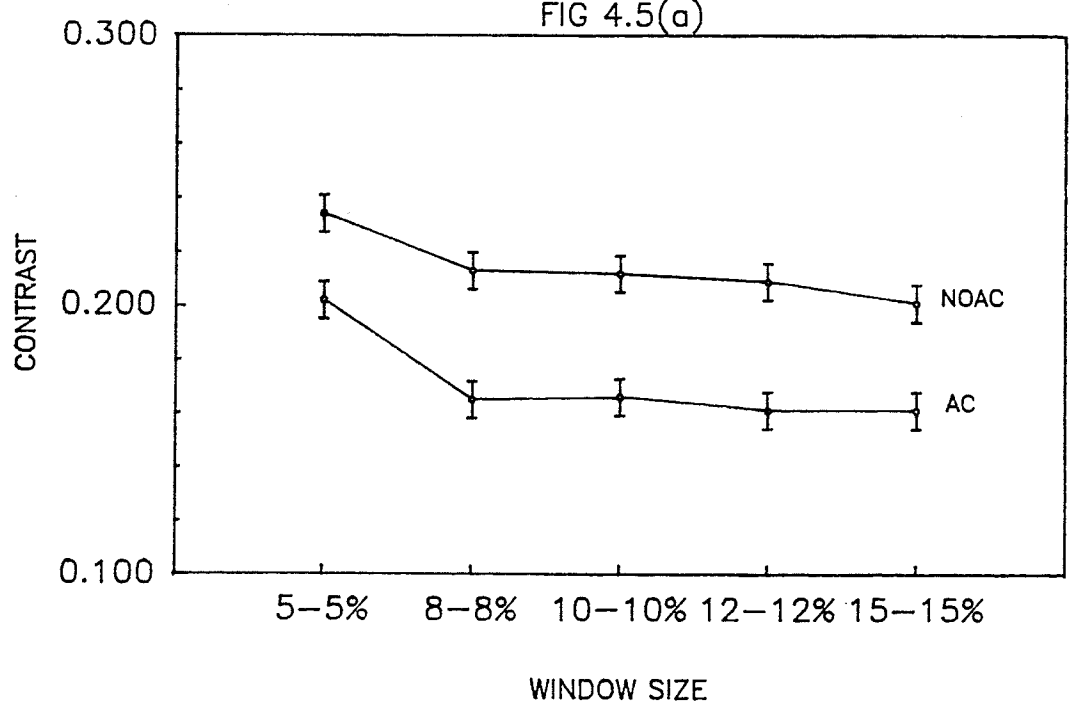


FIG 4.5(b)

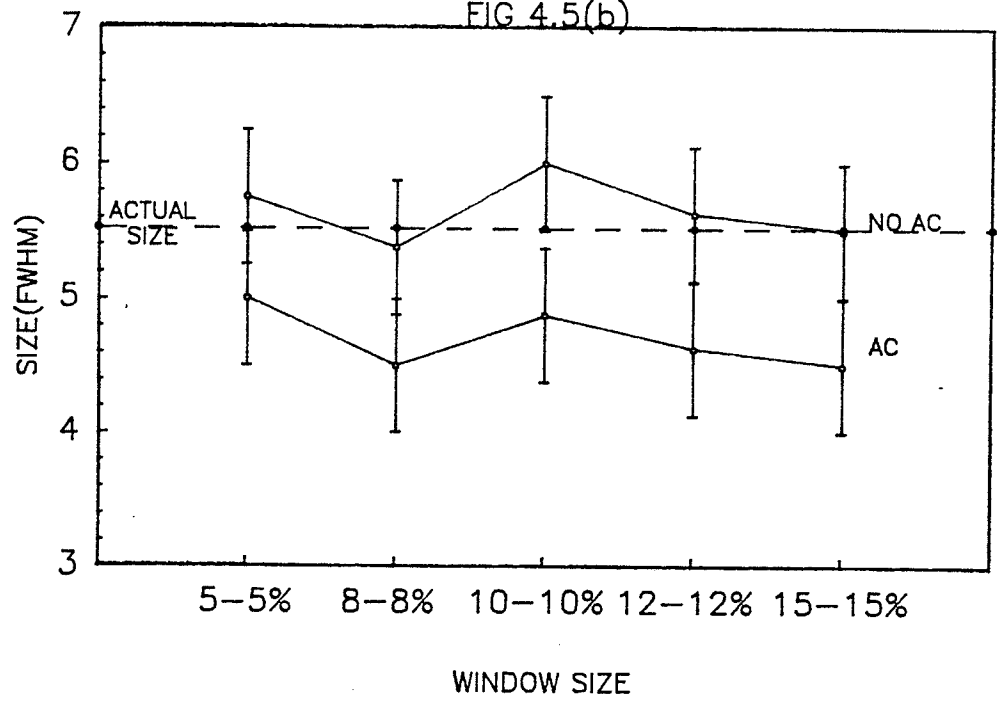


Fig.4.6 Contrast and resolution of lesion 30/50, with and without attenuation correction, plotted against (symmetric) window size.

FIG 4.6(a)

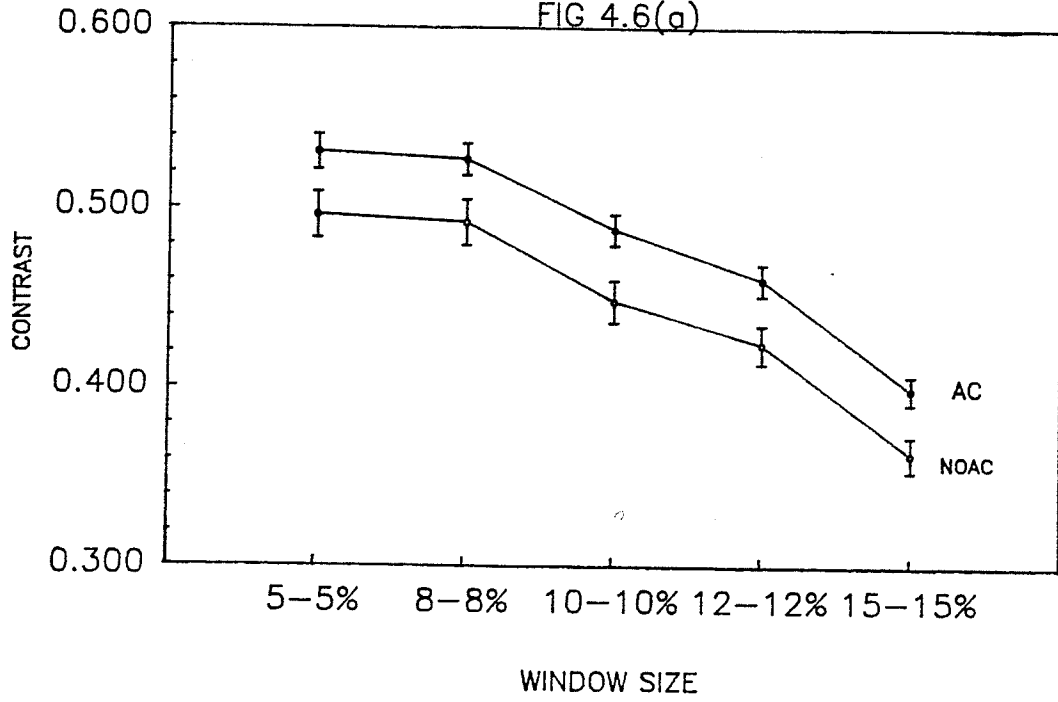


FIG 4.6(b)

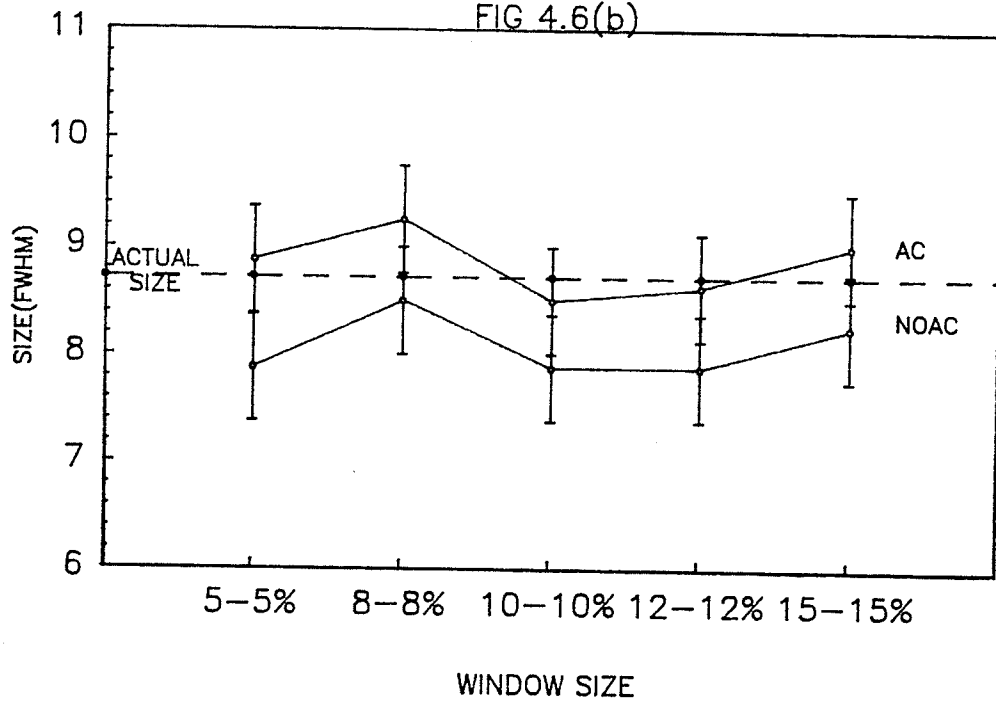


Fig.4.7 Contrast and resolution of lesion 16/50, with and without attenuation correction, plotted against (symmetric) window size.

FIG 4.7(a)

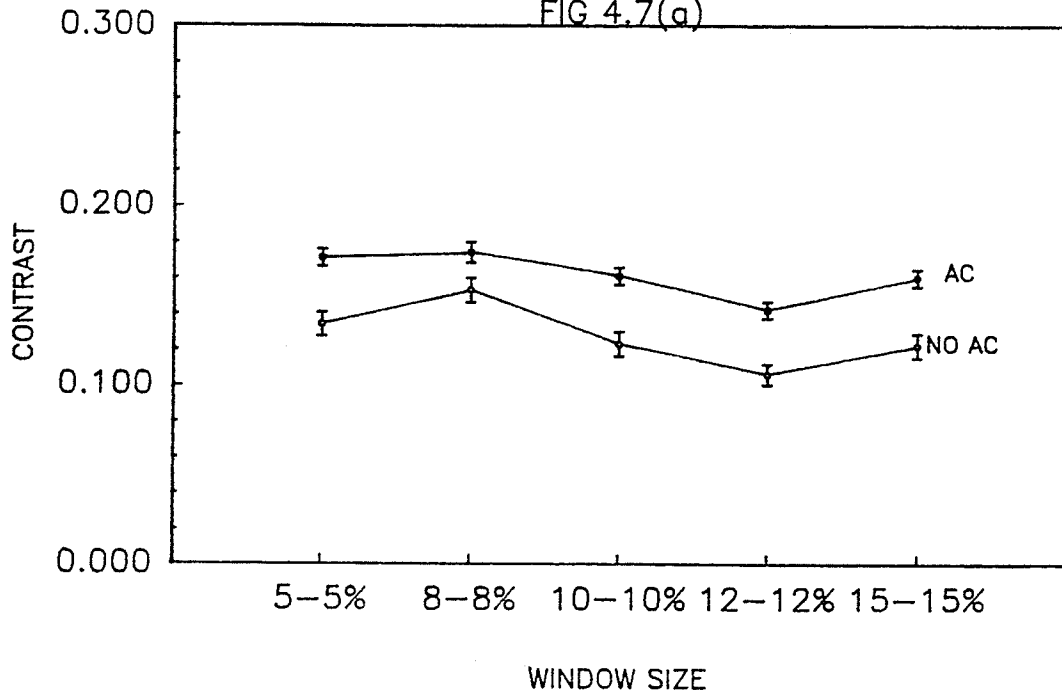
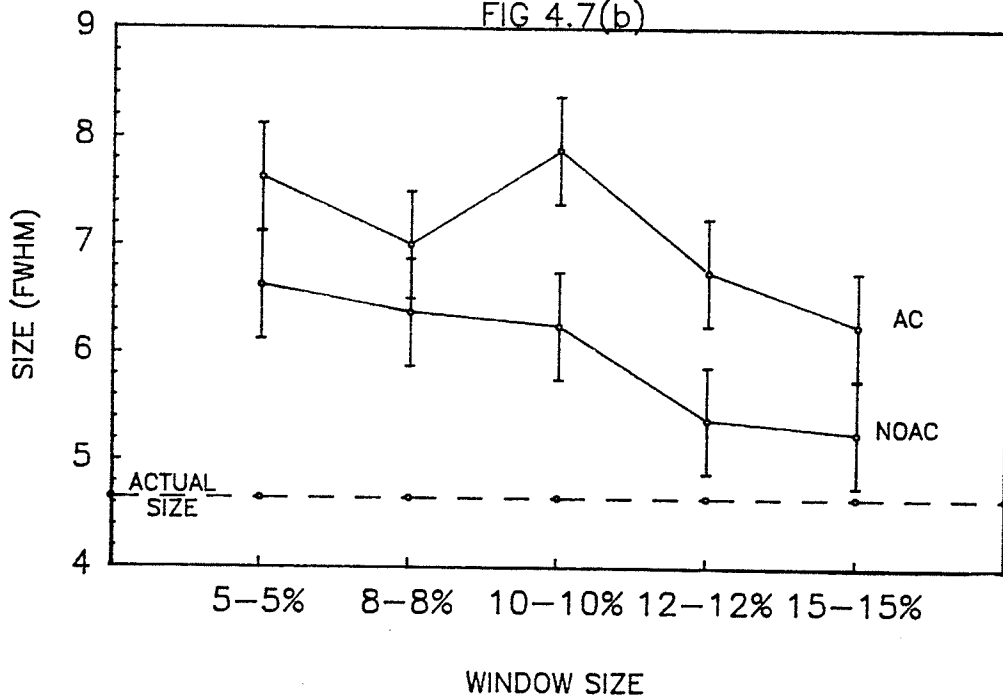


FIG 4.7(b)



(d) ASYMMETRIC WINDOWS

Figs.4.8 to 4.10 illustrate the effect of attenuation correction on the contrast and resolution of each lesion, as a window of constant width is located at various positions, moving towards higher energy, on the photopeak.

Figs.4.8(a) and 4.8(b) refer to lesion 19/80. Application of attenuation correction decreases the contrast at all window positions, and also tends to decrease the measured diameter of the lesion, although the error bars overlap at all windows except 10-2%. The actual size of the lesion lies within the error limits of the measured size, at all window positions, for images obtained without attenuation correction. This is true only for the 4-8% window, with attenuation correction. It must then be concluded that for lesion 19/80, optimal image contrast and resolution are achieved by using a 6-6% or 4-8% acquisition window, without applying attenuation correction. This confirms the indication of Figs.4.5(a) and 4.5(b), that a narrow window, without

attenuation correction, is best for detection and measurement of this lesion.

Figs.4.9(a) and 4.9(b) refer to lesion 30/50. At all window positions, the contrast is greater than even the highest values, for either lesion 19/80 or 16/50, and increases as the window is moved to higher energies. The deciding factor perhaps should be the resolution, which is improved by use of attenuation correction. Without attenuation correction, the actual size (8.72 pixels) is included within the error limits of only the 2-10% window position measurement. When attenuation correction is applied, the actual size is encompassed by the error limits on the diameter measurements, at all window positions except 10-2%. The best combination of contrast and resolution is achieved by using the 4-8% window and employing attenuation correction. However, the 6-6% position has similar resolution, and the contrast is only slightly less than at the 4-8% position (in fact, when error limits are considered they are the same). It is interesting to note that the same windows were identified as giving optimal results for lesion 19/80, although in that case attenuation correction was found to be

unhelpful. The indications of Figs.4.6(a) and 4.6(b), that use of attenuation correction was beneficial, with respect to identification and accurate size measurement of this lesion, are confirmed.

Figs.4.10(a) and 4.10(b) are for lesion 16/50, and indicate that attenuation correction improves the contrast of images of this smaller, deeper lesion at all window positions. The contrast, as previously mentioned, increases as the window position is moved towards higher energy. The effect of attenuation correction, on the measured size of this lesion, is more noticeable in this case than either of the others, which is interesting since this is the most difficult of the three to detect and measure. At all window positions attenuation correction causes an increase in the measured diameter of the lesion. As the window position is moved towards higher energy, the measured size of the lesion tends to increase, with or without application of attenuation correction. This trend was also evident for lesion 30/50, but was less marked. The actual size of the lesion lies within the error limits of only one measurement - that obtained without attenuation correction of images

acquired using an 8-4% window. Comparison of Figs.4.10(a) and 4.10(b) with 4.7(a) and 4.7(b) indicates that the probability of detection of this lesion is greatest using a narrow window, perhaps asymmetrically positioned (for example, 6-6% or 4-8%). However, the only realistic measurement of the size of the lesion was obtained with the 8-4% window position, without attenuation correction.

Fig.4.8 Contrast and resolution of lesion 19/80, with and without attenuation correction, plotted against (asymmetric) window size.

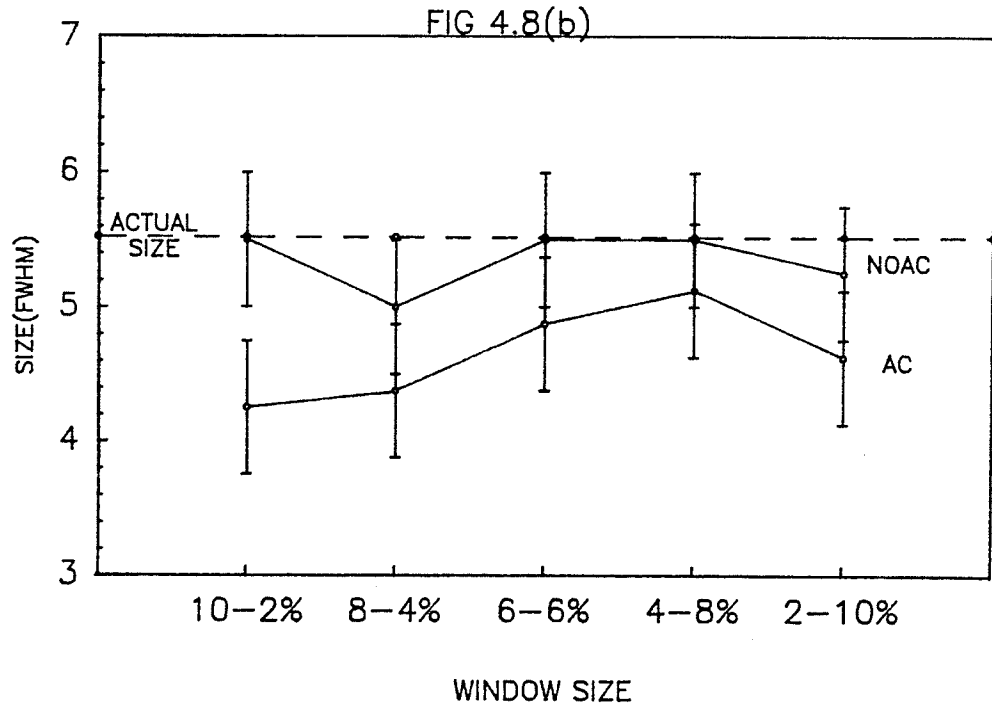
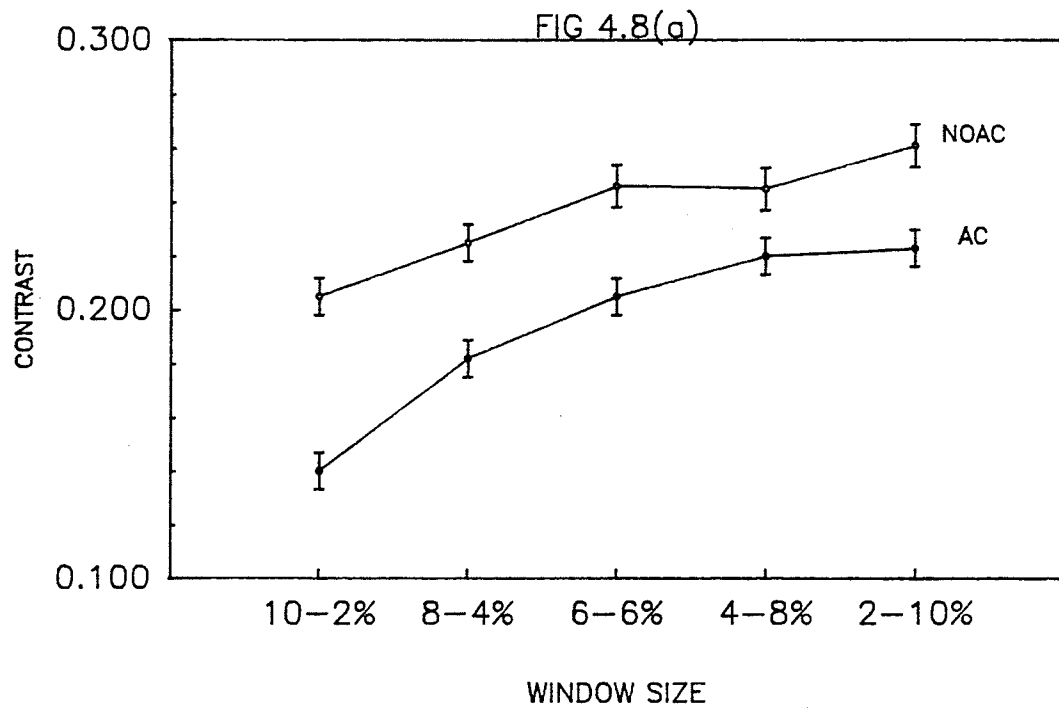


Fig.4.9 Contrast and resolution of lesion 30/50, with and without attenuation correction, plotted against (asymmetric) window size.

FIG 4.9(a)

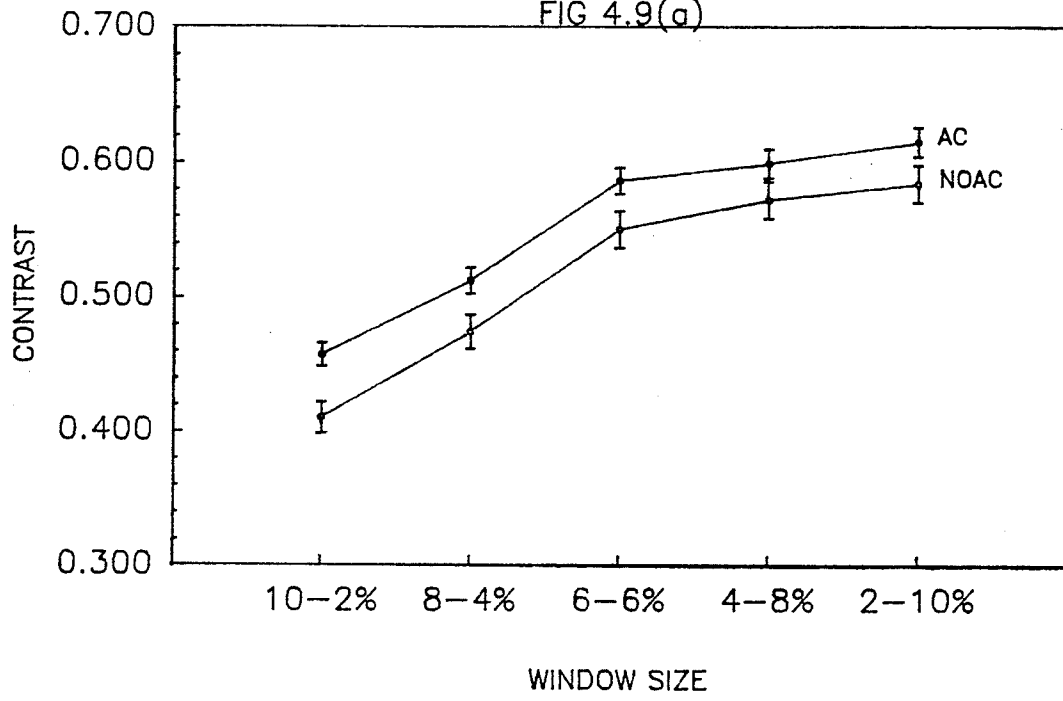


FIG 4.9(b)

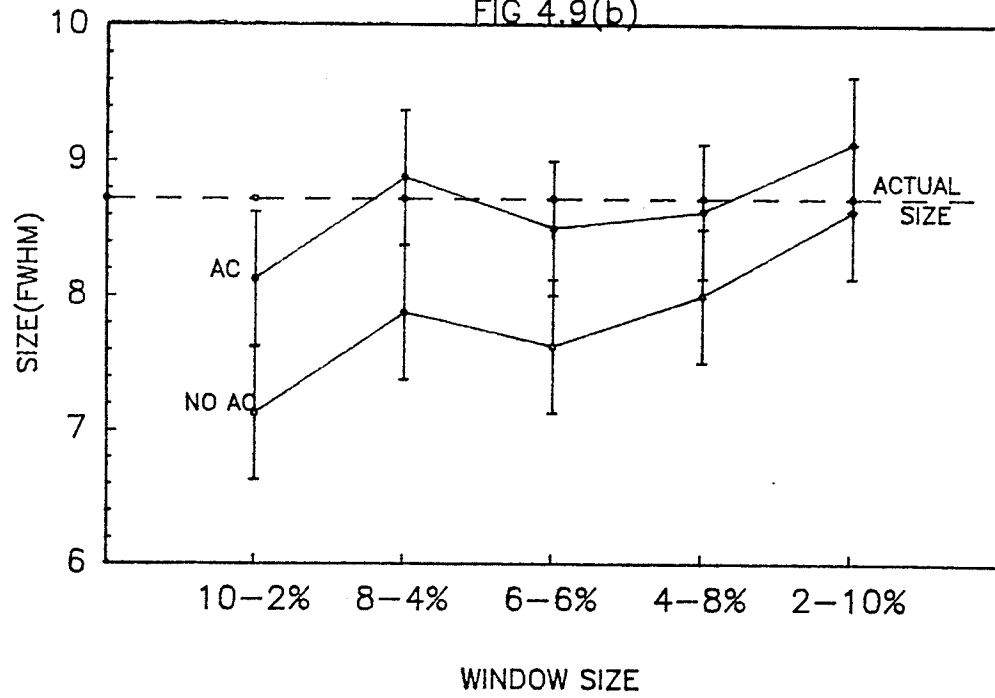


Fig.4.10 Contrast and resolution of lesion 16/50, with and without attenuation correction, plotted against (asymmetric) window size.

FIG 4.10(a)

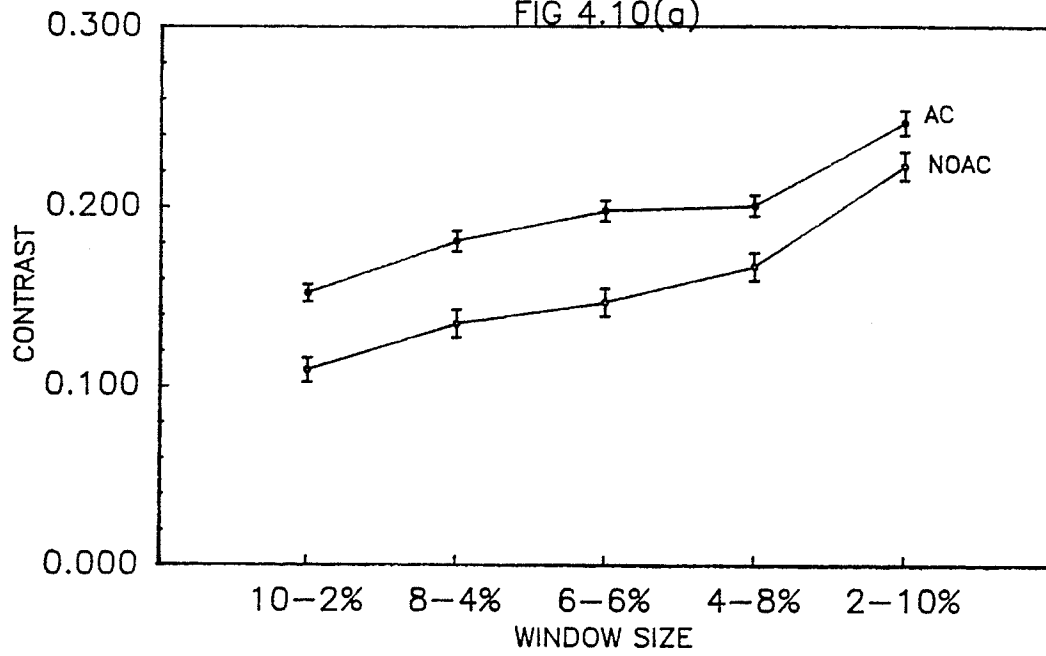
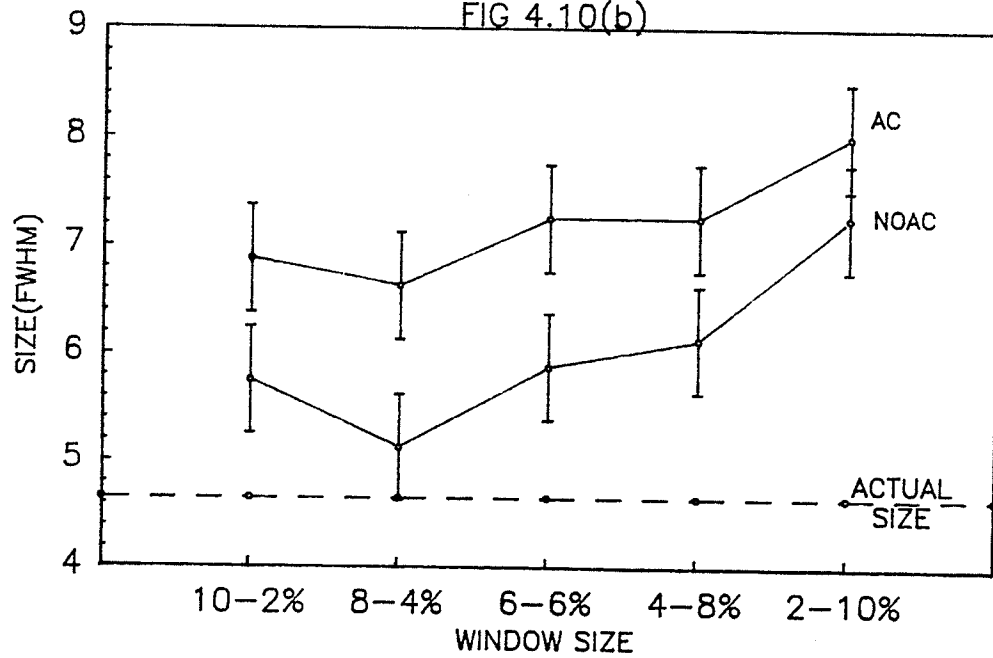


FIG 4.10(b)



(e) SUBTRACTION IMAGES

Figs.4.11, 4.12 and 4.13 illustrate the effect, on the contrast and resolution of images of lesion 19/80 acquired using 10-10%, 8-4% and 6-6% windows on the photopeak, of subtracting images reconstructed from data acquired with the energy window located on the Compton peak. Prior to subtraction, all images have undergone attenuation correction, using the appropriate values of attenuation coefficient, as indicated in Table 4.3.

For the 10-10% photopeak images, contrast of 1.000 and a measured diameter equal to the actual size of the lesion are obtained when the subtracted fraction, k , is 0.6.

For the 8-4% photopeak images, Fig.4.12 indicates that the actual size of the lesion lies within the uncertainty limits of the diameter measurements, when the subtracted fraction is 0.5. The corresponding contrast is 1.000.

Fig.4.13 indicates that, for images acquired with a 6-6% photopeak window, when the subtraction fraction is 0.8, the measured size of the lesion is equal to the actual size, and the contrast is 1.000.

Comparison of Figs.4.11, 4.12 and 4.13 with Figs.4.5 and 4.8 respectively, which also refer to lesion 19/80, reveals that much higher contrast can be achieved using the subtraction technique; the maximum contrast achieved at any window size, with or without attenuation correction is 0.261, while a contrast of 1.000 may be readily obtained for this lesion, at any of the three window sizes mentioned, by use of the appropriate subtraction fraction.

Fig.4.11 Contrast and resolution of lesion 19/80, plotted against subtraction fraction, for images acquired with 10-10% window on the photopeak.

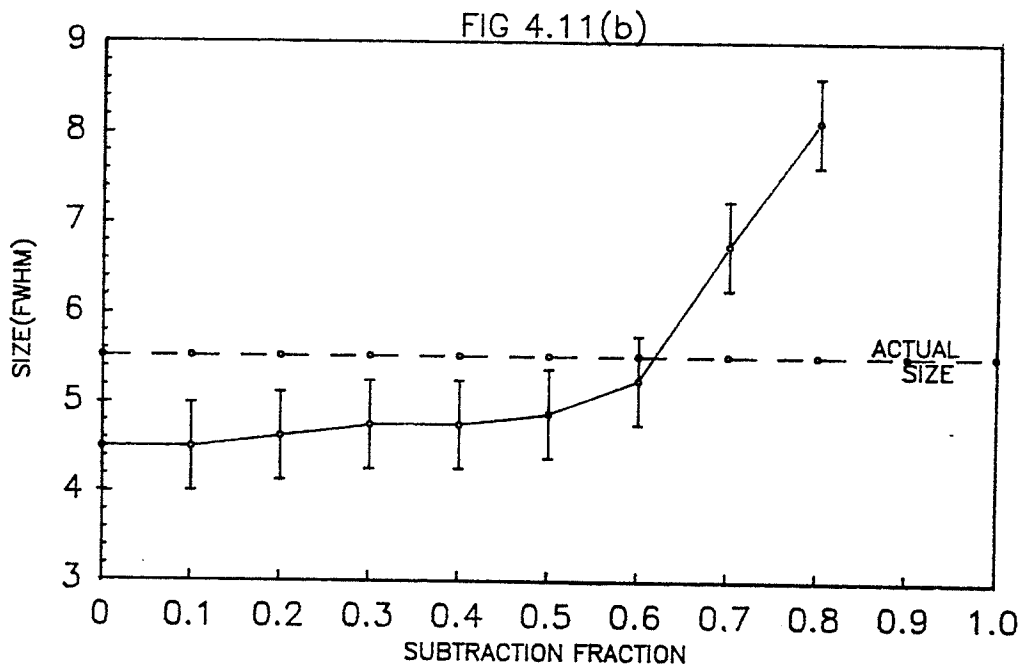
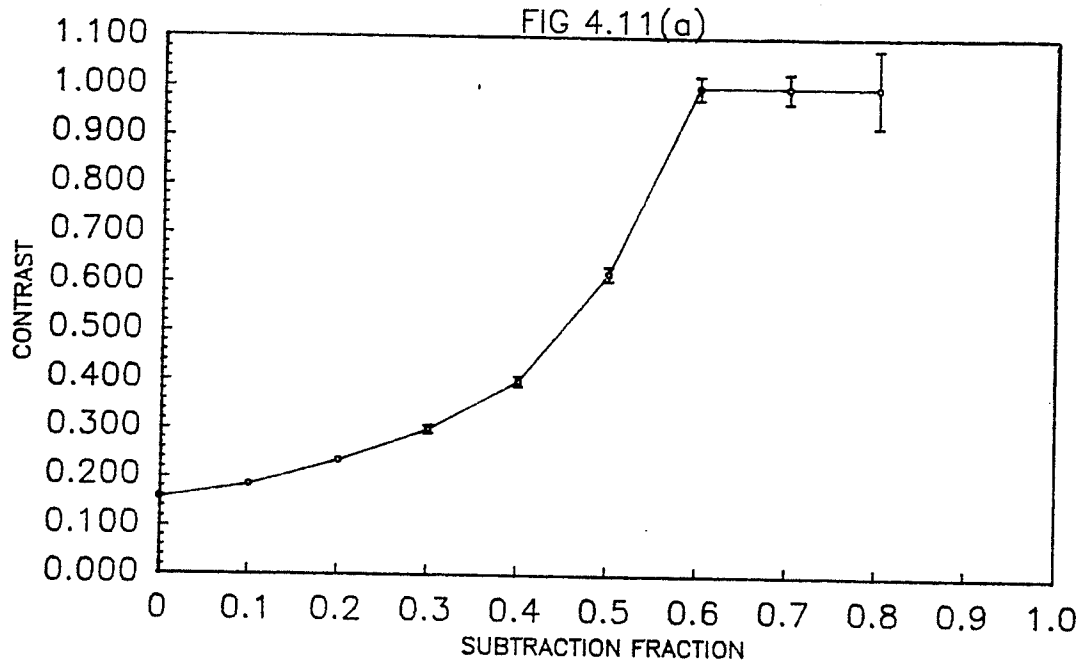


Fig.4.12 Contrast and resolution of lesion 19/80, plotted against subtraction fraction, for images acquired with 8-4% window on the photopeak.

FIG 4.12(a)

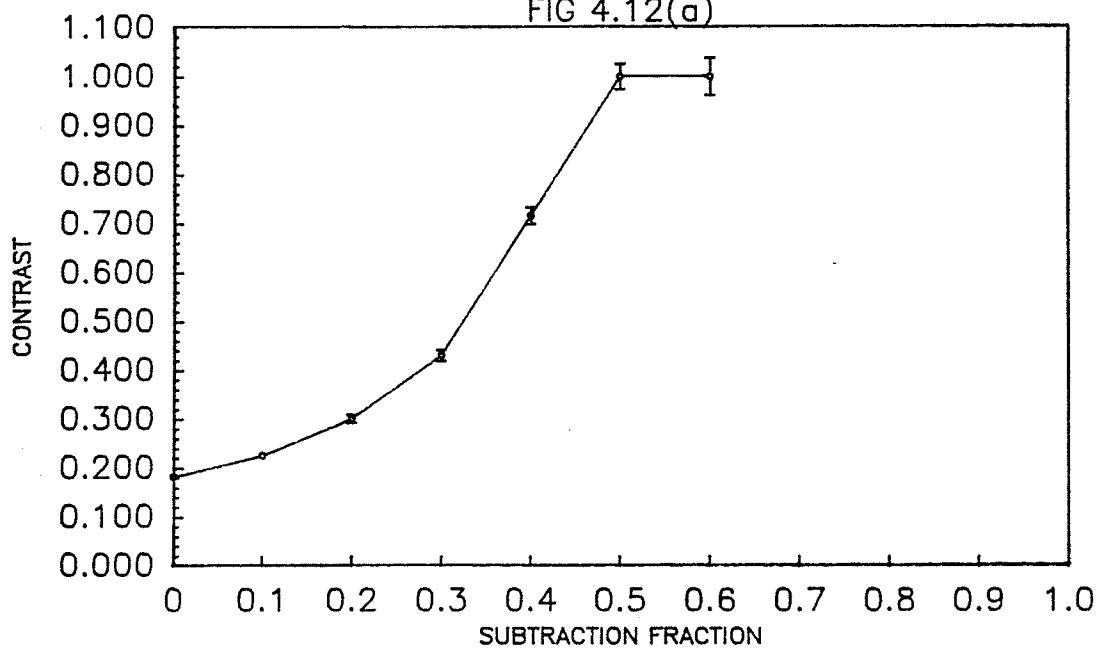


FIG 4.12(b)

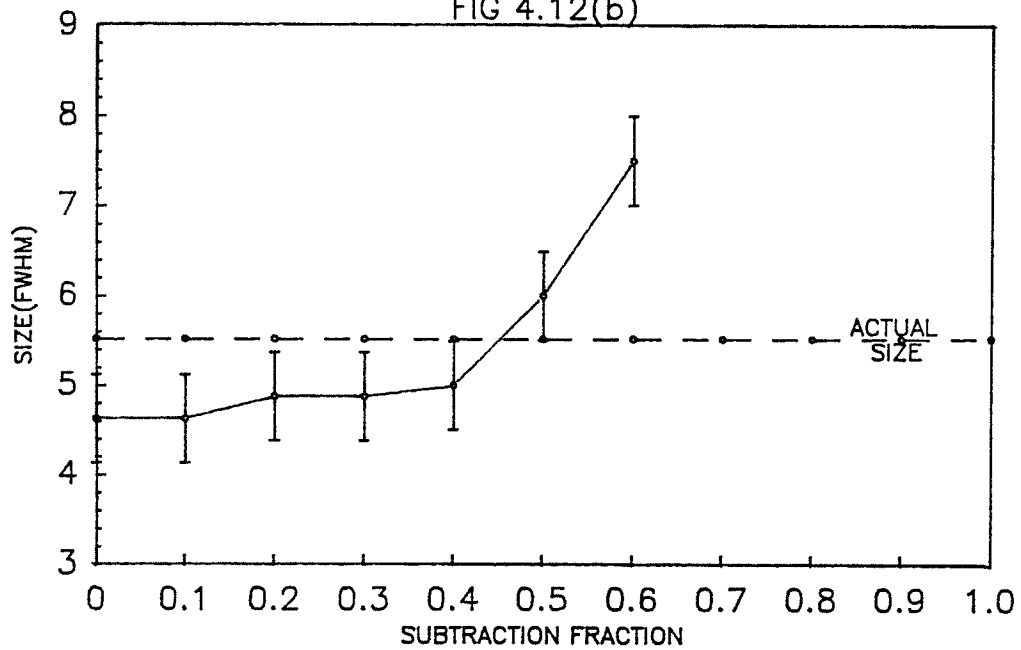
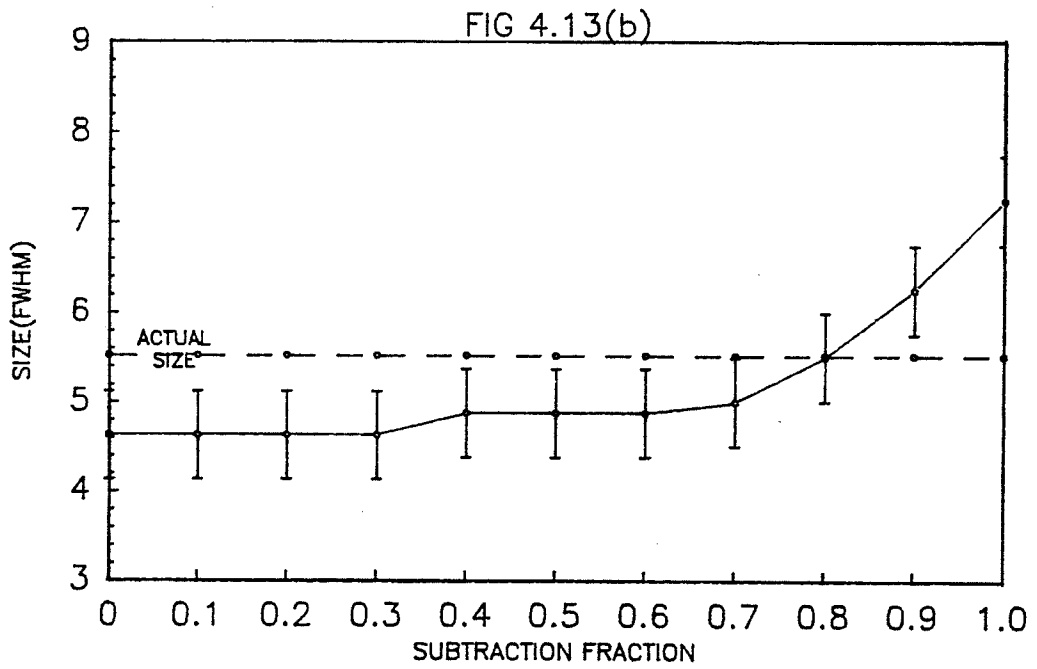
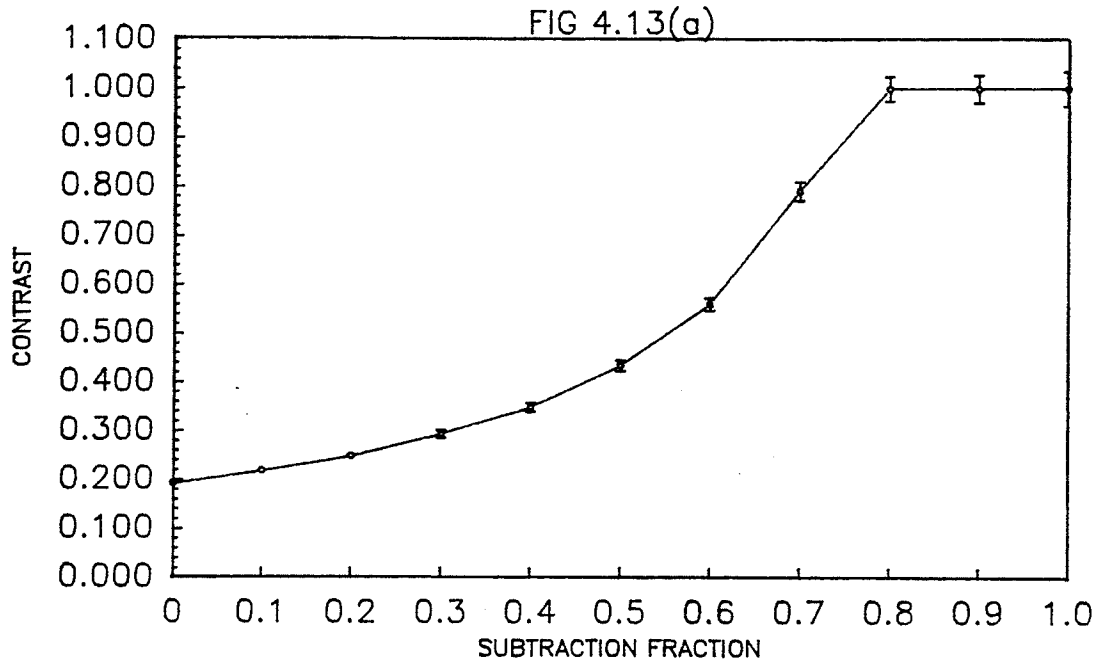


Fig.4.13 Contrast and resolution of lesion 19/80,
plotted against subtraction fraction, for images
acquired with 6-6% window on the photopeak.



Figs.4.14, 4.15 and 4.16 refer to lesion 30/50 images, acquired using 10-10%, 8-4% and 6-6% windows on the photopeak, which have undergone subtraction as described above.

For the 10-10% photopeak images, the contrast increases to reach a value of 1.000 when k is 0.4. For $k = 0.4$ the actual size of the lesion is within the limits of error of the measurements of the lesion diameter.

In Fig.4.15, the contrast reaches 1.000 when k is 0.3, and the measured diameter is representative of the actual size of the lesion.

In Fig.4.16, the contrast reaches a value of 1.000 when k is 0.5, and the actual size of the lesion is within the limits of uncertainty of the corresponding measured diameter.

Once again, it is noticeable that, whatever the size of the energy window used for data acquisition, it is possible to obtain much better contrast by this method, and to obtain more reliably an accurate measurement of

the diameter of the lesion under study, than by using only the symmetric or asymmetric windows as described earlier.

Fig.4.14 Contrast and resolution of lesion 30/50, plotted against subtraction fraction, for images acquired with 10-10% window on the photopeak.

FIG 4.14(a)

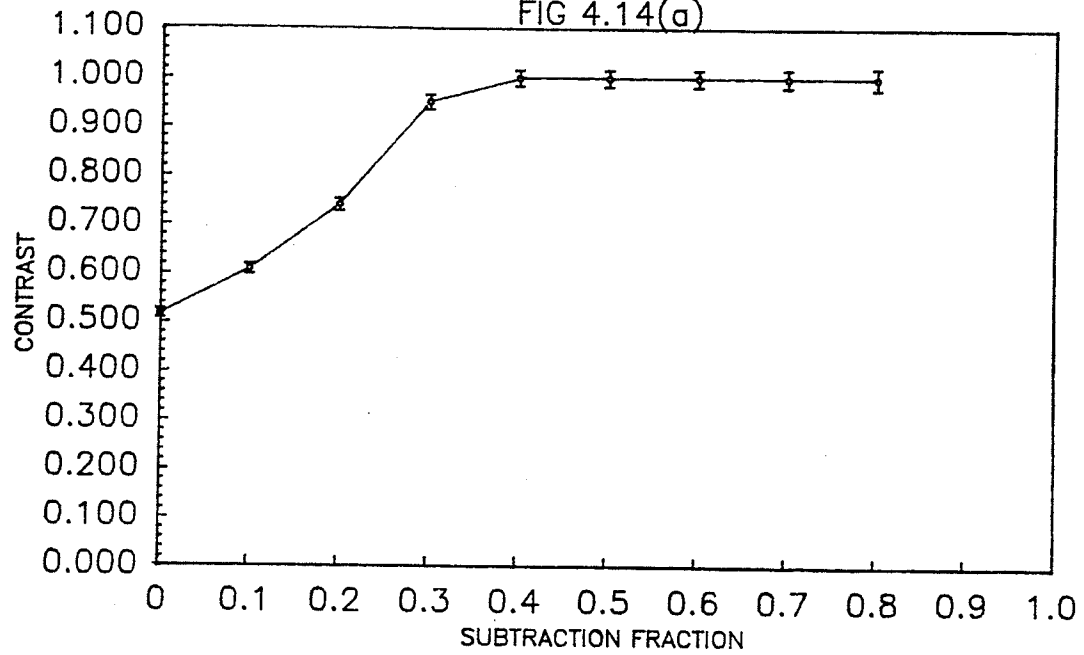


FIG 4.14(b)

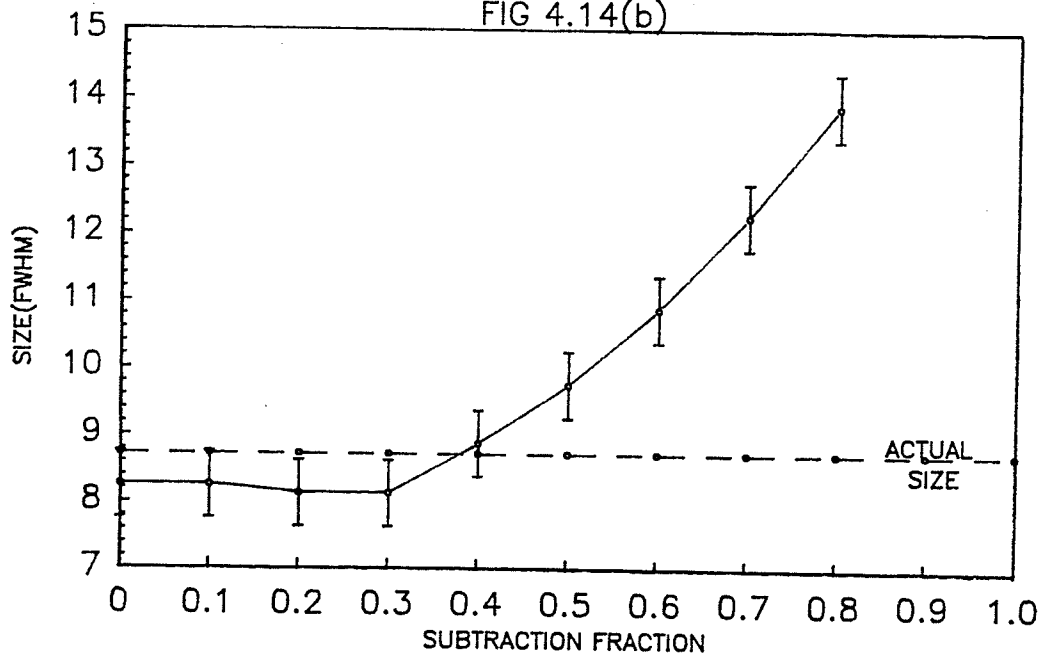


Fig.4.15 Contrast and resolution of lesion 30/50,
plotted against subtraction fraction, for images
acquired with 8-4% window on the photopeak.

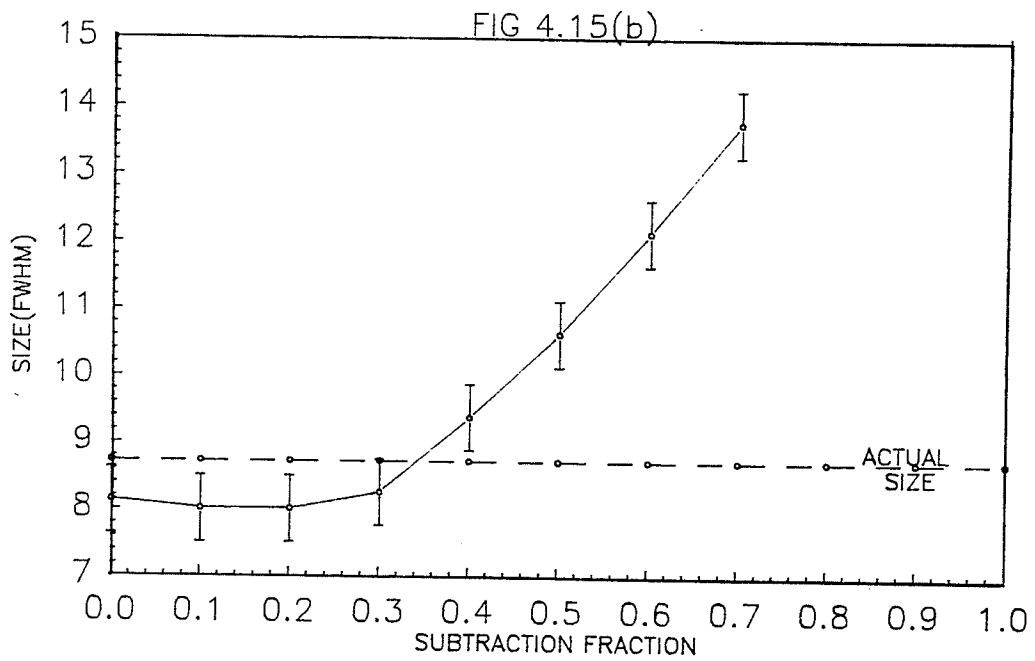
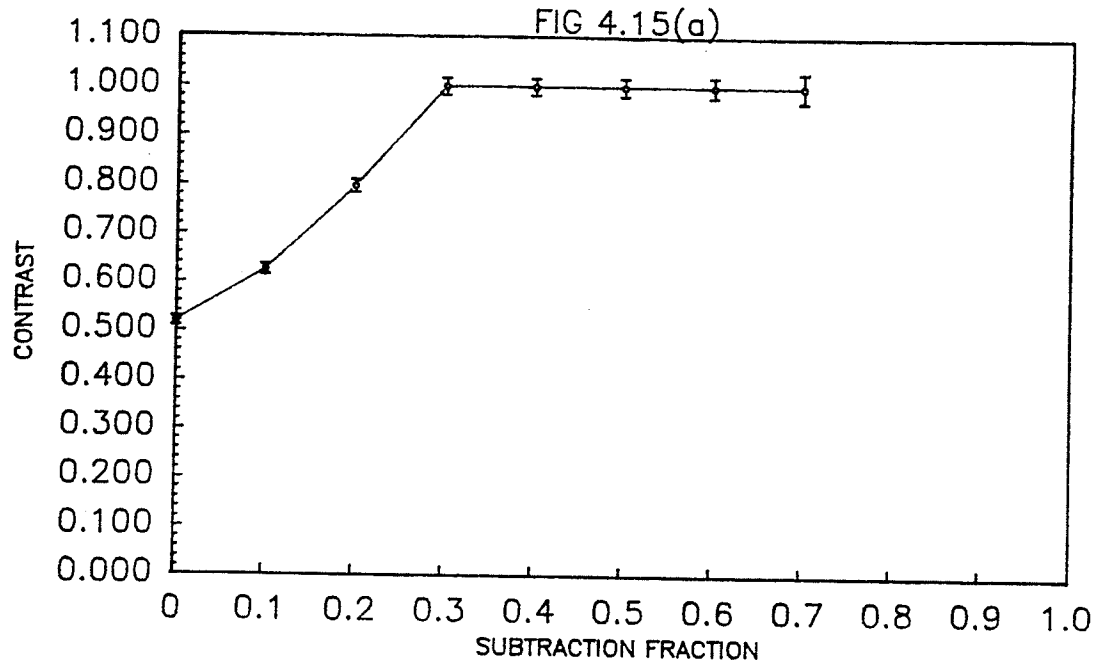
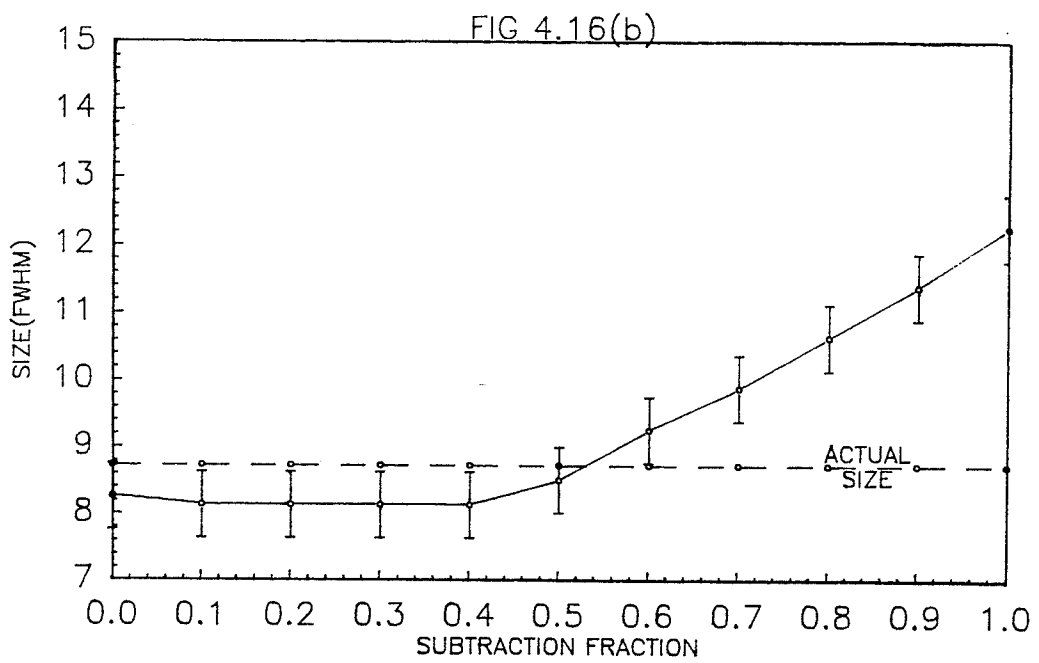
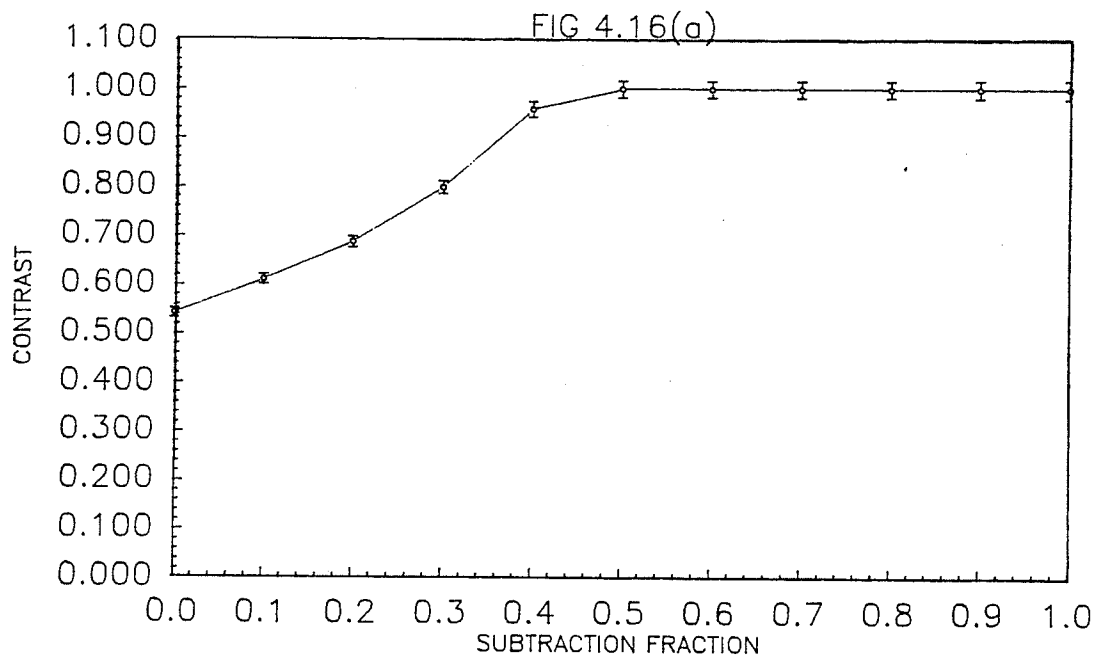


Fig.4.16 Contrast and resolution of lesion 30/50, plotted against subtraction fraction, for images acquired with 6-6% window on the photopeak.



Figs.4.17, 4.18 and 4.19 refer to the contrast and resolution of images of lesion 16/50, subsequent to subtraction of scatter images, obtained with 10-10%, 8-4% and 6-6% energy windows on the photopeak. Attenuation correction was applied to all images prior to subtraction.

Fig.4.17(a) shows that contrast of 1.000 is achieved with the 10-10% images when the subtracted fraction is 0.7. The resolution is never good, the actual size of the lesion never falling within the error limits of the measured values. Resolution is better when the 8-4% window is used, as illustrated by Fig.4.18(b), particularly at the lower k values. For k in the range 0.2 to 0.5 the measured values are close to the actual size. The contrast does not reach the value of 1.000 until k is 0.6, although the contrast at all values of k greater than 0.2, is higher than obtained for this lesion without using the subtraction technique. The resolution for k in the range 0.0 to 0.5 is also better than that achieved without subtraction.

Fig.4.19(a) indicates that, when data is acquired

with a 6-6% window on the photopeak, the contrast does not become 1.000 until the subtracted fraction of the scatter image is 1.0. The resolution is never good - the actual size of the lesion never lies within the error limits of the measured diameter.

Perhaps, for this lesion, the best compromise is obtained when an 8-4% photopeak window is used for acquisition, followed by subtraction of the scatter image using a value for k of 0.5. However, detection and measurement of the size of this lesion is perhaps the most demanding test of these techniques, so it is encouraging to find that this subtraction method can provide very noticeable advantages.

Fig.4.17 Contrast and resolution of lesion 16/50,
plotted against subtraction fraction, for images
acquired with 10-10% window on the photopeak.

FIG 4.17(a)

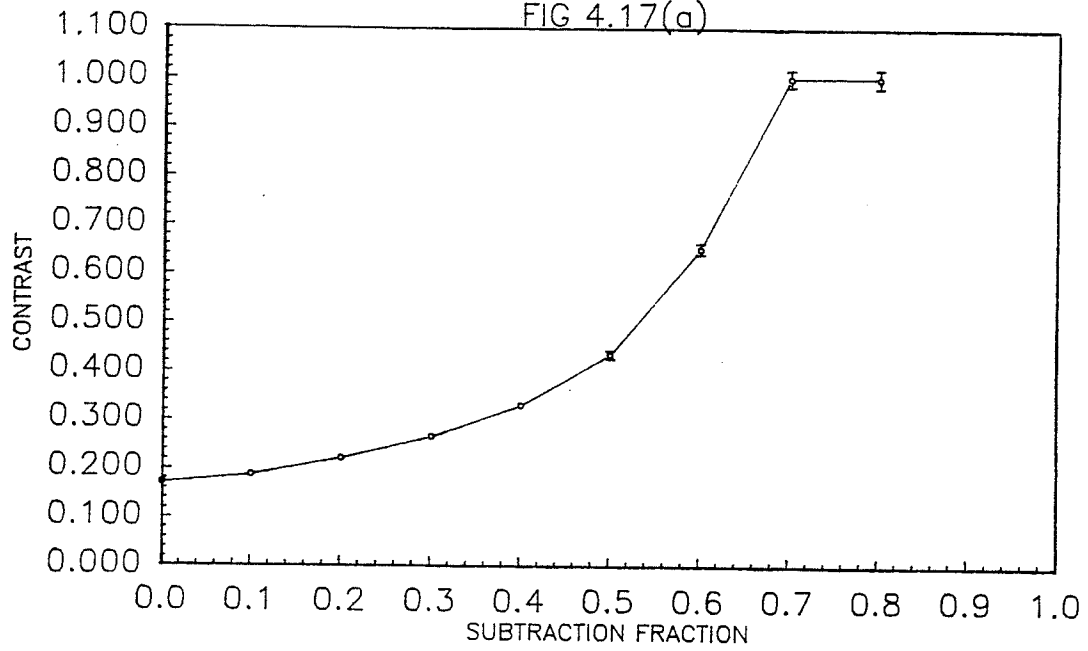


FIG 4.17(b)

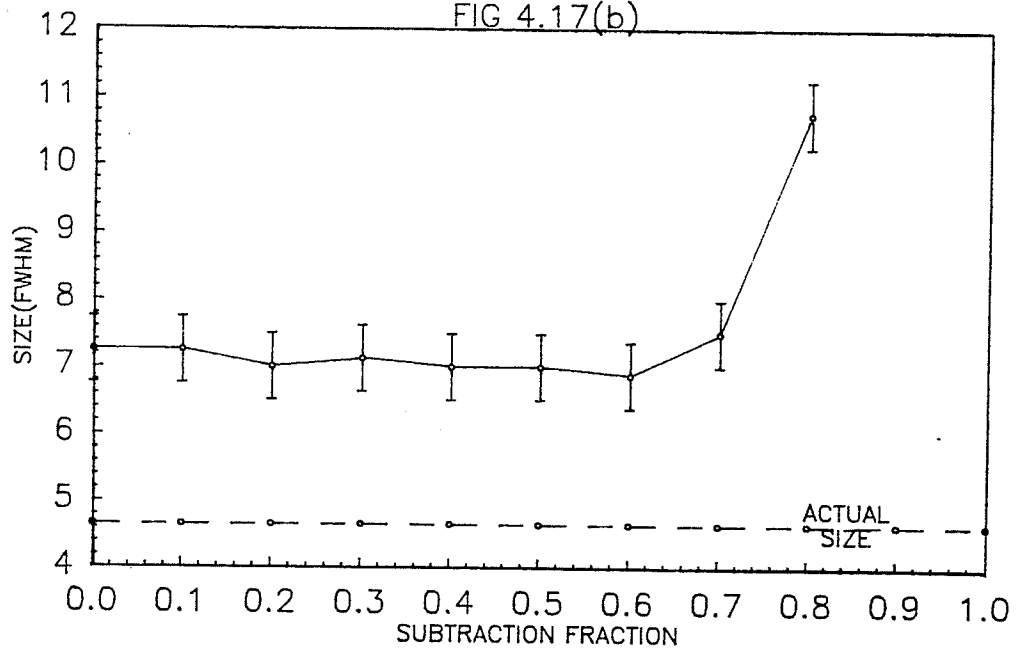


Fig.4.18 Contrast and resolution of lesion 16/50, plotted against subtraction fraction, for images acquired with 8-4% window on the photopeak.

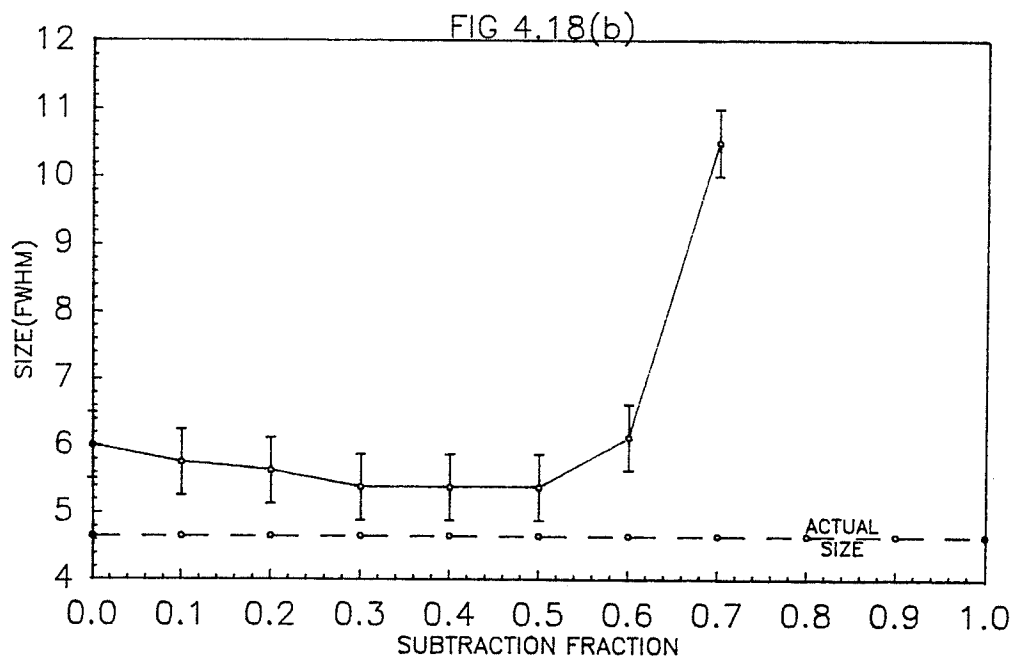
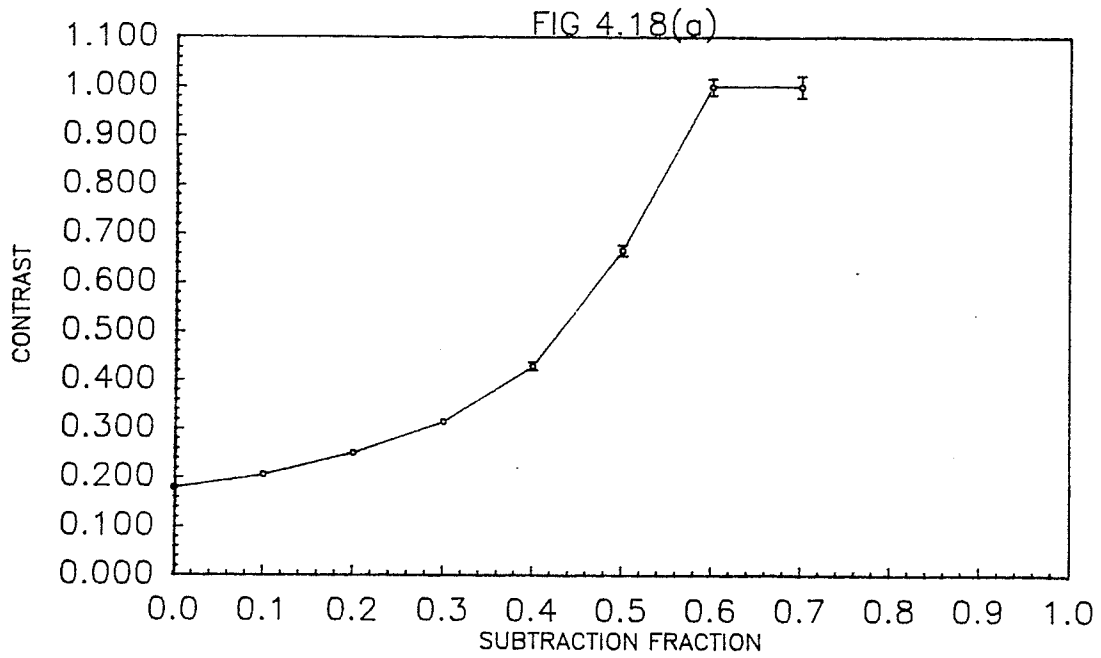


Fig.4.19 Contrast and resolution of lesion 16/50,
plotted against subtraction fraction, for images
acquired with 6-6% window on the photopeak.

FIG 4.19(a)

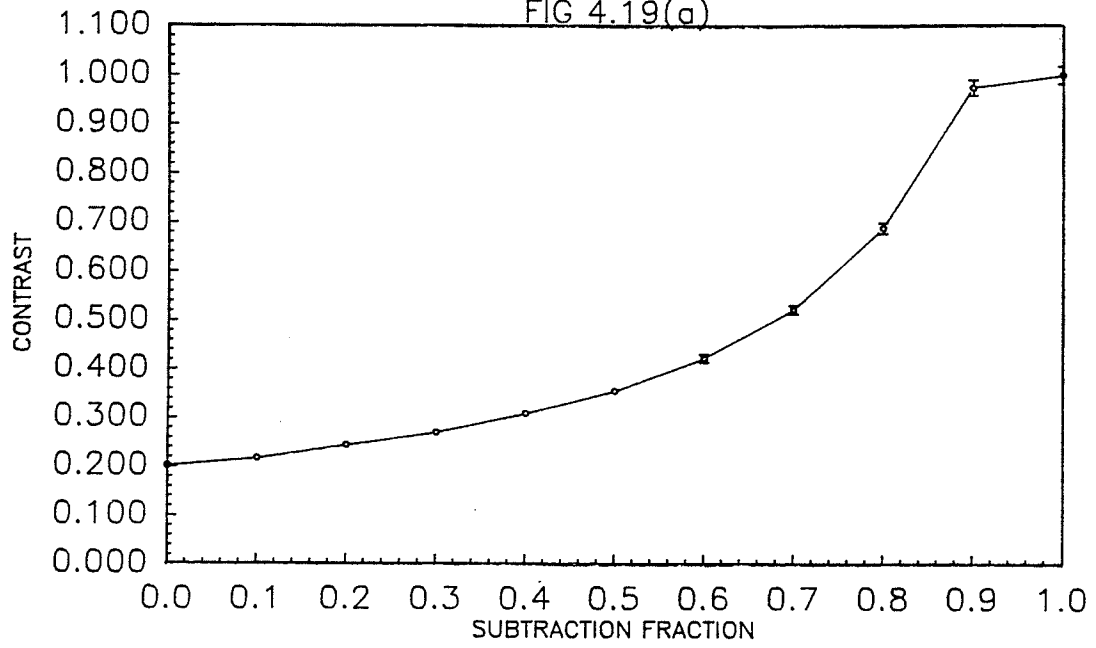
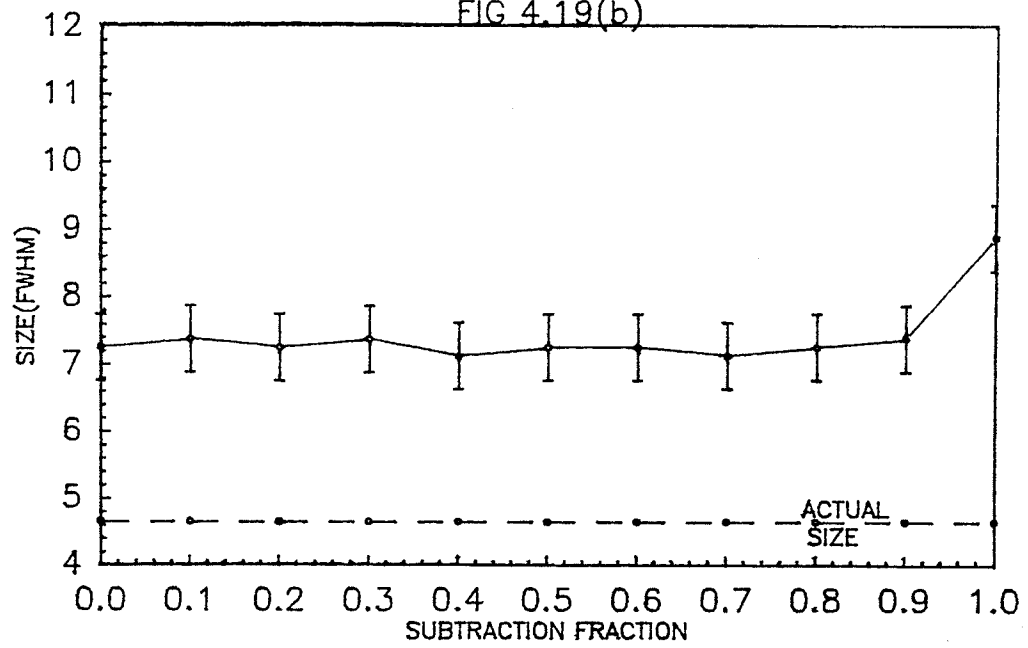


FIG 4.19(b)



In evaluating the images obtained by subtracting scatter images from photopeak images, many variables have to be considered, in order to select the best compromise between contrast and resolution. To help identify the optimal set of conditions, a quantity, which will be called the "resolution ratio", has been defined to be the actual size of the lesion divided by the measured diameter, both quantities in pixels. The ideal set of parameters would be those which result in a contrast of 1.000 and a resolution ratio of 1.000. For each lesion and each photopeak window, contrast is plotted against resolution ratio for each k value.

Fig.4.20 is for lesion 19/80 images acquired with a 10-10% window on the photopeak. It indicates that the optimal value of k is close to 0.6, because, although $k = 0.7$ also produces a contrast of 1.000, the corresponding resolution ratio is much less than when k is 0.6. By drawing a smooth curve and interpolating, the "true" optimum value of k may be obtained, although the clinical benefit of this additional effort is questionable.

Fig.4.21 is for lesion 19/80 with an 8-4% window on

the photopeak. In this case, $k = 0.5$, for which the contrast is 1.000 and the resolution ratio is 0.920, is probably the best compromise. Again, interpolation could be used to find the "true" optimum subtraction fraction.

Fig.4.22 is also for lesion 19/80, but with a 6-6% window on the photopeak. In this case, use of k values less than 0.8 results in decreased contrast, and resolution ratios in excess of 1.000. When k is 0.8, the contrast is 1.000 and the resolution ratio is 1.004.

Fig.4.20 Contrast plotted against resolution ratio for
lesion 19/80, 10-10% photopeak window.

Fig.4.21 Contrast plotted against resolution ratio for
lesion 19/80, 8-4% photopeak window.

FIG 4.20

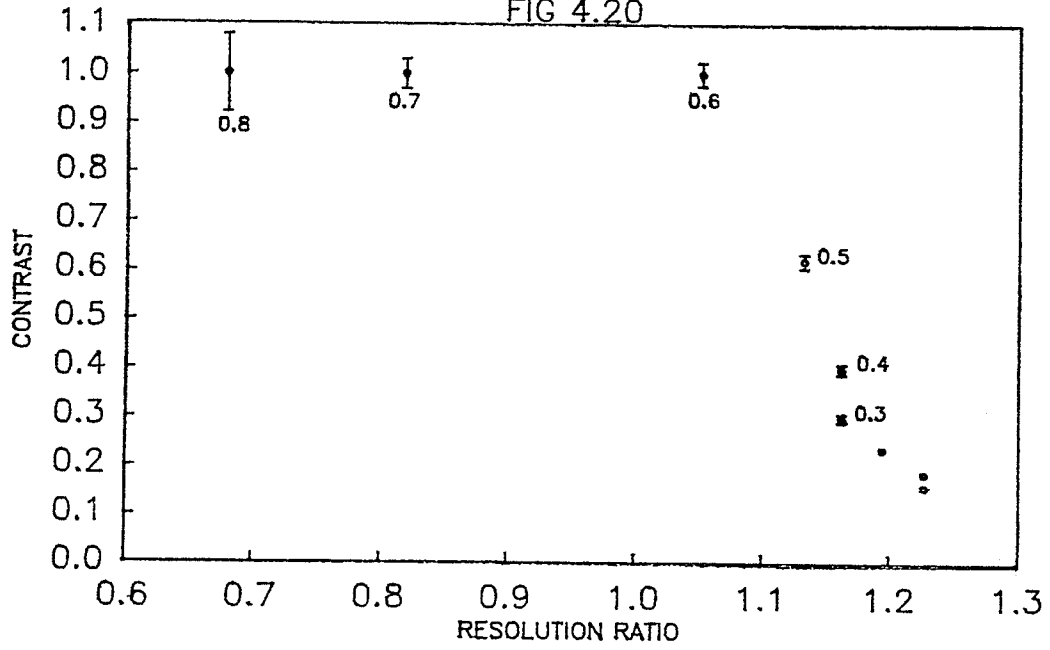


FIG 4.21

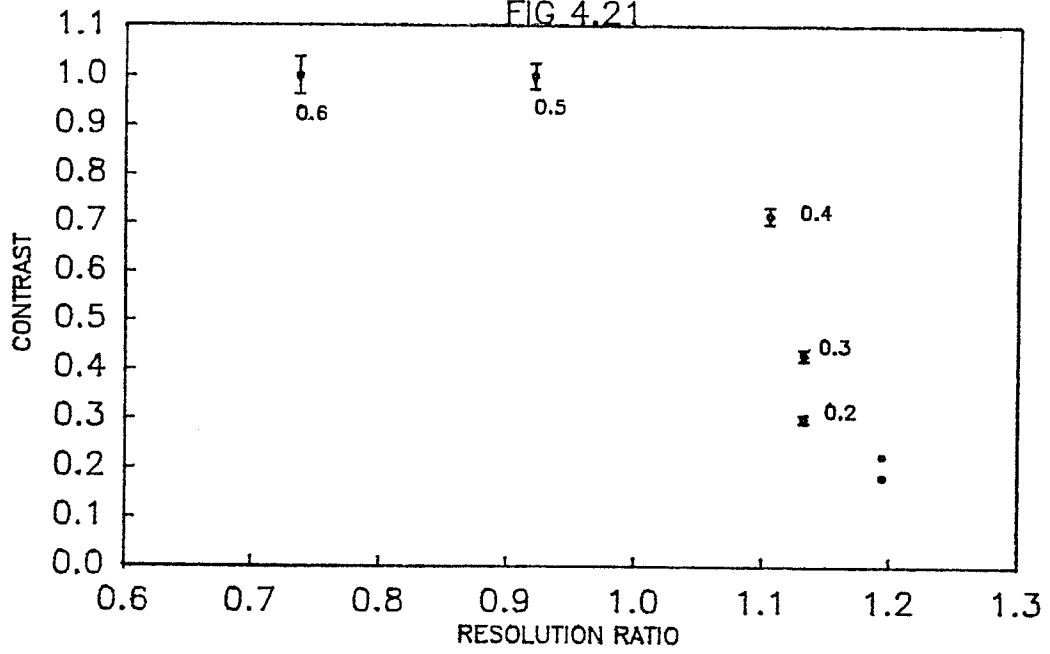


Fig.4.22 Contrast plotted against resolution ratio for
lesion 19/80, 6-6% photopeak window.

FIG 4.22

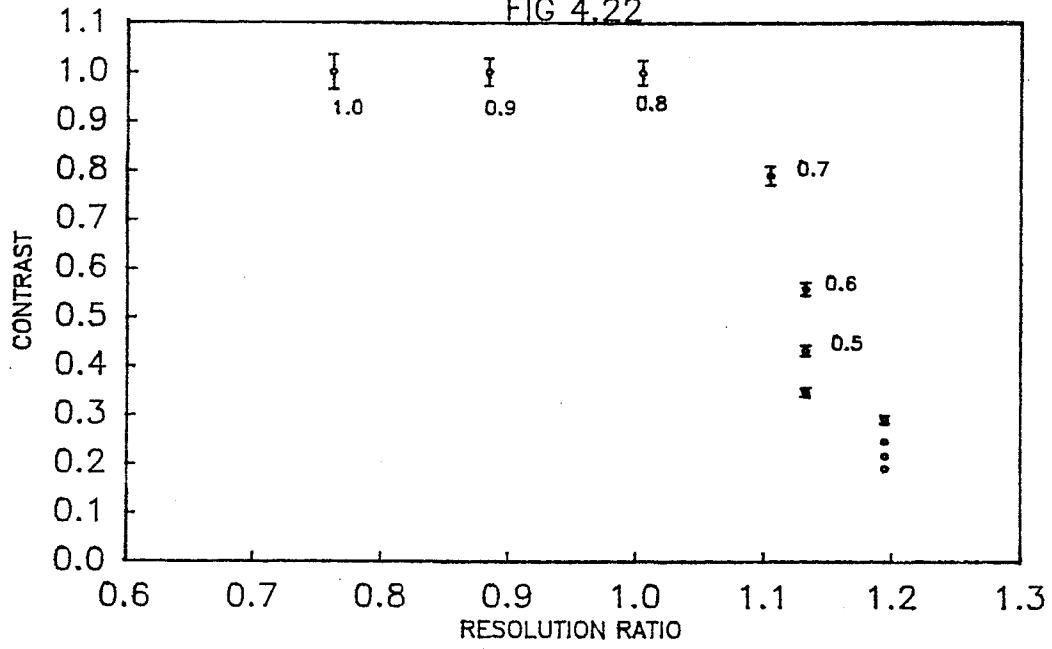


Fig.4.23 shows the equivalent information for lesion 30/50, when the photopeak window is 10-10%. This is interesting because of the wide range of values of k for which the contrast is 1.000. The optimal value must be decided, on the basis of the resolution ratio, which suggests a k value close to 0.4.

Fig.4.24 also refers to lesion 30/50, but with the 8-4% window on the photopeak. It also indicates that the optimal value of k is close to 0.4. Fig.4.25 suggests a k value close to 0.6, when the photopeak window is 6-6%.

Fig.4.23 Contrast plotted against resolution ratio for
lesion 30/50, 10-10% photopeak window.

Fig.4.24 Contrast plotted against resolution ratio for
lesion 30/50, 8-4% photopeak window.

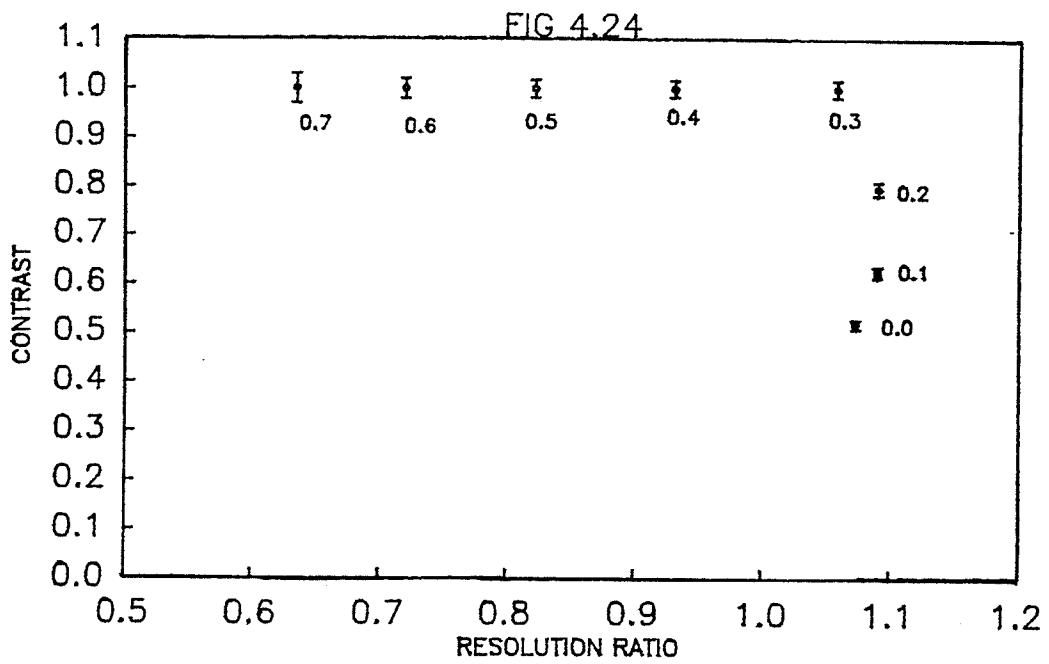
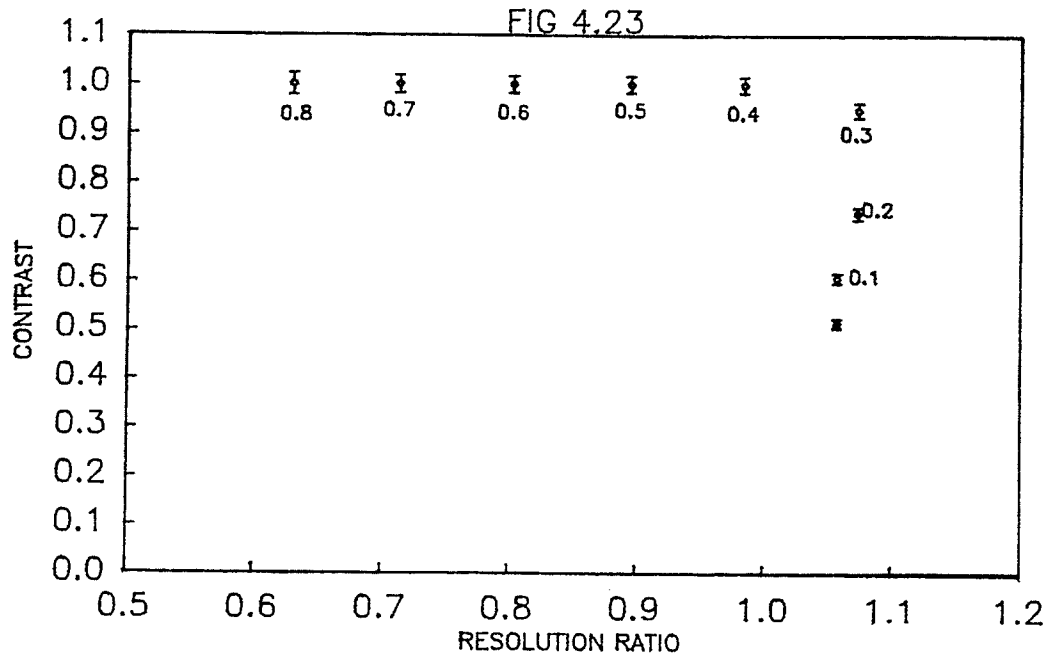


Fig.4.25 Contrast plotted against resolution ratio for
lesion 30/50, 6-6% photopeak window.

FIG 4.25

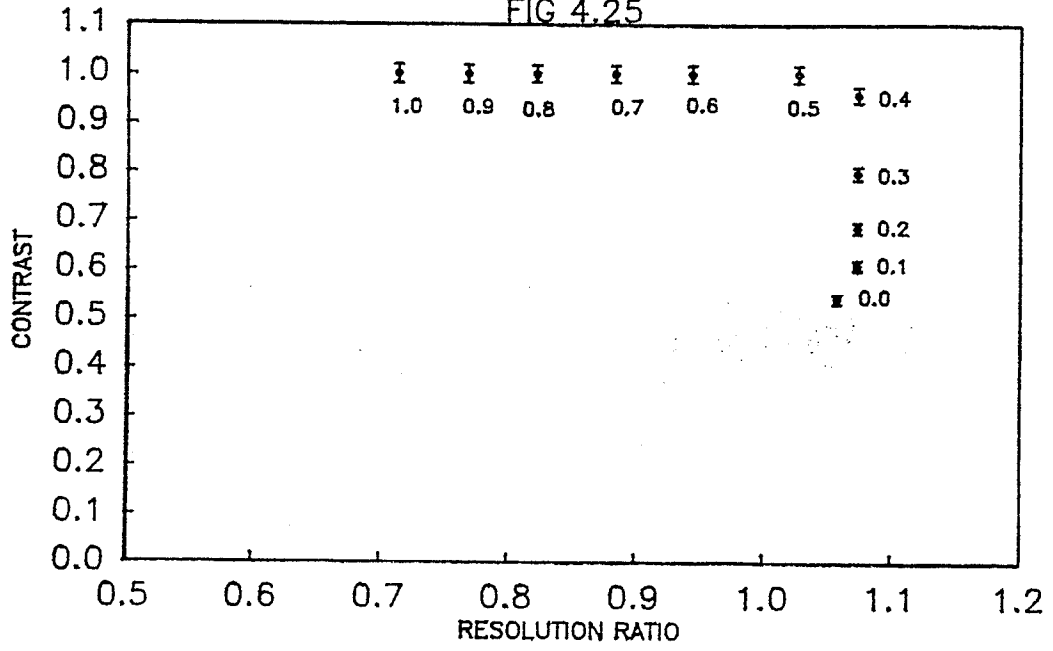


Fig.4.26 illustrates the contrast and resolution ratio for images of lesion 16/50, acquired with a photopeak window of 10-10%. The resolution ratio is never better than 0.676 and, when the contrast attains its maximum value of 1.000, the resolution ratio is only 0.620 at best. A 6-6% window on the photopeak is also not very satisfactory, as shown in Fig.4.28. In this case, the resolution ratio is never better than 0.653, and when the contrast is 1.000 the resolution ratio is only 0.524.

This information suggests that for this small, deep lesion, neither a 10-10% nor a 6-6% window is the best to use. This is confirmed by the results obtained using an 8-4% window, summarized in Fig.4.27. A resolution ratio of 0.865 and contrast of 0.666 can be achieved with a value of k of 0.5, or, when k is 0.6, a resolution ratio and contrast of 0.759 and 1.000 respectively can be achieved.

Fig.4.26 Contrast plotted against resolution ratio for
lesion 16/50, 10-10% photopeak window.

Fig.4.27 Contrast plotted against resolution ratio for
lesion 16/50, 8-4% photopeak window.

FIG 4.26

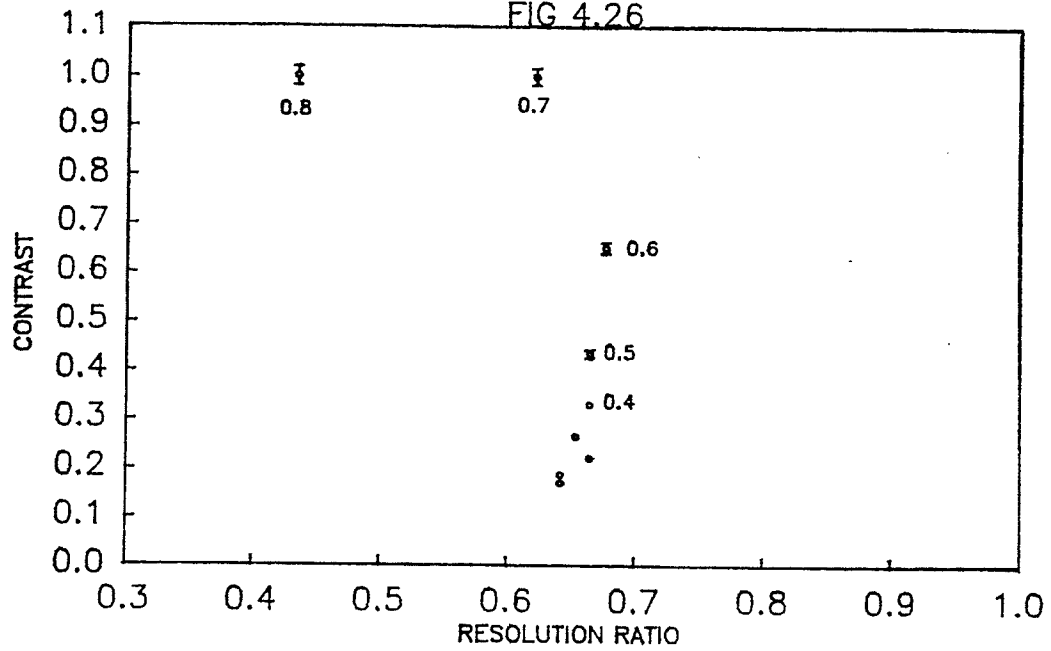


FIG 4.27

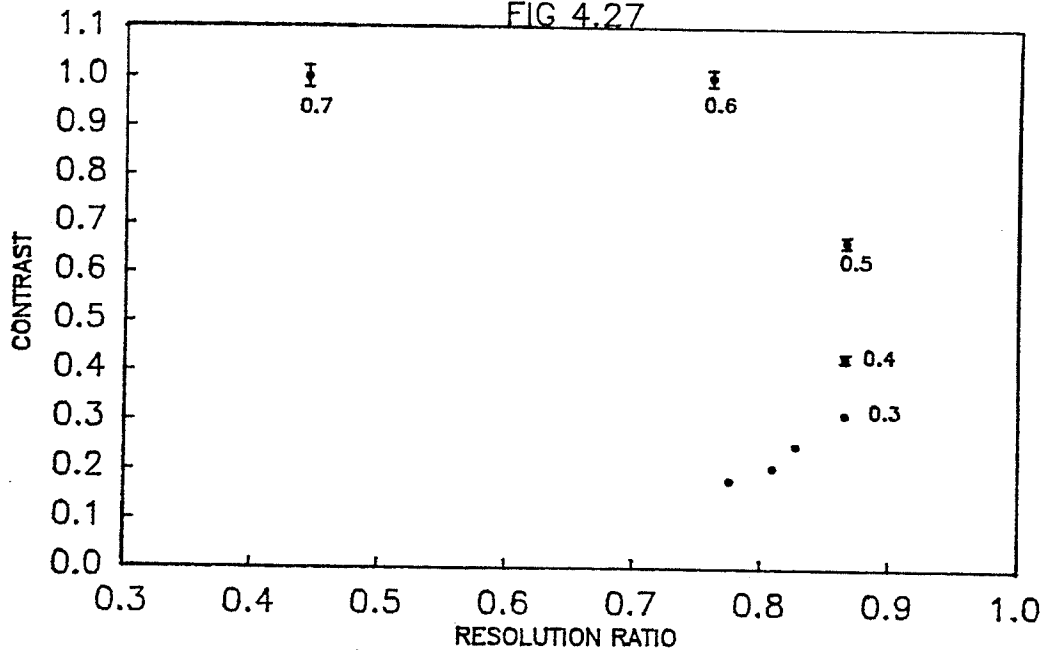
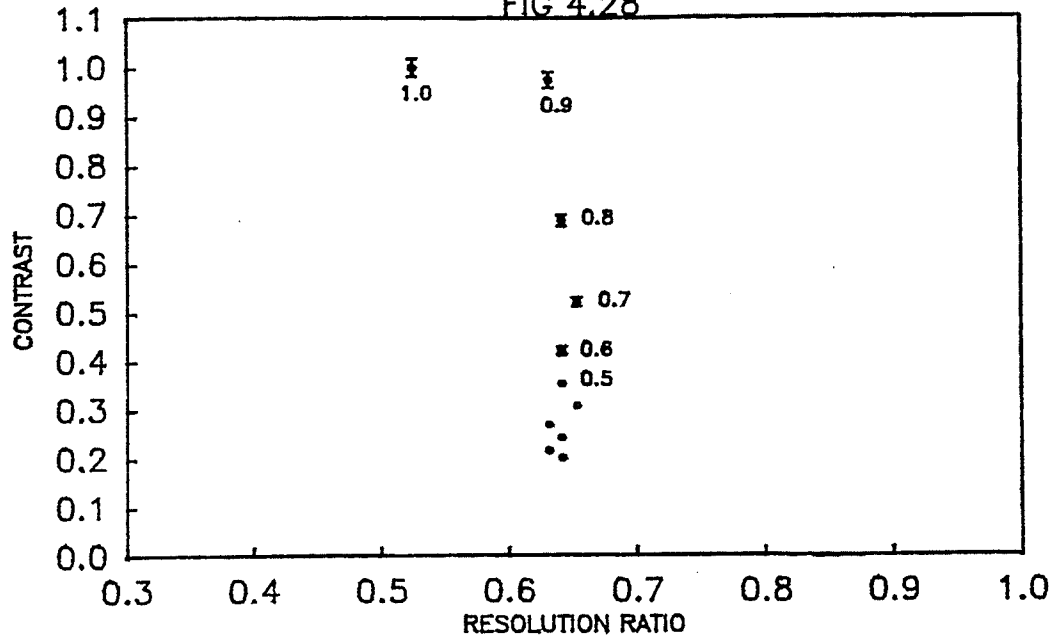


Fig.4.28 Contrast plotted against resolution ratio for
lesion 16/50, 6-6% photopeak window.

FIG 4.28



CHAPTER V CONCLUSION

The aim of this study was to investigate the possible improvement of SPECT image quality, resulting from the application of scatter and attenuation correction, within a clinically acceptable time-span. The width and position of the energy window was varied during data acquisition, and the effect upon lesion contrast and resolution was evaluated. A separate "scatter window" technique was also examined.

Chang's method of attenuation correction was also considered. This method required the experimental determination of the attenuation coefficient, for which a new, clinically expedient, procedure was developed.

The width of the symmetric window did not effect the contrast and resolution appreciably or predictably. Positioning the asymmetric window towards higher energies brought about an overall trend to increased contrast. By far the greatest improvements in image quality resulted from subtraction of images obtained using a Compton scatter window from those obtained using a window on the photopeak. Fourfold improvements in the contrast were achieved using this technique. Selection of the optimal

value of subtraction fraction can therefore improve the detectability of a lesion and can also permit a realistic assessment of lesion size.

Used appropriately in a clinical setting, this technique could significantly improve both image quality and the effectiveness of SPECT diagnostic procedures, in a nuclear medicine department.

The quality of SPECT images could be further improved by optimization of the reconstruction filter to the lesion size and noise characteristics expected in the image. The use of non-circular orbits, in which the detector is, on average, closer to the scanned object, may be expected to improve image quality and should be investigated.

CHAPTER VI REFERENCES

- Anger HO. Scintillation camera with multi-channel collimators. *J Nucl Med* 1964; 5:515.
- Axelsson B, Msaki P, Israelsson A. Subtraction of Compton scattered photons in single photon emission computed tomography. *J Nucl Med* 1984; 25:490-494.
- Axelsson B, Israelsson A, Larsson SA. Studies of a technique for attenuation correction in single photon emission computed tomography. *Phys Med Biol* 1987; 32(6):737-749.
- Bailey DL, Hutton BF, Walker PJ. Improved SPECT using simultaneous emission and transmission tomography. *J Nucl Med* 1971; 28:844-851.
- Beck JW. Analysis of a camera-based single photon emission computed tomography (SPECT) system. [Ph.D thesis]. Ann Arbor, Michigan: Duke University, 1982.

Blinchikoff HJ, Zverev AI. Filtering in the time and frequency domains. New York: John Wiley and Sons, 1976.

Bracewell RN. The Fourier transform and its applications. New York: McGraw-Hill, 1965.

Budinger TF, Gullberg GT, Huesman RH. Emission computed tomography. In: Herman GT, ed. Topics in applied physics (vol 32): Image reconstruction from projections, implementation and applications. Heidelberg: Springer-Verlag, 1979.

Chang LT. A method for attenuation correction in radionuclide computed tomography. IEEE Trans Nucl Sci 1978; NS-25: 638.

Childers D, Durling A. Digital filtering and signal processing. New York: West Publishing Company, 1975.

Compton AH. A quantum theory of the scattering of X-rays by light elements. Phys Rev 1923; 21:483-502.

- Croft BY, Teates CD, Honeyman JG. Single photon emission computed tomography of the liver in digital imaging. In: Esser PD, ed. Clinical advances in nuclear medicine. New York: Society of Nuclear Medicine, 1982.
- Eisberg R, Resnick R. Quantum physics of atoms, molecules, solids, nuclei and particles. New York: John Wiley and Sons, 1974.
- English RJ, Brown SE. Single photon emission computed tomography (SPECT): a primer. New York: Society of Nuclear Medicine Inc., 1986.
- Floyd Jr. CE, Jaszczak RJ, Greer KL, Coleman RE. Deconvolution of Compton scatter in SPECT. J Nucl Med 1985; 26:403-408.
- Floyd Jr. CE, Jaszczak RJ, Greer KL, Coleman RE. Inverse Monte Carlo as a unified reconstruction algorithm for ECT. J Nucl Med 1986; 27:1577-1585.
- Floyd Jr. CE, Jaszczak RJ, Harris CC, Coleman RE. Energy

and spatial distribution of multiple order Compton scatter in SPECT - a Monte Carlo investigation. Phys Med Biol 1984; 29(10):1217-1230.

Floyd Jr. CE, Jaszczak RJ, Harris CC, Coleman RE. Revised scatter fraction results for SPECT. [Letter to the editor]. Phys Med Biol 1987; 32(12):1663-1666.

Graham LS, LaFontaine R, Stein MA. Effects of asymmetric photopeak windows on flood field uniformity and spatial resolution of scintillation cameras. J Nucl Med 1986; 27:706-713.

Gullberg GT, Malko JA, Eisner RL. Boundary determination methods for attenuation correction in single photon emission computed tomography. In: Esser PD, ed. Emission computed tomography: Current trends. New York: Society of Nuclear Medicine, 1983.

Heller SL, Goodwin PN. SPECT Instrumentation: Performance, lesion detection and recent innovations. Seminars in Nuclear Medicine 1987, 17(3):184-199.

Hounsfield GN. Computerised transverse axial scanning (tomography). 1. Description of system. Br J Radiol; 46: 1016-1022.

Jaszczak RJ, Coleman RE, Whitehead FR. Physical factors affecting quantitative measurements using camera-based single photon emission computed tomography (SPECT). IEEE Trans Nucl Sci 1981; NS-28:69-80.

Jaszczak RJ, Floyd Jr. CE, Coleman RE. Scatter compensation techniques for SPECT. IEEE Trans Nucl Sci 1985; NS-32:786-793.

Jaszczak RJ, Greer KL, Coleman RE. SPECT. In: Rao DV, Chandra R, Graham MC, ed. Physics of nuclear medicine - recent advances. New York: American Institute of Physics, Inc., 1984: 457-482. (AAPM Medical Physics Monograph No.10).

Jaszczak RJ, Greer KL, Floyd Jr. CE, Harris CC, Coleman RE. Improved SPECT quantification using compensation for scattered photons. J Nucl Med 1984; 25:893-900.

Jaszczak RJ, Greer KL, Floyd Jr. CE, Harris CC, Coleman RE. Estimating SPECT count densities, scatter fractions and statistical noise. IEEE Trans Nucl Sci 1985; NS-32:762-768.

Johns HE, Cunningham JR. The physics of radiology. 4th ed. Springfield, Illinois: C.Thomas, 1983.

Kay DB, Keys JW. First order correction for absorption and resolution compensation in radionuclide fourier tomography. J Nucl Med 1975; 16:540-541.

King MA, Schwinger RB, Esser PD et al. Preliminary characterization of the properties of a new rotating SPECT imaging system. In: Esser PD, ed. Emission computed tomography: current trends. New York: Society of Nuclear Medicine, 1983.

LaFontaine R, Stein MA, Graham LS. Contrast enhancement of cold lesions using asymmetric photopeak windows. Radiol (abst) 1983; 149(P):232.

- Lewellen T, Murano R, Weimer K et al. The use of asymmetric windows. In: Raynaud C, ed. Proceedings of the third world congress of nuclear medicine and biology, volume 2. Pergamon Press, 1982:1236-1239.
- Manglos SH, Floyd Jr. CE, Jaszczak RJ, Greer KL, Harris CC, Coleman RE. Experimentally measured scatter fractions and energy spectra as a test of Monte Carlo simulations. *Phys Med Biol* 1987; 32(3):335-343.
- McAinsh TF (ed). *Physics in medicine and biology encyclopedia*. New York: Pergamon Press, 1986.
- Metz CE, Beck RN. Quantitative effects of stationary linear image processing on noise and resolution of structure in radionuclide images. *J Nucl Med* 1973; 15(3):164-170.
- Moore SC. Attenuation compensation. In: Ell PJ, Holman BL, eds. *Computed emission tomography*. Oxford University Press, 1982:339-360.

Pratt WK. Digital image processing. New York: John Wiley and Sons, 1978.

Radon J. On the determination of functions from their integrals along certain manifolds. (Berichte über die Verhandlungen der königlich Sachsischen Gesellschaft der Wissenschaften zu Leipzig). Mathematisch-Physische Klasse 1917; 69:262-277 [Ger].

Roentgen WC. The rays. Nature 1896; 53:274-276.

Shepp LA, Logan BF. The Fourier reconstruction of a head section. IEEE Trans Nucl Sci 1974; NS-21:21-43.

Sorenson JA. Methods for quantitative measurement of radioactivity in vivo by whole-body counting. In: Hine GJ, Sorenson JA, eds. Instrumentation in nuclear medicine, vol 2. New York: Academic Press, 1974:311-348.

Sorenson JA, Phelps ME. Physics in nuclear medicine. 2nd ed. Toronto: Grune and Stratton, 1987.